# Supplementary Information

## Contents

# 1 Background

## 1.1 Koopman Operator: Definition, Properties, and Spectrum

The Koopman operator provides an alternative, linear framework for analyzing nonlinear dynamical systems [1, 2]. Consider a state space $\mathcal{M} \subseteq \mathbb{R}^n$ and a flow $S^t : \mathcal{M} \to \mathcal{M}$ ($t \geq 0$) defined on this space. The Koopman operator $K^t$ acts on a function space $\mathcal{F}$ of observables $g : \mathcal{M} \to \mathbb{C}$.

### Koopman Operator and Linearization

The family of Koopman operators $\{K^t\}_{t\geq 0}$ is defined as follows:

**Definition 1** (Koopman Operator) For any observable function $g \in \mathcal{F}$ and time $t \geq 0$, the Koopman operator $K^t$ maps the observable to a new function, evaluated at a state $\mathbf{x} \in \mathcal{M}$, by

$$(K^t g)(\mathbf{x}) = g(S^t(\mathbf{x})). \tag{1}$$

This operation means that evaluating the "pushed-forward" observable $K^t g$ at the initial state $\mathbf{x}$ is equivalent to evaluating the original observable $g$ at the evolved state $S^t(\mathbf{x})$. The Koopman operator is well-defined for any flow satisfying the semigroup property: $S^{t_1} \circ S^{t_2} = S^{t_1+t_2}$.

The operator's key property is its linearity: $K^t(\alpha_1 g_1 + \alpha_2 g_2) = \alpha_1 K^t g_1 + \alpha_2 K^t g_2$. This linearity enables the transformation of the nonlinear state dynamics $\dot{\mathbf{x}} = \mathbf{f}(\mathbf{x})$ into an equivalent infinite-dimensional linear system in the observable space $\mathcal{F}$.

The infinitesimal generator $L : \mathcal{D}(L) \to \mathcal{F}$ is defined such that $\frac{\partial}{\partial t}(K^t g)|_{t=0} = Lg$. For a flow generated by $\dot{\mathbf{x}} = \mathbf{f}(\mathbf{x})$, the generator can be explicitly computed for sufficiently smooth observables $g$ as the Lie derivative along the vector field $\mathbf{f}$ [3]:

$$(Lg)(\mathbf{x}) = \mathbf{f}(\mathbf{x}) \cdot \nabla g(\mathbf{x}). \tag{2}$$

The Koopman framework expresses the system dynamics via $L$:

$$\dot{g} = Lg, \quad \forall g \in \mathcal{D}(L). \tag{3}$$

### Koopman Spectrum and Eigenfunctions

The Koopman operator's spectrum provides a powerful tool for modal decomposition.

**Definition 2** (Koopman Eigenvalue and Eigenfunction) A scalar $\lambda_i \in \mathbb{C}$ is a Koopman eigenvalue, and a non-zero function $\varphi_i \in \mathcal{F} \setminus \{0\}$ is its corresponding Koopman eigenfunction, if they satisfy:

$$K^t \varphi_i = e^{\lambda_i t} \varphi_i, \quad \forall t \geq 0. \tag{4}$$

This definition shows that the Koopman eigenfunction $\varphi_i(\mathbf{x})$ evolves linearly in time, independent of other modes. The eigenvalues of $K^t$ are exponentially related to

the eigenvalues of the generator $L$, $\lambda_i$, which satisfy the eigenvalue problem $L\varphi_i = \lambda_i\varphi_i$. The set of all eigenvalues $\sigma(L)$ is known as the "Koopman spectrum".

Koopman eigenfunctions exhibit a multiplicative closure property [4]:

**Proposition 1** (Algebraic Property of Eigenfunctions [4]) *If $\varphi_1, \varphi_2 \in \mathcal{F}$ are Koopman eigenfunctions with eigenvalues $\lambda_1, \lambda_2 \in \mathbb{C}$, then the product $\varphi_1^{c_1}\varphi_2^{c_2}$ $(c_1, c_2 \in \mathbb{N})$ is also a Koopman eigenfunction corresponding to the eigenvalue $c_1\lambda_1 + c_2\lambda_2$.*

The analysis typically focuses on the "discrete spectrum" (eigenvalues), which corresponds to functions that evolve purely exponentially, while the "continuous spectrum" (when present in non-hyperbolic systems) is associated with more complex, mixing dynamics. For bounded operators, the relationship between the spectra of $K^\tau$ and $L$ holds:

$$\sigma(K^\tau) = \{e^{\lambda\tau} : \lambda \in \sigma(L)\}. \tag{5}$$

***The computation of matrix logarithm and exponential***

In practice, the Koopman operator and its generator are approximated by finite-dimensional matrices $\mathbf{K}^t$ and $\mathbf{L}$, which are connected through matrix exponential and logarithm:

$$\mathbf{K}^{T_s} = \exp(\mathbf{L}T_s), \tag{6}$$

$$\mathbf{L} = \log(\mathbf{K}^{T_s})/T_s. \tag{7}$$

The log and exp functions in (6) and (7) are calculated according to the standard matrix exponential and logarithmic series expansions [5], i.e.,

$$\log(\mathbf{K}^{T_s}) \equiv \sum_{k=1}^{\infty} \frac{(-1)^{k+1}}{k}(\mathbf{K}^{T_s} - \mathbf{I})^k, \tag{8}$$

$$\exp(T_s\mathbf{L}) \equiv \sum_{k=0}^{\infty} \frac{1}{k!}(T_s\mathbf{L})^k. \tag{9}$$

Evaluating the matrix logarithm and exponential requires efficient numerical algorithms. Extensive studies in numerical linear algebra have developed robust methods tailored to different matrix structures [6–8]. In this work, we adopt the logarithm and exponential algorithms [8–10] implemented in Python through the functions `scipy.linalg.logm` and `scipy.linalg.expm`, which internally employ scaling–squaring techniques and Padé approximants to ensure stable computation even for ill-conditioned matrices.

## 1.2 Extended Dynamic Mode Decomposition with Logarithm (EDMD-log)

Extended Dynamic Mode Decomposition (EDMD) [11] provides a data-driven approximation of the Koopman operator, a linear but infinite-dimensional operator that governs the evolution of observables of nonlinear dynamical systems. Given a

dictionary of observables $\boldsymbol{\psi}(\mathbf{x}) = [\psi_1(\mathbf{x}), \ldots, \psi_N(\mathbf{x})]^T$, EDMD constructs a finite-dimensional approximation of the Koopman operator $\mathbf{K} \in \mathbb{R}^{N \times N}$ with snapshot pairs $(\mathbf{x}_k, \mathbf{x}_{k+1})$ obtained from the system $\dot{\mathbf{x}} = \mathbf{f}(\mathbf{x})$ by solving

$$\mathbf{K} = \mathbf{X}_{\text{lift}}^{\dagger} \mathbf{Y}_{\text{lift}}, \tag{10}$$

where

$$\mathbf{X}_{\text{lift}} = \frac{1}{M} \sum_{k=1}^{M} \boldsymbol{\psi}(\mathbf{x}_k) \boldsymbol{\psi}(\mathbf{x}_k)^T, \quad \mathbf{Y}_{\text{lift}} = \frac{1}{M} \sum_{k=1}^{M} \boldsymbol{\psi}(\mathbf{x}_k) \boldsymbol{\psi}(\mathbf{x}_{k+1})^T, \tag{11}$$

and $M$ is the number of samples.

To recover the continuous-time generator $\mathbf{L}$, we compute the matrix logarithm of $\mathbf{K}$,

$$\mathbf{L} = \frac{1}{\Delta t} \log(\mathbf{K}), \tag{12}$$

where $\Delta t$ is the sampling interval.

This generator captures the infinitesimal dynamics and can be directly related to the system's vector field. In practice, the logarithm is evaluated via the principal branch, and care must be taken to handle cases when $\mathbf{K}$ has eigenvalues outside the unit circle due to noise.

The EDMD-log framework thus provides a direct pathway from discrete snapshot data to continuous-time system identification without requiring numerical differentiation. In following sections, we detail the derivation of its theoretical growth rate and compare it with that of SINDy.

# 2 Error Analysis of Derivative-Based Approach

Consider the dynamical system $\dot{\mathbf{x}} = \mathbf{f}(\mathbf{x})$ and its sampled version at time $t_k = kT_s$, denoted by $\mathbf{x}_k = \mathbf{x}(t_k)$.

### Forward difference approximation

The forward difference approximation of the time derivative is given by

$$\dot{\mathbf{x}}(t_k) \approx \frac{\mathbf{x}_{k+1} - \mathbf{x}_k}{T_s}. \tag{13}$$

Substituting the exact solution $\mathbf{x}(t)$ into the expression and using the Taylor expansion at $t_k$ yields:

$$\mathbf{x}(t_k + T_s) = \mathbf{x}(t_k) + T_s \dot{\mathbf{x}}(t_k) + \frac{T_s^2}{2} \ddot{\mathbf{x}}(t_k) + \mathcal{O}(T_s^3). \tag{14}$$

and forward difference error becomes

$$\frac{\mathbf{x}_{k+1} - \mathbf{x}_k}{T_s} = \dot{\mathbf{x}}_k + \frac{T_s}{2} \ddot{\mathbf{x}}_k + \mathcal{O}(T_s^2). \tag{15}$$

Thus, the approximation error is

$$\text{Error}_{\text{forward}} = \frac{T_s}{2}\ddot{\mathbf{x}}_k + \mathcal{O}(T_s^2). \tag{16}$$

### Backward difference approximation

Similarly, the backward difference is given by

$$\dot{\mathbf{x}}(t_k) \approx \frac{\mathbf{x}_k - \mathbf{x}_{k-1}}{T_s}, \tag{17}$$

and the Taylor expansion at $t_k$ gives

$$\frac{\mathbf{x}_k - \mathbf{x}_{k-1}}{T_s} = \dot{\mathbf{x}}_k - \frac{T_s}{2}\ddot{\mathbf{x}}_k + \mathcal{O}(T_s^2), \tag{18}$$

which implies

$$\text{Error}_{\text{backward}} = -\frac{T_s}{2}\ddot{\mathbf{x}}_k + \mathcal{O}(T_s^2). \tag{19}$$

### Central difference approximation

The central difference is given by

$$\dot{\mathbf{x}}(t_k) \approx \frac{\mathbf{x}_{k+1} - \mathbf{x}_{k-1}}{2T_s}, \tag{20}$$

and Taylor expansion leads to

$$\frac{\mathbf{x}_{k+1} - \mathbf{x}_{k-1}}{2T_s} = \dot{\mathbf{x}}(t_k) + \frac{T_s^2}{6}\dddot{\mathbf{x}}(t_k) + \mathcal{O}(T_s^4). \tag{21}$$

Then we obtain the error

$$\text{Error}_{\text{central}} = \frac{T_s^2}{6}\dddot{\mathbf{x}}_k + \mathcal{O}(T_s^4). \tag{22}$$

## 3 Error Analysis of EDMD-log-based Approach

Given the vector field $\mathbf{f}$ and observable function $g$, the Koopman generator $L$ satisfies:

$$\mathbf{f}(\mathbf{x}) \cdot \nabla g(\mathbf{x}) = Lg(\mathbf{x}), \quad \forall g \in C^1. \tag{23}$$

Denote the invariant space of the Koopman operator as $\mathcal{F}$ with norm $\|\cdot\|$ and consider a finite-dimensional function space $\mathcal{G}_N = \text{span}\{g_1, \ldots, g_N\} \subseteq \mathcal{F}$. We define the projection operator $P_N : \mathcal{F} \to \mathcal{G}_N$ through:

$$P_N h = \arg\min_{g \in \mathcal{G}_N} \|h - g\|, \ \forall h \in \mathcal{F}. \tag{24}$$

Assuming that state coordinate functions $\{\mathrm{id}_k(\mathbf{x}) = x_k\}_{k=1}^n$ belong to $\mathcal{G}_N$, the estimated vector field (via EDMD) $\hat{\mathbf{f}}_N \in \mathcal{G}_N$ is reconstructed from identified generator $\widehat{\mathbf{L}}$ via:

$$\widehat{\mathbf{L}} \cdot \mathbf{id}(\mathbf{x}) = \hat{\mathbf{f}}_N(\mathbf{x}) \cdot \nabla \mathbf{id}(\mathbf{x}), \tag{25}$$

where $\mathbf{id}(\mathbf{x}) = [\mathrm{id}_1(\mathbf{x}) = x_1, \ldots, \mathrm{id}_n(\mathbf{x}) = x_n]^\top$, i.e.,

$$\hat{\mathbf{f}}_N(\mathbf{x}) := \widehat{\mathbf{L}} \cdot \mathbf{id}(\mathbf{x}) = \frac{1}{T_s} \log(\widehat{\mathbf{K}}) \mathbf{id}(\mathbf{x}), \tag{26}$$

with $\widehat{\mathbf{K}} : \mathcal{G}_N \to \mathcal{G}_N$ being the EDMD approximation of the Koopman operator over sampling period $T_s$.

### Step 1: Identification error decomposition

Denote the projected Koopman generator as $\mathbf{L}_N = P_N L P_N$. Let $\mathbf{L}_N \in \mathbb{C}^{N \times N}$ be diagonalizable:

$$\mathbf{L}_N = \mathbf{V} \mathbf{\Lambda} \mathbf{V}^{-1}, \quad \mathbf{\Lambda} = \mathrm{diag}(\lambda_1, \ldots, \lambda_N),$$

and define the semigroup $\mathbf{K}_N^t : \mathcal{G}_N \to \mathcal{G}_N$ generated by the projected Koopman generator as $\mathbf{K}_N^t := e^{t\mathbf{L}_N}, t \geq 0$. We have

$$\mathbf{K}_N^{T_s} := e^{T_s \mathbf{L}_N} = \mathbf{V} \mathrm{diag}(\mu_i) \mathbf{V}^{-1}, \tag{27}$$

where $\mu_i = e^{T_s \lambda_i}$. Then we define the related projected vector field $\mathbf{f}_N \in \mathcal{G}_N$ through:

$$\mathbf{f}_N(\mathbf{x}) := \mathbf{L}_N \cdot \mathbf{id}(\mathbf{x}). \tag{28}$$

Then we analyze the total error in estimating the vector field $\mathbf{f}(x)$ via:

$$\mathbf{f}(\mathbf{x}) - \hat{\mathbf{f}}_N(\mathbf{x}) = \underbrace{\mathbf{f}(\mathbf{x}) - \mathbf{f}_N(\mathbf{x})}_{\text{Projection Error}} + \underbrace{\mathbf{f}_N(\mathbf{x}) - \hat{\mathbf{f}}_N(\mathbf{x})}_{\text{EDMD Approximation Error}}. \tag{29}$$

### Step 2: Projection error

The projection error of vector field can be represented by the residual of Koopman generator, i.e.,

$$\mathbf{f}(\mathbf{x}) - \mathbf{f}_N(\mathbf{x}) = (L - \mathbf{L}_N)\, \mathbf{id}(\mathbf{x}). \tag{30}$$

It is clear that this error is not related to the sampling period.

### Step 3: EDMD approximation error

Let $\widehat{\mathbf{K}} = \mathbf{K}_N^{T_s} + \epsilon$ and define

$$\widehat{\mathbf{L}} = \frac{1}{T_s} \log(\widehat{\mathbf{K}}) = \frac{1}{T_s} \log(\mathbf{K}_N^{T_s} + \epsilon). \tag{31}$$

Let $\lambda_j$ be a simple eigenvalue of $\mathbf{L}_N$ with the smallest real part, i.e.,

$$\Re\lambda_j = \min_i \Re\lambda_i = \Re\lambda_{\min},$$

and assume that $\lambda_{\min} < 0$. We denote $\mathbf{v}_j$ and $\mathbf{u}_j^*$ the corresponding right and left eigenvectors normalized by $\mathbf{u}_j^*\mathbf{v}_j = 1$. Assume that the perturbation is sufficiently small and has a nonzero projection on the eigenspace, $|\mathbf{u}_j^*\epsilon\mathbf{v}_j| \geq c_\epsilon > 0$, and that $\kappa(\mathbf{V}) = \|\mathbf{V}\|\|\mathbf{V}^{-1}\|$ is bounded independently of $T_s$.

***Eigenvalue perturbation.***

For a simple eigenvalue $\mu_j$ of $\mathbf{K}_N^{T_s}$, the first-order perturbation expansion from standard spectral perturbation theory [12] gives

$$\Delta\mu_j = \widehat{\mu}_j - \mu_j = \mathbf{u}_j^*\epsilon\mathbf{v}_j + \mathcal{O}(\|\epsilon\|^2), \tag{32}$$

so that the generator eigenvalue perturbation satisfies, by Taylor expansion,

$$\Delta\lambda_j = \frac{1}{T_s}\left(\log(\mu_j + \Delta\mu_j) - \log\mu_j\right) = \frac{1}{T_s}\frac{\Delta\mu_j}{\mu_j} + \mathcal{O}\left(\frac{\|\epsilon\|^2}{T_s}\right), \tag{33}$$

which implies

$$|\Delta\lambda_j| \gtrsim \frac{1}{T_s}\frac{|\mathbf{u}_j^*\epsilon\mathbf{v}_j|}{|\mu_j|} - \mathcal{O}\left(\frac{\|\epsilon\|^2}{T_s}\right). \tag{34}$$

***Matrix perturbation.***

Using the Fréchet derivative of the matrix logarithm [8],

$$\widehat{\mathbf{L}} \approx \mathbf{L}_N + \frac{1}{T_s}\mathrm{D}\log(\mathbf{K}_N^{T_s})[\epsilon] + \mathcal{O}(\|\epsilon\|^2),$$

and in the eigenbasis of $\mathbf{K}_N^{T_s}$,

$$\left[\mathrm{D}\log(\mathbf{K}_N^{T_s})[\epsilon]\right]_{jj} = \frac{1}{\mu_j}\mathbf{u}_j^*\epsilon\mathbf{v}_j.$$

Let $\mathbf{id}(\mathbf{x}) = \sum_{k=1}^N c_k(\mathbf{x})\mathbf{v}_k$, and choose $\mathbf{x}_j$ such that $c_j(\mathbf{x}_j) \neq 0$. Projecting the local error $\mathbf{e}(\mathbf{x}_j) = (\widehat{\mathbf{L}} - \mathbf{L}_N)\mathbf{id}(\mathbf{x}_j)$ onto $\mathbf{u}_j^*$ gives

$$\mathbf{u}_j^*\mathbf{e}(\mathbf{x}_j) = \sum_{k=1}^N c_k(\mathbf{x}_j)\,\mathbf{u}_j^*(\widehat{\mathbf{L}} - \mathbf{L}_N)\mathbf{v}_k \tag{35}$$

$$\approx c_j(\mathbf{x}_j)\,\mathbf{u}_j^*(\widehat{\mathbf{L}} - \mathbf{L}_N)\mathbf{v}_j + \mathcal{O}\left(\frac{\|\epsilon\|^2}{T_s}\right) \approx c_j(\mathbf{x}_j)\Delta\lambda_j + \mathcal{O}\left(\frac{\|\epsilon\|^2}{T_s}\right). \tag{36}$$

By the Cauchy–Schwarz inequality,

$$\|\mathbf{e}(\mathbf{x}_j)\| \geq \frac{|u_j^* \mathbf{e}(\mathbf{x}_j)|}{\|\mathbf{u}_j\|} \geq C_1 |\Delta\lambda_j| - C_2 \frac{\|\epsilon\|^2}{T_s}, \tag{37}$$

where $C_1 = \frac{|c_j(\mathbf{x}_j)|}{\|\mathbf{u}_j\|}$. Since $\mu_j = e^{T_s \lambda_j}$, it follows from (34) that

$$|\Delta\lambda_j| \gtrsim \frac{e^{T_s |\Re\lambda_{\min}|}}{T_s} |\mathbf{u}_j^* \epsilon \mathbf{v}_j| - \mathcal{O}\left(\frac{\|\epsilon\|^2}{T_s}\right). \tag{38}$$

Substituting into (37) yields the final lower bound

$$\|\widehat{\mathbf{f}}_N(\mathbf{x}) - \mathbf{f}_N(\mathbf{x})\| \geq C_1' \frac{e^{T_s |\Re\lambda_{\min}|}}{T_s} - C_2' \frac{\|\epsilon\|^2}{T_s}, \tag{39}$$

where the constants $C_1'$ and $C_2'$ absorb $C_1$ and the higher-order terms.

This error typically increases rapidly as sampling time $T_s$ grows, due to the exponential factor in stable systems ($\Re\lambda_{\min} < 0$). This occurs because the discrete Koopman eigenvalues, $|\mu_j| = e^{T_s \Re\lambda_j}$, decay exponentially towards zero as $T_s$ grows. Recovering the generator $\mathbf{L}$ requires computing the logarithm of these nearly vanishing terms, a highly ill-conditioned operation. Consequently, the perturbation in the error is amplified by a factor proportional to $\frac{1}{|\mu_j|}$, which establishes the asymptotic lower bound that grows exponentially as $\frac{e^{T_s |\Re\lambda_{\min}|}}{T_s}$.

# 4 Data Preparation

The dataset used in this study consists of two categories: synthetic systems and realistic systems. The data preparation procedures for each category are described below.

## 4.1 Synthetic dataset

The synthetic datasets used in this study are generated by numerically solving the governing ordinary differential equations (ODEs) of each dynamical system. Simulations are performed using MATLAB's `ode45` solver to ensure accurate integration of the continuous-time dynamics. For each system listed in Supplementary Table 1, $N_{\text{traj}}$ initial states are randomly sampled within a predefined initial region $R$. Each initial condition is integrated forward in time to generate a continuous trajectory. The resulting trajectories are subsequently downsampled at various sampling periods $\Delta t$ to produce discrete-time observation sequences with varying temporal resolutions. Each trajectory contains $N_{\text{sim}}$ time steps. The system dimension $d$ denotes the number of state variables in the dynamical model.

**Table 1**: Simulation Setup for Synthetic Dynamical Systems

| Dynamic System | $d$ | $N_{\text{traj}}$ | $N_{\text{sim}}$ | $\Delta t$ | $R$ |
|---|---|---|---|---|---|
| Fixed Point | 2 | 1000 | 30 | $0.1, 0.2, \ldots, 1.0$ | $[-1, 1]^2$ |
| Limit cycle | 2 | 1000 | 30 | $0.1, 0.2, \ldots, 1.0$ | $[-1.5, 1.5]^2$ |
| Van der Pol | 2 | 1000 | 30 | $0.1, 0.2, \ldots, 0.5$ | $[-3, 3]^2$ |
| Duffing | 2 | 3000 | 10 | $0.1, 0.2, 0.3, 0.4$ | $[-4, 4]^2$ |

### 4.2 Benchmark and realistic dataset

Our experimental evaluation encompasses representative benchmark systems, including the glycolytic oscillator, chemical autocatalysis, SIR epidemic model, and language death model, exhibiting diverse dynamical behaviors characteristic of nonlinear processes in biological, chemical, epidemiological, and socio-linguistic domains. In addition to these synthetic benchmarks, the study incorporates realistic datasets composed of experimentally measured or physiologically recorded time series from physical and biological systems, each representing a distinct underlying dynamical process. Each system listed in Supplementary Table 2 contains $N_{\text{traj}}$ trajectories with $N_{\text{sim}}$ time steps at the sampling period $\Delta t$. The measured variables denote the observed quantities, which may include position, velocity, membrane potential, or other physical signals, and the system dimension $d$ denotes the number of state variables in the dynamical model. All data are preprocessed to ensure consistency in scale and temporal resolution before being used for training. The source and pre-processing methods for each dataset are introduced in corresponding sections.

## 5 Configurations of HANDI

### 5.1 Neural Network Architecture

The neural network used in this code is a simple multilayer perceptron (MLP) named DictNN. It serves as the neural basis function $\mathbf{G}(\mathbf{x})$. The network consists of *depth* hidden layers. The layer dimensions are $(in\_dim, width)$, followed by $depth - 1$ layers of $(width, width)$, and finally an output layer of $(width, out\_dim)$. All layers use `Tanh` as the activation function. Additionally, `Dropout` layers can be optionally applied after hidden layers.

### 5.2 Experimental Parameters

This section details the hyperparameter configurations used in the experiments, including settings for both the Phase I and Phase II. All experiments were conducted

**Table 2**: Data Specifications for benchmark and Realistic Dynamical Systems

| Dynamic System | Measured Variable | $d$ | $N_{\text{traj}}$ | $N_{\text{sim}}$ | $\Delta t$ |
|---|---|---|---|---|---|
| Chemical Autocatalysis | $x(t)$ | 1 | 2 | 9 | 2.25 |
| Language Death | $x(t)$ | 1 | 2 | 6 | 2.0 |
| SIR Epidemic | $x_1(t)$, $x_2(t)$ | 2 | 2 | 34 | 0.3 |
| Glycolytic Oscillator | $x_1(t)$, $x_2(t)$ | 2 | 2 | 34 | 0.3 |
| Simple Pendulum | $x(t)$, $\dot{x}(t)$ | 2 | 1 | 37 | 0.3 |
| Inverted Flag | $x_1(t)$, $\dot{x}_1(t)$, $x_2(t)$, $\dot{x}_2(t)$ | 4 | 4 | 76 | 0.2 |
| Wheel Shimmy | $\theta$, $\omega$ | 2 | 2 | 28 | 0.11 |
| Neural Integration | $V(t)$, $W(t)$, $I$ | 3 | 2 | 20 | 0.03 |

using the same general framework, with parameters tuned per system based on empirical performance or auto-tuning. The key experimental parameters are summarized in Supplementary Table 3. The famework is defined by hidden layers with width of $W$, depth of $D$, and dropout rate of *dropout*. The batch size is set to 1024, and gradient clipping is applied at a threshold of 1.0. Training is initialized with a random seed of 3407. A validation split of 20% is used for performance monitoring. All models were trained using the AdamW optimizer with a weight decay of 1.0e−5. The initial learning rate in Phase I ($lr_A$) is set to 2e−3, and the learning rate schedule was implemented via a LambdaLR schedule. During Phase I, $lr_A$ decays cosine-style over the final fraction (default 30%) of epochs. In Phase II, $lr_B$ starts at 3e−3 and decreases to 3e−4 using a cosine annealing schedule. For each dynamic system, specific hyperparameters are tuned to optimize performance, as summerized in Supplementary Table 3. These include:

- $\Delta t$: the time step of the simulation data;
- *polyorder*: the degree of the polynomial basis used in the fixed dictionary
- $g_{dim}$: the the dimensionality of the learned neural dictionary;
- $W$: the width of the framework;
- $D$: the depth of the framework;
- *dropout*: the dropout rate applied to prevent overfitting;
- $epochs_A$: the number of training epochs in Phase I;
- $epochs_B$: the number of training epochs in Phase II;
- $\lambda_g$: the regularization strength for the residual dictionary;
- $\lambda_{full}$: the regularization strength for the full augmented Koopman operator;
- $\beta_{align}$: the weighting coefficient for multi-step rollout consistency loss in Phase II.

**Table 3**: Detailed setup of HANDI for dynamical systems

| Dynamic System | $dt$ | $polyorder$ | $g_{dim}$ | $W$ | $D$ | $dropout$ | $epochs_A$ | $epochs_B$ | $\lambda_g$ | $\lambda_{full}$ | $\beta_{align}$ |
|---|---|---|---|---|---|---|---|---|---|---|---|
| Fixed Point | 1.0 | 7 | 30 | 96 | 7 | 0.2 | 120 | 300 | 1.808e-6 | 1.108e-7 | 2.344e-4 |
| Limit cycle | 1.0 | 5 | 45 | 128 | 5 | 0.4 | 100 | 240 | 3.007e-7 | 3.798e-6 | 1.486e-3 |
| Van der Pol | 0.5 | 5 | 45 | 96 | 4 | 0.1 | 120 | 220 | 1.629e-5 | 4.405e-7 | 4.401e-2 |
| Duffing | 0.4 | 3 | 56 | 192 | 5 | 0.4 | 110 | 180 | 9.357e-7 | 2.124e-6 | 3.932e-3 |
| Chemical Autocatalysis | 2.25 | 2 | 60 | 192 | 3 | 0.05 | 90 | 140 | 4.985e-7 | 1.351e-6 | 2.567e-2 |
| Language Death | 2.0 | 1 | 63 | 64 | 3 | 0.35 | 110 | 220 | 3.178e-7 | 1.221e-6 | 3.296e-3 |
| SIR Epidemic | 0.3 | 2 | 60 | 96 | 3 | 0.0 | 80 | 220 | 1.358e-5 | 2.404e-5 | 1.298e-2 |
| Glycolytic Oscillator | 0.3 | 3 | 56 | 128 | 3 | 0.05 | 120 | 200 | 9.812e-6 | 5.315e-7 | 1.260e-2 |
| Simple Pendulum | 0.3 | 2 | 4 | 224 | 3 | 0.0 | 180 | 300 | 2.911e-6 | 8.365e-6 | 7.040e-2 |
| Inverted flag | 0.2 | 3 | 5 | 224 | 3 | 0.35 | 230 | 120 | 1.529e-5 | 7.135e-6 | 8.542e-2 |
| Wheel Shimmy | 0.11 | 4 | 51 | 64 | 2 | 0.1 | 90 | 300 | 1.721e-6 | 4.992e-6 | 1.092e-3 |
| Neural Integration | 0.03 | 3 | 56 | 96 | 7 | 0.35 | 180 | 280 | 1.429e-07 | 1.290e-07 | 5.782e-3 |

# 6 Supplementary Experimental Details

## 6.1 Evaluation Metrics

Consider dynamical system $\dot{\mathbf{x}} = \mathbf{f}(\mathbf{x})$ and assume that the vector field $\mathbf{f}(\mathbf{x})$ is

$$\mathbf{f}(\mathbf{x}) = \sum_{k=1}^{m} \boldsymbol{C}_k \boldsymbol{\phi}(\mathbf{x}_k), \tag{40}$$

where $\boldsymbol{\phi}(\mathbf{x}_k)$ are candidate functions, $\boldsymbol{C}_k \in \mathbb{R}^d$, and the vectors $\mathbf{C}_{\text{true}} = [\boldsymbol{C}_1, \ldots, \boldsymbol{C}_d]^\top \in \mathbb{R}^n$ are unknown coefficients (to be identified). In our experiments, we employ the following metrics.

$$\text{NRMSE} = \frac{\sqrt{\frac{1}{md}\sum_{i=1}^{m}\sum_{j=1}^{d}\left(\mathbf{C}_{\text{hat}}(i,j) - \mathbf{C}_{\text{true}}(i,j)\right)^2}}{\frac{1}{|\Omega|}\sum_{(i,j)\in\Omega}\left|\mathbf{C}_{\text{true}}(i,j)\right|}, \tag{41}$$

where $\Omega = \{(i,j) : |\mathbf{C}_{\text{true}}(i,j)| > 0\}$, and $|\Omega|$ refers to the cardinality of $\Omega$.

$$\text{MSE} = \frac{1}{d\, N_{\text{traj}} N_{\text{sim}}} \sum_{k=1}^{N_{\text{traj}}} \sum_{j=0}^{N_{\text{sim}}} \|\mathbf{x}_k(t_j) - \hat{\mathbf{x}}_k(t_j)\|^2, \tag{42}$$

where $N_{\text{traj}}$ is the number of trajectories and $N_{\text{sim}}$ the number of predicted time steps.

The Area Under the Success Curve (AUSC) is computed by the normalized area under the success-rate curve over a fixed interval $[0, \delta_{\max}]$:

$$\text{AUSC} = \frac{1}{\delta_{\max}} \int_0^{\delta_{\max}} \text{SR}(\delta) \mathrm{d}\delta, \tag{43}$$

where $\delta_{\max} = 1.0$ for all methods and systems, success rate at threshold $\delta > 0$ is

$$\text{SR}(\delta) = \frac{1}{N} \sum_{k=1}^{N_{\text{traj}}} \mathbb{I}\left(\text{MSE}^{(k)} \leq \delta\right), \tag{44}$$

with $\mathbb{I}(\cdot)$ denotes the indicator function and $\text{MSE}^{(k)} = \frac{1}{d\, N_{\text{sim}}} \sum_{j=0}^{N_{\text{sim}}} \|\mathbf{x}_k(t_j) - \hat{\mathbf{x}}_k(t_j)\|^2$.

The Attractor Consistency Rate (ACR) is introduced to assess the physical fidelity of the recovered geometric attractors. It is defined as the probability that trajectories initialized from uniformly sampled states preserve the correct asymptotic attractor structure under the identified model. Specifically, we uniformly sample 100 initial conditions over the prescribed state space and evaluate whether the long-term behavior of each predicted trajectory satisfies system-dependent geometric criteria. The specific criteria in Supplementary Table 4 are designed to capture the topological invariants essential to each system's category. For instance, C2 for Fixed Points evaluates Lyapunov stability by measuring monotonic contraction; C2 for Limit Cycles

ensures orbital frequency consistency; and C3 for the Van der Pol system quantifies the singular perturbation profile inherent to relaxation oscillators.

## 6.2 Comparison Methods and Hyperparameter Configurations

To ensure a fair and reproducible comparison, we have carefully configured the hyperparameters for all benchmark methods. Given the large number of test cases (12 systems across various sampling intervals and noise levels), we report the representative configurations for the most challenging scenarios (e.g., largest $T_s$ or highest noise level) in Supplementary Tables 5-6. The exhaustive list of parameters for every specific case is provided in the accompanying source code as .json and .log files at https://github.com/kaixinzeng/HANDI. The parameter selection logic is provided as follows:

- SINDy: We performed a post-hoc manual grid search. For each case, the sparsity threshold *threshold* was optimized to achieve the minimum normalized root mean square error (NRMSE), representing the algorithm's best-case performance. The candidate functions is identical to those used in HANDI.
- SR3, WSINDy, and PSE: These methods are designed with built-in automated optimization routines. For SR3 and WSINDy, parameters—including the number of integration kernels $K$ in WSINDy, the sparsity threshold (*threshold*), and the relaxation coefficient ($\nu$) shared by both methods—were automatically tuned on a validation set, minimizing multi-step rollout prediction error. The maximum iteration count $max_iter$ was fixed during tuning. The candidate functions is identical to those used in HANDI.
- PSE: This method employs a neural-guided program synthesis framework to automatically discover symbolic expressions from data. Its key hyperparameters, including the operator library (e.g., ['Add', 'Mul', 'Sub', 'Identity']), input dimensionality ($n\_inputs$), time limit $time\_limit$ and expression selection strategy, are configured based on domain knowledge. The top-k (topk = 10) candidate expressions are selected by Pareto optimality over accuracy and complexity, and the best is chosen by reward.
- EDMD and gEDMD: These methods do not require no hyperparameter tuning. We ensured that their dictionary of basis (type and number is strictly identical to those used in HANDI).

## 6.3 Identification Performance of Dynamical systems

- Supplementary Table 7 summarizes the NRMSE of the identified governing equations for both the synthetic systems (at the maximum sampling interval) and the benchmark system (under maximum noise perturbation with 5 additive Gaussian noise), providing a normalized measure of model fidelity across different dynamical regimes.
- Supplementary Table 8 reports the mean and variance of the mean squared error (MSE) for the synthetic systems datasets evaluated at the largest sampling interval that still permits recovery of the true trajectory, $V_{trajs}$ denotes the number of

**Table 4**: ACR criteria for different dynamical systems.

| System | ACR criteria |
|---|---|
| **Fixed point** | **C1 (Equilibrium magnitude consistency):** $\left\lvert \max_{t\geq t_k} \lVert\hat{\mathbf{x}}(t)\rVert - \max_{t\geq t_k} \lVert\mathbf{x}(t)\rVert \right\rvert / \max_{t\geq t_k} \lVert\mathbf{x}(t)\rVert < \delta$ |
| | **C2 (Stability characterization):** $\frac{1}{N_k}\sum_j \mathbb{I}(\lVert\hat{\mathbf{x}}(t_{j+1})\rVert \leq \lVert\hat{\mathbf{x}}(t_j)\rVert) \geq \eta, \quad N_k = \lvert\{t_j \lvert t_j \geq t_k\}\rvert$ |
| | **C3 (Spiral rotation consistency):** $\lvert\hat{\omega} - \omega\rvert/\omega < \delta_\omega, \quad \hat{\omega} = \langle \Delta\theta(t)/\Delta t \rangle_{t\geq t_k}$ |
| **Limit cycle** | **C1 (Cycle amplitude consistency):** $\left\lvert \langle\lVert\hat{\mathbf{x}}(t)\rVert\rangle_{t\geq t_k} - \langle\lVert\mathbf{x}(t)\rVert\rangle_{t\geq t_k} \right\rvert / \langle\lVert\mathbf{x}(t)\rVert\rangle_{t\geq t_k} < \varepsilon_{\text{cyc}}$ |
| | **C2 (Temporal frequency consistency):** $\lvert\hat{T} - T\rvert/T \leq \delta_T$ |
| **Van der Pol** | **C1 (Period consistency):** $\lvert T - \hat{T}\rvert/T \leq \delta_T$ |
| | **C2 (Amplitude and boundedness):** $\left\lvert \langle\lVert\hat{\mathbf{x}}(t)\rVert\rangle_{t\geq t_k} - \langle\lVert\mathbf{x}(t)\rVert\rangle_{t\geq t_k} \right\rvert / \langle\lVert\mathbf{x}(t)\rVert\rangle_{t\geq t_k} < \varepsilon_{\text{cyc}}$ <br> $\varepsilon_{\min}\langle\lVert\mathbf{x}(t)\rVert\rangle_{t\geq t_k} \leq \lVert\hat{\mathbf{x}}(t)\rVert \leq \varepsilon_{\max}\langle\lVert\mathbf{x}(t)\rVert\rangle_{t\geq t_k},$ |
| | **C3 (Singular perturbation profile):** $Q_{\hat{v}}/Q_v \geq \gamma, \quad Q_v = \text{quantile}_{0.9}(\lVert\dot{\mathbf{x}}\rVert)/\text{quantile}_{0.1}(\lVert\dot{\mathbf{x}}\rVert)$ |
| **Duffing** | **C1 (Ergodic basin identification):** $\text{sign}\Big(\langle\hat{x}_1(t)\rangle_{t\geq t_k}\Big) = \text{sign}\Big(\langle x_1(t)\rangle_{t\geq t_k}\Big)$ |
| | **C2 (Terminal state proximity):** $\lVert\hat{\mathbf{x}}(t_{\text{end}}) - \mathbf{x}(t_{\text{end}})\rVert_2^2 < \varepsilon.$ |

**Table 5**: Detailed setup of SINDy and the variants for dynamical systems

| Dynamical System | $dt$ | SINDy | | SR3 | | | WSINDy | | | |
|---|---|---|---|---|---|---|---|---|---|---|
| | | *polyorder* | *threshold* | *polyorder* | *threshold* | $\nu$ | *polyorder* | $K$ | *threshold* | $\nu$ |
| Fixed Point | 1.0 | 7 | 0.1 | 7 | 1.240e-4 | 2.463e-6 | 7 | 100 | 7.100e-2 | 7.686e-3 |
| Limit cycle | 1.0 | 5 | 0.01 | 5 | 2.401e-2 | 5.338e-3 | 5 | 700 | 4.624e-2 | 9.449e-1 |
| Van der Pol | 0.5 | 5 | 0.01 | 5 | 7.868e-2 | 7.842e-3 | 5 | 300 | 4.202e-5 | 2.238e-5 |
| Duffing | 0.4 | 3 | 0.1 | 3 | 1.120e−2 | 4.041e−5 | 3 | 1000 | 1.032e−5 | 1.105e−6 |
| Chemical Autocatalysis | 2.25 | 2 | 0.01 | 2 | 1.142e-4 | 5.842e-6 | 2 | 100 | 6.617e-2 | 1.757e-6 |
| Language Death | 2.0 | 1 | 0.01 | 1 | 1.319e-3 | 1.259e-1 | 1 | 100 | 5.653e-5 | 3.438e-6 |
| SIR Epidemic | 0.3 | 2 | 0.01 | 2 | 6.169e-4 | 5.600e-1 | 2 | 400 | 0.01 | 2.311e-2 |
| Glycolytic Oscillator | 0.3 | 3 | 0.01 | 3 | 7.216e-2 | 5.934e-2 | 3 | 800 | 1.998e-4 | 2.099e-5 |
| Simple Pendulum | 0.3 | 2 | 0.01 | 2 | 4.382e−5 | 0.164 | 2 | 800 | 2.917e−4 | 1.288e−4 |
| Inverted flag | 0.2 | 3 | 0.001 | 3 | 1.789e−2 | 8.345e−5 | 3 | 100 | 5.375e−4 | 5.422e−4 |
| Wheel Shimmy | 0.11 | 4 | 0.05 | 4 | 0.1 | 5.094e-2 | 4 | 100 | 0.1 | 9.761e-1 |
| Neural Integration | 0.03 | 3 | 0.01 | 3 | 0.01 | 3.306e-4 | 3 | 650 | 1.189e-3 | 0.253 |

**Table 6**: Detailed setup of PSE, gEDMD and EDMD for dynamical systems

| Dynamical System | *dt* | PSE | | | gEDMD | | EDMD | |
|---|---|---|---|---|---|---|---|---|
| | | operators | *n_inputs* | *time_limit* (s) | *poly_basis* | *poly* | *poly_basis* | *poly* |
| Fixed point | 1.0 | ['Add', 'Mul', 'Sub', 'Identity'] | 5 | 3600 | 7 | 10 | 7 | 10 |
| Limit cycle | 1.0 | ['Add', 'Mul', 'Sub', 'Identity'] | 5 | 3600 | 5 | 10 | 5 | 10 |
| Van der Pol | 0.5 | ['Add', 'Mul', 'Sub', 'Identity'] | 5 | 3600 | 5 | 10 | 5 | 10 |
| Duffing | 0.4 | ['Add', 'Mul', 'Sub', 'Identity'] | 5 | 7200 | 3 | 10 | 3 | 10 |
| Chemical Autocatalysis | 2.25 | ['Add', 'Mul', 'Sub', 'Identity'] | 3 | 3600 | 2 | 10 | 2 | 10 |
| Language Death | 2.0 | ['Add', 'Mul', 'Sub', 'Identity'] | 2 | 3600 | 1 | 10 | 1 | 10 |
| SIR Epidemic | 0.3 | ['Add', 'Mul', 'Sub', 'Identity'] | 3 | 3600 | 2 | 10 | 2 | 10 |
| Glycolytic Oscillator | 0.3 | ['Add', 'Mul', 'Sub', 'Identity'] | 4 | 3600 | 3 | 10 | 3 | 10 |
| Simple Pendulum | 0.3 | ['Add', 'Mul', 'Sub', 'Identity'] | 3 | 7200 | 3 | 2 | 3 | 2 |
| Inverted flag | 0.2 | ['Add', 'Mul', 'Sub', 'Identity'] | 3 | 7200 | 4 | 3 | 4 | 3 |
| Wheel Shimmy | 0.11 | ['Add', 'Mul', 'Sub', 'Identity'] | 5 | 3600 | 4 | 10 | 4 | 10 |
| Neural Integration | 0.03 | ['Add', 'Mul', 'Sub', 'Identity'] | 5 | 10800 | 3 | 10 | 3 | 10 |

non-divergent (valid) trajectories out of $N_{trajs} = 100$ randomly sampled initial conditions, and the MSE is computed exclusively over these valid trajectories.

- Supplementary Table 9 presents the per-trajectory mean squared error (MSE) between the identified dynamics and ground-truth trajectories: for the benchmark systems, results are reported under the highest noise level considered (5 additive Gaussian noise) at their respective maximum admissible sampling intervals; for the realistic systems, results correspond to the largest sampling interval at which the true trajectory remains identifiable. Entries marked as $inf$ indicate trajectories that diverged during simulation.

**Table 7**: NRMSE Summary

| Systems | $dt$ | HANDI | SINDy | SR3 | PSE | WSINDy | gEDMD | EDMD |
|---|---|---|---|---|---|---|---|---|
| Fixed Point | 1.0 | 7.427e−1 | 2.744e+0 | 2.761e+0 | 2.515e+0 | 3.364e−1 | 1.180e+1 | 2.081e+0 |
| Limit cycle | 1.0 | 1.683e−1 | 6.210e−1 | 6.210e−1 | 1.633e+0 | 3.692e+0 | 1.181e+1 | 3.984e+0 |
| Van der Pol | 0.5 | 2.435e−2 | 1.084e−1 | 1.221e−1 | 2.739e−1 | 3.907e−2 | 1.660e−1 | 2.941e−1 |
| Duffing | 0.4 | 3.175e−3 | 1.659e−1 | 1.716e−1 | 6.285e−2 | 1.923e−3 | 2.053e−1 | 2.964e−1 |
| Chemical Autocatalysis | 2.25 | 1.209e−02 | 5.075e−01 | 6.283e−01 | 1.174e+00 | 1.267e+00 | 5.106e+03 | 8.240e+02 |
| Language Death | 2.0 | 3.714e−02 | 8.250e−01 | 8.139e−01 | 1.421e+01 | 1.012e+00 | 5.414e+03 | 9.289e+06 |
| SIR Epidemic | 0.3 | 7.777e−01 | 6.669e+00 | 1.503e+00 | 3.120e+00 | 1.598e+01 | 1.534e+05 | 5.376e−01 |
| Glycolytic Oscillator | 0.3 | 5.765e−01 | 1.274e+00 | 5.116e−01 | 1.009e+00 | 1.089e+01 | 4.288e+00 | 5.037e+03 |

### 6.3.1 Mass-Spring-Damper System

We consider a canonical mass–spring–damper oscillator (Supplementary Fig. 1), a fundamental prototype of vibration systems across diverse scales and disciplines, ranging from biomechanics [13] and fluid dynamics [14] to high-precision engineering such as microelectromechanical systems (MEMS) [15], nanopositioning [16], computational medicine [17], and energy harvesting [18]. Precise estimation is essential for functional realization, whether in designing vibration control laws for bridge stability [19] or enabling compliant robotic assistance via impedance control in surgical settings [20]. In high-precision domains, even minor parameter deviations severely degrade performance. However, the characteristic oscillation frequencies of many of these systems range from hundreds of hertz to several megahertz [15, 20]. Sustained high-fidelity

**Table 8**: MSE Summary of Canonical Systems

| Systems | $dt$ | Statistic | HANDI | SINDy | SR3 | PSE | WSINDy | gEDMD | EDMD |
|---|---|---|---|---|---|---|---|---|---|
| Fixed Point | 1.0 | MSE(mean $\pm$ std) | $0.0023 \pm 0.0029$ | $0.0920 \pm 0.0081$ | $0.0921 \pm 0.0082$ | $0.0532 \pm 0.0101$ | $0.4270 \pm 0.2548$ | $0.1152 \pm 0.0106$ | $0.0003 \pm 0.0007$ |
| | | $V_{\text{trajs}}/N_{\text{trajs}}$ | 100/100 | 100/100 | 100/100 | 100/100 | 100/100 | 44/100 | 76/100 |
| Limit cycle | 1.0 | MSE(mean $\pm$ std) | $0.0029 \pm 0.0058$ | $0.9870 \pm 0.0077$ | $0.9870 \pm 0.0077$ | $0.9169 \pm 0.1610$ | $1.3720 \pm 0.5642$ | $0.4831 \pm 0.0039$ | $inf$ |
| | | $V_{\text{trajs}}/N_{\text{trajs}}$ | 100/100 | 100/100 | 100/100 | 100/100 | 100/100 | 100/100 | 0/100 |
| Van der Pol | 0.5 | MSE(mean $\pm$ std) | $0.0832 \pm 0.2397$ | $0.6671 \pm 0.2910$ | $0.4779 \pm 0.4008$ | $1.3697 \pm 1.2120$ | $0.0859 \pm 0.1888$ | $0.5225 \pm 0.9765$ | $2.0299 \pm 3.8271$ |
| | | $V_{\text{trajs}}/N_{\text{trajs}}$ | 100/100 | 100/100 | 100/100 | 100/100 | 100/100 | 100/100 | 100/100 |
| Duffing | 0.4 | MSE(mean $\pm$ std) | $0.4248 \pm 0.8610$ | $3.0296 \pm 3.0871$ | $1.9713 \pm 2.4259$ | $6.9696 \pm 6.3141$ | $0.2522 \pm 0.5133$ | $2.2843 \pm 2.1121$ | 2.58e5 $\pm$ 2.85e5 |
| | | $V_{\text{trajs}}/N_{\text{trajs}}$ | 100/100 | 100/100 | 96/100 | 100/100 | 100/100 | 90/100 | 100/100 |

**Table 9**: MSE Summary of Benchmark/Real Systems

| Systems | $dt$ | Traj | HANDI | SINDy | SR3 | PSE | WSINDy | gEDMD | EDMD |
|---|---|---|---|---|---|---|---|---|---|
| Chemical Autocatalysis | 2.25 | $Traj_1$ | 3.523e−02 | 3.576e−01 | 6.690e−01 | 1.479e+01 | 1.553e+01 | 1.480e+01 | inf |
| | | $Traj_2$ | 3.801e−02 | 4.208e−02 | 3.566e−02 | 3.662e+00 | 1.109e+01 | inf | inf |
| Language Death | 2.0 | $Traj_1$ | 4.700e−04 | 7.065e−04 | 6.845e−04 | 1.233e−01 | 5.053e−02 | inf | inf |
| | | $Traj_2$ | 6.889e−04 | 1.252e−03 | 4.989e−05 | 3.833e−04 | 6.695e−04 | inf | inf |
| SIR Epidemic | 0.3 | $Traj_1$ | 2.262e−01 | 1.108e−02 | inf | 3.019e+00 | 5.702e+00 | 2.580e+01 | inf |
| | | $Traj_2$ | 1.748e−01 | inf | 2.456e−01 | 7.581e+01 | 7.703e+01 | 2.333e+02 | inf |
| Glycolytic Oscillator | 0.3 | $Traj_1$ | 2.969e−05 | 7.805e−04 | 1.350e−03 | 8.765e−04 | 8.765e−04 | inf | 2.451e−02 |
| | | $Traj_2$ | 1.468e−04 | 5.350e−03 | 2.573e−03 | 5.135e−02 | 5.135e−02 | inf | 3.584e−02 |
| Pendulum | 0.3 | $Traj_1$ | 1.782e−2 | 8.823e−1 | 1.393e+0 | inf | 1.107e+0 | inf | 5.799e−1 |
| Inverted Flag | 0.2 | $Traj_1$ | 2.673e−3 | inf | 4.554e−1 | 4.811e+0 | inf | inf | inf |
| | | $Traj_2$ | 2.434e−3 | inf | 4.278e−1 | inf | inf | inf | inf |
| | | $Traj_3$ | 9.854e−4 | inf | 4.283e−1 | 4.371e+0 | inf | inf | inf |
| | | $Traj_4$ | 1.796e−2 | 1.264e+0 | 4.289e−1 | 4.684e+0 | inf | inf | inf |
| Wheel Shimmy | 0.11 | $Traj_1$ | 2.615e−2 | 1.406e+0 | 2.428e+0 | 3.151e+0 | inf | inf | inf |
| | | $Traj_2$ | 3.446e−2 | 1.763e+1 | 2.177e+0 | 2.680e+0 | 1.794e+0 | inf | inf |
| Neural Integration | 0.03 | $Traj_1$ | 4.322e−2 | inf | 3.037e−2 | inf | 6.384e+0 | inf | 4.278e+0 |
| | | $Traj_2$ | 4.382e−2 | 1.671e−1 | inf | 2.622e−1 | 2.359e−1 | inf | inf |

measurement at these extreme rates is physically infeasible, as the required sampling rates rapidly deplete sensor bandwidth, storage capacity, and power resources. Consequently, high-frequency vibration dynamics represent a crucial scenario where sparse temporal sampling is not merely an experimental simplification, but a necessary practical constraint.

The system obeys Newton's second law:

$$\dot{\mathbf{x}} = \mathbf{A}\mathbf{x}, \qquad \mathbf{A} = \begin{bmatrix} 0 & 1 \\ -\frac{k}{m} & -\frac{c}{m} \end{bmatrix}, \tag{45}$$

where $\mathbf{x} = [x_1, x_2]$ denote the displacement and velocity, and $m$, $k$, $c$ are the mass, stiffness, and damping coefficients, respectively. We investigate three distinct physical regimes by modulating these parameters:

- Underdamped ($c^2 < 4mk$): $m = 1.0$,kg, $k = 17.0$,N/m, and $c = 2.0$,N·s/m.
- Critically damped ($c^2 = 4mk$): $m = 1.0\,\text{kg}$, $k = 16.0\,\text{N/m}$, and $c = 8.0\,\text{N·s/m}$.
- Overdamped ($c^2 > 4mk$): $m = 1.0\,\text{kg}$, $k = 25.0\,\text{N/m}$, and $c = 20.0\,\text{N·s/m}$.

From these parameters, we can obtain the natural frequency $\omega_n$ rad/s, the damped natural frequency $\omega_d$ rad/s, and the damping ratio $\zeta$ in each case.

### System identification under different sampling periods

We generate $N_{\text{traj}} = 1000$ trajectories with random initial conditions in $[-2, 2]^2$, each consisting of 30 samples, and repeat the identification procedure for different sampling periods:

$$T_s \in \{0.1,\ 0.2,\ 0.3,\ 0.4,\ 0.5,\ 0.6,\ 0.7\}\ \text{s}.$$

For each $T_s$, we identify the continuous-time vector field by SINDy (as a representative derivative-based identification method) and EDMD (as a representative flow-consistent identification method for linear systems). A *linear* polynomial library (degree = 1) is used to avoid overfitting and ensure a fair comparison with the flow-consistent model. Here we use the threshold $\texttt{threshold} = 10^{-1}$ in SINDy algorithm for subsequent analysis.

Supplementary Fig. 1a and Fig. 1b compare derivative-based and flow-consistent approaches for continuous-time system identification. Across three parameter regimes, the flow-consistent method (EDMD) maintains near-zero NRMSE over all sampling intervals (Supplementary Fig. 1c) and preserves the geometric organization of the phase portrait even under severe temporal sparsity ($T_s = 0.7$ s, Supplementary Fig. 1d). In contrast, the NRMSE of the derivative-based method (SINDy) increases rapidly as the sampling period grows. From a geometric perspective, the reconstructed vector field becomes distorted, and simulated trajectories progressively deviate from the true oscillatory manifold, losing periodicity and exhibiting overdamped behavior (Supplementary Fig. 1e). These results highlight the superior robustness of flow-consistent methods to sparse temporal sampling.

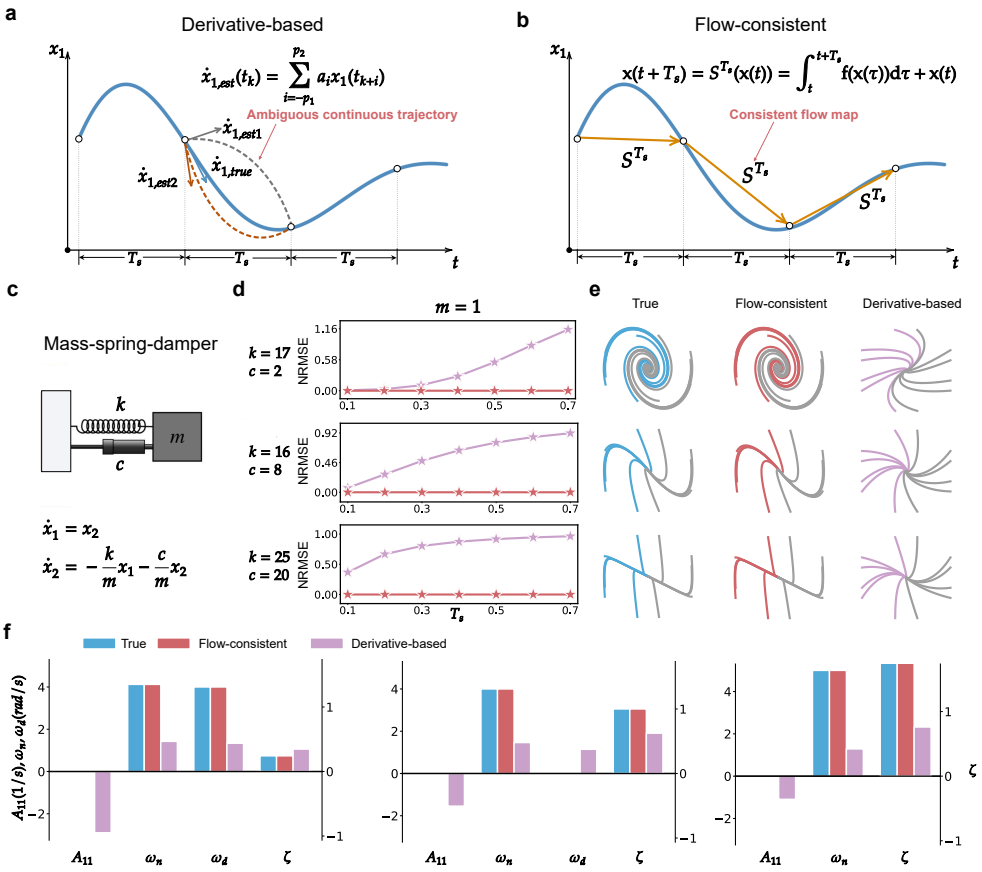


**Fig. 1**: Visualization of the saddle-focus dynamics of the mass–spring–damper system, showing trajectories spiraling toward the equilibrium before diverging along the unstable manifold.

Supplementary Fig. 1f further compares, for models identified from data sampled at $T_s = 0.7\,\mathrm{s}$, four representative physical quantities:

$$[A_{11},\ \omega_n,\ \omega_d,\ \zeta],$$

where $A_{11}$ characterizes the dependence of velocity on displacement, and $\omega_n$, $\omega_d$, and $\zeta$ denote the natural frequency, damped natural frequency, and damping ratio, respectively. The bars represent the ground truth (blue), flow-consistent (red), and derivative-based (purple). Physically, the derivative-based model causes physically inconsistent results, for example, a nonzero $A_{11}$ term implies an incorrect law where velocity depends on position, while the overall coefficient bias causes the model to underestimate the natural frequency and overestimate the damping ratio. Such

structural misidentifications can lead to flawed control laws and degraded system performance. In contrast, flow-consistent approach establishes an exact relation between discrete and continuous dynamics without requiring $T_s \to 0$, yielding accurate system parameters and preserving the correct physical quantities $(\omega_n, \omega_d, \zeta)$ across all sampling intervals, thereby ensuring both structural and physical fidelity.

### 6.3.2 Fixed point

The fixed point system is given by

$$\begin{aligned} \dot{x}_1 &= -3x_2 - x_1(x_1^2 + x_2^2), \\ \dot{x}_2 &= 3x_1 - x_2(x_1^2 + x_2^2). \end{aligned} \tag{46}$$

The fixed point system under this parameter exhibits pronounced nonlinear characteristics. Its sole equilibrium point resides at the origin, yet the state variables are strongly coupled through nonlinear terms. Consequently, system solutions in phase space manifest behaviors such as convergence and rotation, reflecting sensitivity to initial conditions. Precisely due to these inherent nonlinear interactions, this system serves as a paradigmatic model for investigating nonlinear stability, attractor structures, and complex dynamical evolution. The phase portraits of true dynamical system is shown in Supplementary Fig. 2.

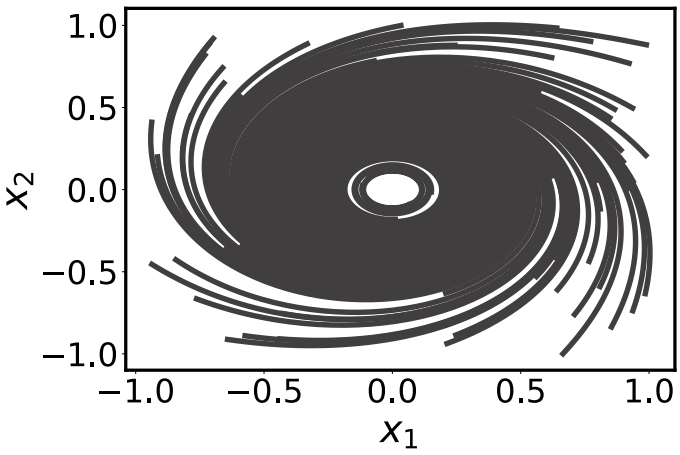


**Fig. 2**: Phase portrait of fixed point system

## System identification under different sampling periods

To comprehensively evaluate the effectiveness of the proposed identification approach, we generate time series data with sampling periods ranging from 0.1 s to 1.0 s in increments of 0.1 s, and conduct independent system identification for each sampling regime.

Supplementary Fig. 3 shows the phase portraits of the identified models as the sample period increases. While the results from the SINDy algorithm gradually diverge, the system found using the proposed approach stays almost the same and shows good agreement with the actual phase portrait.

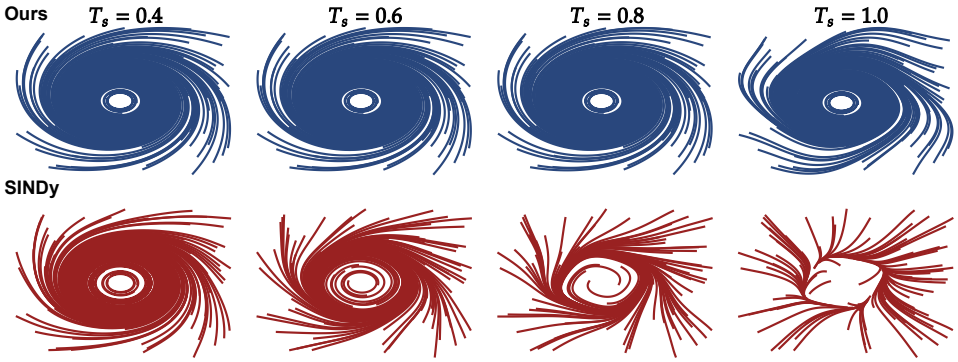


**Fig. 3**: Phase portrait of identified fixed point dynamics through SINDy and our approach from data with different sampling periods

## Validation of prediction performance

To validate the predictive capability of the identified model, we test it using the initial condition $(0.423, -0.336)$. For the model identified from the dataset with $T_s = 1.0$ s, we plot the corresponding trajectories and phase portraits (Supplementary Fig. 4).

## Spectral and eigenfunction analysis

We further investigate the Koopman generator identified by our approach. The spectral distribution is shown in Supplementary Fig. 5a, with dominant eigenvalues of $L$ highlighted in blue to indicate the principal modes of the system. As an example, the eigenfunction illustrated in Supplementary Fig. 5b corresponds to the eigenvalue

$$\lambda_1 = -0.06 - 3.00i,$$

and obtains its maximum at the stable point.

## The computation of NRMSE and MSE

To quantitatively evaluate the prediction performance of the identified models, we employ MSE and NRMSE as evaluation metrics.For MSE evaluation, we uniformly sample 100 initial conditions $\mathbf{x}_0 \in [-1, 1]^2$. For each initial condition, trajectories are simulated using the identified continuous-time models. The prediction horizon is chosen such that the total time equals that of the training trajectories, i.e., the

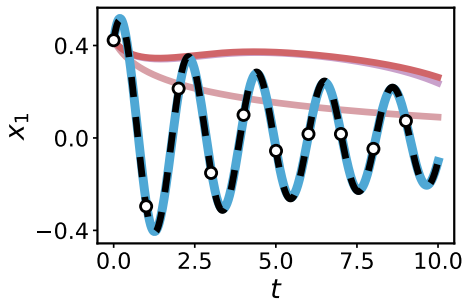


(a) Trajectories predicted from initial conditions $(0.423, -0.336)$

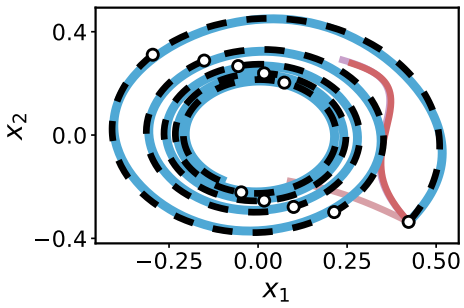


(b) Corresponding phase portraits of the trajectories

**Fig. 4**: Prediction of the identified models. Models are identified from data with $T_s = 1.0$ s. The ground-truth trajectory is shown as a black dashed curve, and the sampled states are indicated by hollow black circles. Predicted trajectories are generated by the identified models using HANDI (blue), SINDy (red), SR3 (purple), and PSE (pink), starting from the same initial condition $(0.423, -0.336)$.

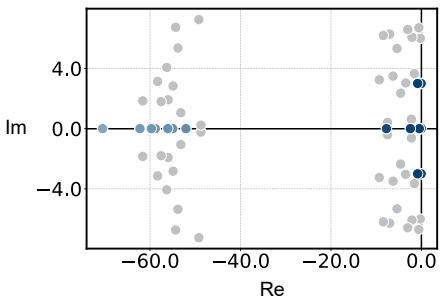


(a) Eigenvalues of Koopman Generator

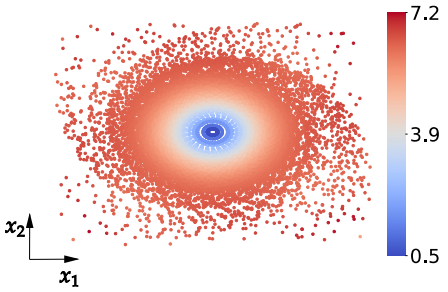


(b) Magnitude of the eigenfunction corresponding to the eigenvalue $\lambda_1 = -0.06 - 3.00i$

**Fig. 5**: Spectral analysis of the identified Koopman generator for fixed point dynamics.

number of simulated steps multiplied by the corresponding sampling interval. The NRMSE and MSE results of the four methods under different sampling intervals are summarized in Supplementary Table 10 and Supplementary Table 11.

**Table 10**: NRMSE of Fixed point system

| $dt$ | HANDI | SINDy | SR3 | PSE |
|---|---|---|---|---|
| 0.1 | 2.122e−4 | 8.455e−2 | 1.185e−1 | 0 |
| 0.2 | 3.253e−3 | 3.781e−1 | 4.130e−1 | 1.434e−1 |
| 0.3 | 7.051e−3 | 8.014e−1 | 8.118e−1 | 2.869e−1 |
| 0.4 | 5.035e−3 | 1.226e+0 | 1.226e+0 | 3.439e−1 |
| 0.5 | 1.429e−2 | 1.805e+0 | 1.896e+0 | 3.364e−1 |
| 0.6 | 1.252e−2 | 2.322e+0 | 2.3327e+0 | 5.020e−1 |
| 0.7 | 9.520e−2 | 1.884e+0 | 2.009e+0 | 5.221e−1 |
| 0.8 | 2.855e−2 | 1.971e+0 | 2.010e+0 | 7.418e−1 |
| 0.9 | 8.278e−2 | 2.416e+0 | 2.423e+0 | 1.473e+0 |
| 1.0 | 0.743e+0 | 2.744e+0 | 2.761e+0 | 2.515e+0 |

### 6.3.3 Limit cycle

The limit cycle system is characterized by the following equations:

$$\begin{aligned} \dot{x}_1 &= 3x_2 - x_1(x_1^2 + x_2^2 - 1), \\ \dot{x}_2 &= -3x_1 - x_2(x_1^2 + x_2^2 - 1), \end{aligned} \tag{47}$$

In this system, the dynamics are governed by a combination of linear oscillatory terms and nonlinear damping effects. The linear terms of $x_1$ and $x_2$ induce rotational motion in the phase space, while the nonlinear terms act to stabilize trajectories around $x_1^2 + x_2^2 = 1$. This results in a stable limit cycle, where all trajectories starting within a certain basin of attraction converge to a periodic orbit. The trajectory shape of this limit cycle is a perfect circle centered at the origin with a radius of one. This geometric feature arises from the balance between the linear and nonlinear components of the system, ensuring that any deviation from the circle is corrected over time. The robustness against perturbations makes this system a key concept in understanding self-sustained oscillations in various physical, biological, and engineering systems.The phase portraits of true dynamical system is shown in Supplementary Fig. 6.

### System identification under different sampling periods

We generate time series data with sampling periods $T_s \in \{0.1, 0.2, \ldots, 1.0\}$ and identify the system separately. Our proposed identification method achieves accurate recovery across all these sampling regimes.

**Table 11**: MSE (mean ± std) of Fixed point system

| $dt$ | HANDI | SINDy | SR3 | PSE |
|---|---|---|---|---|
| 0.1 | 1.340e−7 ± 2.624e−8 | 2.369e−4 ± 5.202e−5 | 2.571e−4 ± 6.703e−5 | 1.343e−13 ± 1.599e−13 |
| 0.2 | 4.404e−8 ± 1.897e−8 | 1.157e−2 ± 2.219e−3 | 1.147e−2 ± 2.271e−3 | 9.171e−3 ± 4.097e−3 |
| 0.3 | 1.535e−7 ± 3.140e−7 | 7.580e−2 ± 1.280e−2 | 7.591e−2 ± 1.263e−2 | 1.952e−2 ± 7.861e−3 |
| 0.4 | 6.370e−8 ± 1.425e−8 | 9.416e−2 ± 1.740e−2 | 9.416e−2 ± 1.740e−2 | 8.201e−2 ± 1.541e−2 |
| 0.5 | 8.626e−7 ± 8.052e−7 | 1.161e−1 ± 2.001e−2 | 1.159e−1 ± 2.083e−2 | 6.545e−2 ± 1.281e−2 |
| 0.6 | 3.525e−7 ± 5.656e−7 | 1.168e−1 ± 1.356e−2 | 1.169e−1 ± 1.359e−2 | 6.607e−2 ± 1.312e−2 |
| 0.7 | 2.426e−5 ± 2.226e−5 | 1.043e−1 ± 1.017e−2 | 1.064e−1 ± 1.047e−2 | 5.012e−2 ± 1.017e−2 |
| 0.8 | 4.014e−6 ± 4.392e−6 | 1.019e−1 ± 9.534e−3 | 1.017e−1 ± 9.506e−3 | 4.707e−2 ± 9.674e−3 |
| 0.9 | 1.946e−5 ± 2.647e−5 | 9.699e−2 ± 8.496e−3 | 9.703e−2 ± 8.498e−3 | 4.248e−2 ± 8.556e−3 |
| 1.0 | 2.341e−3 ± 2.941e−3 | 9.202e−2 ± 8.145e−3 | 9.209e−2 ± 8.153e−3 | 5.323e−2 ± 1.007e−2 |

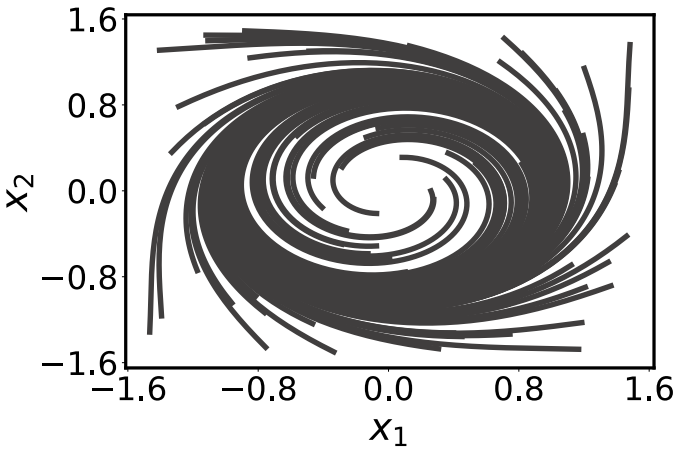


**Fig. 6**: Phase portrait of limit cycle system

Supplementary Fig. 7 shows the phase portraits of the identified models as the sample period increases. With the increase of the sampling period, the dynamic identified by SINDy show incorrect behavior, with the trajectory starting from the initial point collapsing directly onto the limit cycle without proper transient evolution, while our approach consistently preserves the correct dynamic of the system.

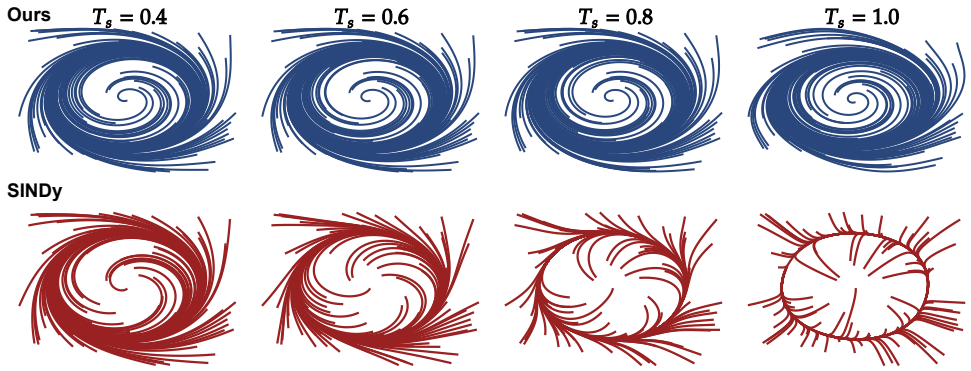


**Fig. 7**: Phase portrait of identified limit cycle dyanmics through SINDy and our approach from data with different sampling periods

### Validation of prediction performance

To validate the predictive capacity of the identified models, we test on symmetrical initial conditions $(1.257, -1.095)$. The system trajectories are predicted using the sampling interval of 1.0 s. We plot the trajectories (Supplementary Fig. 8a) and the corresponding phase portraits (Supplementary Fig. 8b).

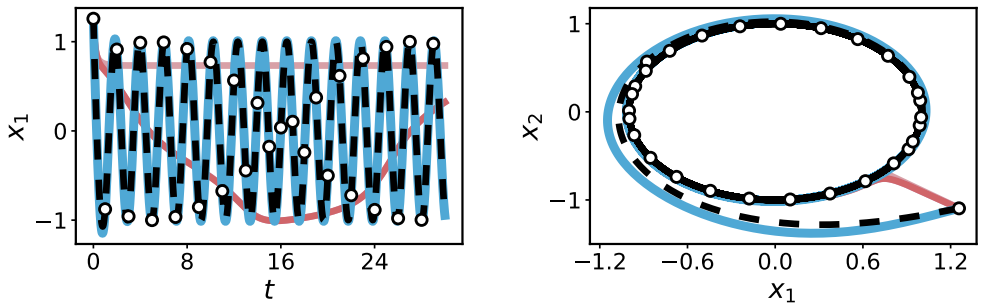


(a) Trajectories predicted from initial condition $(1.257, -1.095)$

(b) Corresponding phase portraits of the trajectories

**Fig. 8**: Prediction of the identified models. Models are identified from data with $T_s = 1.0$ s. The ground-truth trajectory is shown as a black dashed curve, and the sampled states are indicated by hollow black circles. Predicted trajectories are generated by the identified models using HANDI (blue), SINDy (red), SR3 (purple), and PSE (pink), starting from the same initial condition $(1.257, -1.095)$.

## Spectral and eigenfunction analysis

We further analyze the Koopman generator identified by our approach. The spectrum is shown in Supplementary Fig. 9a, while representative eigenfunctions are presented in Supplementary Fig. 9b. The spectrum reveals intrinsic dynamical properties. We highlight the eigenvalues along the real axis associated with transient decay toward the attractor. We also highlight the conjugate pair at $\pm 3i$, which corresponds to the intrinsic oscillation frequency of the limit cycle. The eigenfunction illustrated in the Supplementary Fig. 9b corresponds to the eigenvalue

$$\lambda_1 = -1.47 + 0.00i,$$

the real part of the associated eigenfunction vanishes precisely along the region of the state space occupied by the limit cycle attractor, providing a clear geometric signature of the stable periodic orbit.

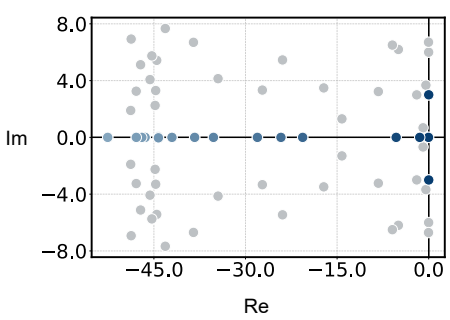


(a) Eigenvalues of Koopman Generator

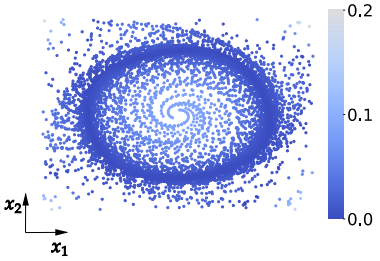


(b) Magnitude of the eigenfunction corresponding to the eigenvalue $\lambda_1 = -1.47 + 0.00i$

**Fig. 9**: Spectral analysis of the identified Koopman generator for limit cycle dynamics.

## The computation of NRMSE and MSE

To quantitatively evaluate the prediction performance of the identified models, we employ MSE and NRMSE as evaluation metrics.For MSE evaluation, we uniformly sample 100 initial conditions $\mathbf{x}_0 \in [-1.5, 1.5]^2$. For each initial condition, trajectories are simulated using the identified continuous-time models. The prediction horizon is chosen such that the total time equals that of the training trajectories, i.e., the number of simulated steps multiplied by the corresponding sampling interval. The NRMSE and MSE results of the four methods under different sampling intervals are summarized in Supplementary Table 12 and Supplementary Table 13.

**Table 12**: NRMSE of Limit cycle system

| $dt$ | HANDI | SINDy | SR3 | PSE |
|---|---|---|---|---|
| 0.1 | 3.290e-4 | 3.676e-2 | 3.636e-2 | 0.000e+0 |
| 0.2 | 2.570e-3 | 8.292e-2 | 8.170e-2 | 0.000e+0 |
| 0.3 | 1.221e-2 | 1.397e-1 | 1.399e-1 | 5.578e-1 |
| 0.4 | 4.859e-3 | 2.270e-1 | 2.266e-1 | 2.981e-1 |
| 0.5 | 6.664e-3 | 3.311e-1 | 3.307e-1 | 2.981e-1 |
| 0.6 | 1.479e-2 | 4.144e-1 | 4.139e-1 | 5.578e-1 |
| 0.7 | 1.374e-2 | 5.293e-1 | 5.287e-1 | 4.472e-1 |
| 0.8 | 3.988e-2 | 5.724e-1 | 5.723e-1 | 8.300e-1 |
| 0.9 | 4.975e-2 | 6.314e-1 | 6.315e-1 | 6.055e-1 |
| 1.0 | 1.683e-1 | 6.210e-1 | 6.210e-1 | 1.633e+0 |

### 6.3.4 Van der Pol

Mathematically, the Van der Pol system is governed by the equation

$$\begin{aligned} \dot{x}_1 &= x_2, \\ \dot{x}_2 &= -x_1 + \mu x_2(1 - x_1^2), \end{aligned} \tag{48}$$

where $\mu$ is the damping parameter that controls the strength of the nonlinear damping.The system exhibits rich dynamical behavior, including self-sustained oscillations and limit cycle dynamics. Its trajectories typically converge to a stable limit cycle, which is an attracting periodic orbit in the phase space. The Van der Pol system serves as a fundamental model for understanding nonlinear oscillatory phenomena in various fields, such as electrical circuits, biological systems, and mechanical vibrations. In our analysis, we set $\mu = 1$. The phase portraits of true dynamical system is shown in Supplementary Fig. 10.

### System identification under different sampling periods

To fully estimate the performance of the system identification methods, we generate time series data with sampling periods ranging from 0.1 s to 0.5 s in increments of 0.1 s, and perform system identification separately for each case.

Supplementary Fig. 11 shows the phase portraits of the identified models as the sample period increases. Trajectories obtained from the SINDy algorithm, when initialized in the vicinity of the unstable equilibrium (e.g., near the origin), fail to converge to the expected limit cycle, whereas the proposed method consistently identifies models that accurately capture the true system dynamics.

**Table 13**: MSE (mean ± std) of Limit cycle system

| *dt* | HANDI | SINDy | SR3 | PSE |
|---|---|---|---|---|
| 0.1 | 9.140e−8 ± 2.780e−8 | 1.834e−3 ± 8.470e−4 | 1.826e−3 ± 8.180e−4 | 1.380e−12 ± 8.620e−13 |
| 0.2 | 2.520e−7 ± 3.720e−7 | 1.177e−1 ± 2.381e−2 | 1.176e−1 ± 2.326e−2 | 3.080e−12 ± 1.560e−12 |
| 0.3 | 8.950e−6 ± 1.580e−5 | 9.028e−1 ± 6.517e−2 | 9.028e−1 ± 6.511e−2 | 3.722e−1 ± 1.481e−1 |
| 0.4 | 7.800e−6 ± 6.050e−6 | 9.057e−1 ± 6.587e−3 | 9.056e−1 ± 6.583e−3 | 9.313e−1 ± 1.434e−2 |
| 0.5 | 7.580e−5 ± 2.040e−5 | 9.461e−1 ± 8.987e−3 | 9.460e−1 ± 8.980e−3 | 9.090e−1 ± 1.008e−2 |
| 0.6 | 3.420e−5 ± 2.570e−5 | 1.002e+0 ± 5.786e−3 | 1.002e+0 ± 5.787e−3 | 9.419e−1 ± 1.583e−2 |
| 0.7 | 7.710e−5 ± 3.630e−5 | 9.817e−1 ± 5.253e−3 | 9.817e−1 ± 5.255e−3 | 1.048e+0 ± 1.404e−2 |
| 0.8 | 3.500e−5 ± 3.590e−4 | 1.017e+0 ± 8.230e−3 | 1.017e+0 ± 8.230e−3 | 1.004e+0 ± 2.235e−2 |
| 0.9 | 2.321e−3 ± 2.535e−3 | 9.907e−1 ± 7.093e−3 | 9.907e−1 ± 7.088e−3 | 1.038e+0 ± 2.705e−2 |
| 1.0 | 2.930e−3 ± 5.785e−3 | 9.870e−1 ± 7.660e−3 | 9.870e−1 ± 7.659e−3 | 9.169e−1 ± 1.610e−1 |

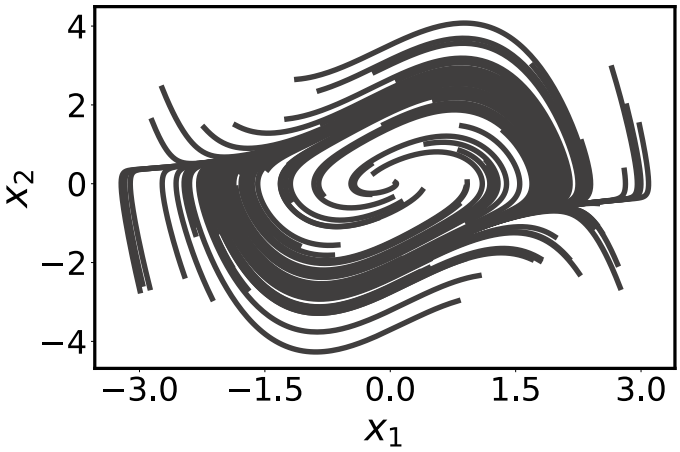


**Fig. 10**: Phase portrait of Van der Pol system

### Validation of prediction performance

To validate the predictive performance of the identified models, we test on symmetrical initial conditions $(0.005, 0.005)$, and predict the system trajectories at the sampling period of 0.5 s. The predicted trajectories, as illustrated in the Supplementary Fig. 12a and 12b, show the comparative performance of our model against the other methods.

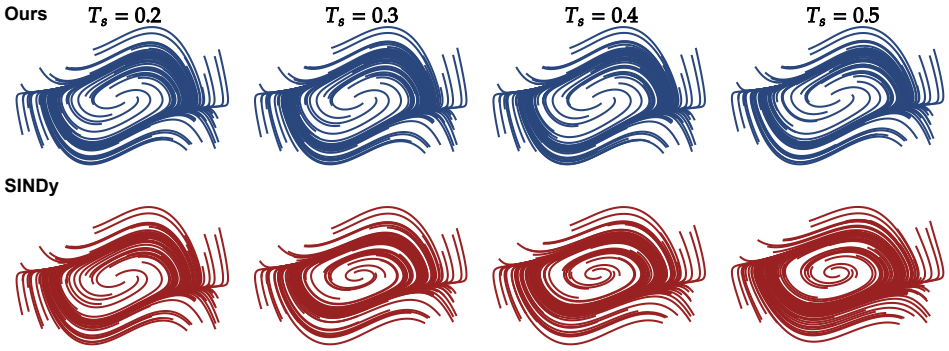


**Fig. 11**: Phase portrait of identified Van der Pol dynamics through SINDy and our approach from data with different sampling periods

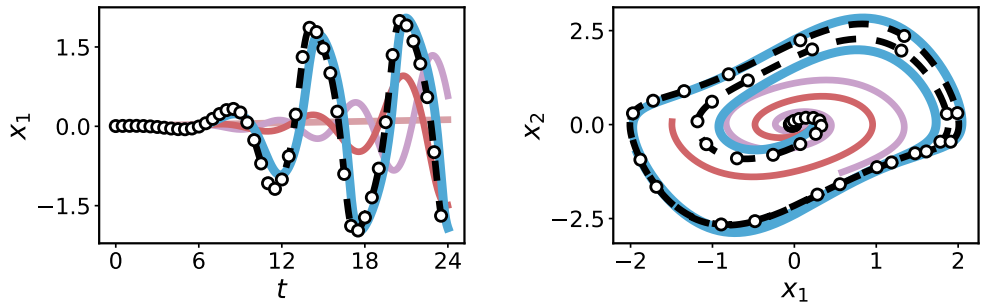


(a) Trajectories predicted from initial conditions $(0.005, 0.005)$

(b) Corresponding phase portraits of the trajectories

**Fig. 12**: Prediction of the identified models. Models are identified from data with $T_s = 0.5$ s. The ground-truth trajectory is shown as a black dashed curve, and the sampled states are indicated by hollow black circles. Predicted trajectories are generated by the identified models using HANDI (blue), SINDy (red), SR3 (purple), and PSE (pink), starting from the same initial condition $(0.005, 0.005)$.

## Spectral and eigenfunction analysis

We further analyze the Koopman generator identified by our approach. The spectrum is shown in Supplementary Fig. 13a, while representative eigenfunctions are presented in Supplementary Fig. 13b. For the van der Pol oscillator, the highlighted eigenvalues along the negative real axis correspond to the strong nonlinear damping modes that govern the transient relaxation toward the limit cycle. These modes reflect the characteristic stabilization mechanism of the amplitude of the system, where initial perturbations rapidly decay before settling into sustained oscillations. Meanwhile, eigenvalues that close to the imaginary axis and near the origin capture the intrinsic

phase dynamics of the self-sustained oscillation, encoding the fundamental frequency of the stable limit cycle. The eigenfunction illustrated in the Supplementary Fig. 13b corresponds to the eigenvalue

$$\lambda_1 = -3.96 + .00i,$$

the spatial structure of the real part of this eigenfunction similarly vanishes on the attractor, effectively delineating the extent of the limit cycle and highlighting its role as the dominant long-term dynamical feature.

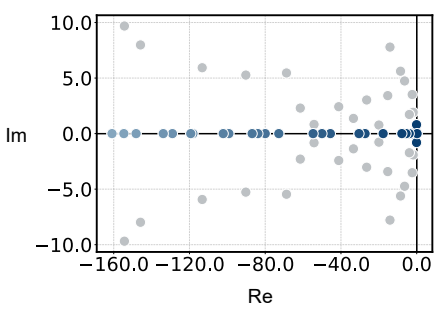


(a) Eigenvalues of Koopman Generator

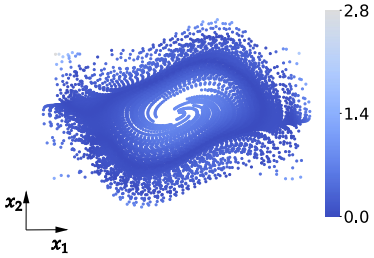


(b) Magnitude of the eigenfunction corresponding to the eigenvalue $\lambda_1 = -3.96 + .00i$

**Fig. 13**: Spectral analysis of the identified Koopman generator for Van der Pol system.

### The computation of NRMSE and MSE

To quantitatively evaluate the prediction performance of the identified models, we employ MSE and NRMSE as evaluation metrics. For MSE evaluation, we uniformly sample 100 initial conditions $\mathbf{x}_0 \in [-3, 3]^2$. For each initial condition, trajectories are simulated using the identified continuous-time models. The prediction horizon is chosen such that the total time equals that of the training trajectories, i.e., the number of simulated steps multiplied by the corresponding sampling interval. The NRMSE and MSE results of the four methods under different sampling intervals are summarized in Supplementary Table 14 and Supplementary Table 15.

### 6.3.5 Duffing system

The Duffing system is given by

$$\begin{aligned} \dot{x}_1 &= x_2, \\ \dot{x}_2 &= -\delta x_2 - \alpha x_1 - \beta x_1^3. \end{aligned} \tag{49}$$

**Table 14**: NRMSE of Van der Pol system

| $dt$ | HANDI | SINDy | SR3 | PSE |
|---|---|---|---|---|
| 0.1 | 5.216e-04 | 2.036e-02 | 3.874e-02 | 0.000e+00 |
| 0.2 | 2.947e-03 | 1.921e-02 | 3.885e-02 | 3.873e-01 |
| 0.3 | 4.858e-03 | 4.690e-02 | 8.343e-02 | 2.739e-01 |
| 0.4 | 1.358e-02 | 7.791e-02 | 1.029e-01 | 2.739e-01 |
| 0.5 | 2.435e-02 | 1.084e-01 | 1.221e-01 | 2.739e-01 |

**Table 15**: MSE (mean ± std) of Van der Pol system

| $dt$ | HANDI | SINDy | SR3 | PSE |
|---|---|---|---|---|
| 0.1 | 2.670e-5 ± 3.670e-5 | 1.633e-3 ± 1.216e-3 | 6.136e-3 ± 9.338e-3 | 1.290e-12 ± 2.010e-12 |
| 0.2 | 2.290e-4 ± 3.210e-4 | 6.875e-3 ± 4.248e-3 | 2.020e-2 ± 2.359e-2 | 4.545e+0 ± 2.863e+0 |
| 0.3 | 2.811e-3 ± 2.279e-3 | 4.974e-2 ± 5.672e-2 | 9.790e-2 ± 1.112e-1 | 5.129e+1 ± 4.562e+1 |
| 0.4 | 6.082e-2 ± 3.269e-2 | 1.579e-1 ± 1.406e-1 | 2.122e-1 ± 2.450e-1 | 8.887e+1 ± 7.842e+1 |
| 0.5 | 8.316e-2 ± 2.397e-1 | 6.671e-1 ± 2.910e-1 | 4.779e-1 ± 4.008e-1 | 1.370e+2 ± 1.212e+2 |

where $\delta$ is the damping coefficient, $\alpha$ and $\beta$ determine the linear and nonlinear stiffness. The Duffing system displays diverse nonlinear dynamics, including periodic, quasi-periodic, and chaotic responses, depending on the parameters. Its trajectories often exhibit bistability or chaotic switching, reflecting the sensitivity to initial conditions and parameter variations. Owing to these features, the Duffing system serves as a canonical model for nonlinear oscillations and chaos. In our study, we set $\delta = 0.5, \alpha = -5, \beta = 1$. The system exhibits two stable equilibrium points $(\pm\sqrt{5}, 0)$. The phase portraits of true dynamical system is shown in Supplementary Fig. 14.

### System identification under different sampling periods

First, we generate time series data with different sampling periods ($T_s = 0.1, 0.2, 0.3, 0.4$ s) and identify the system separately. Our proposed identification method achieves accurate recovery across all these sampling regimes.

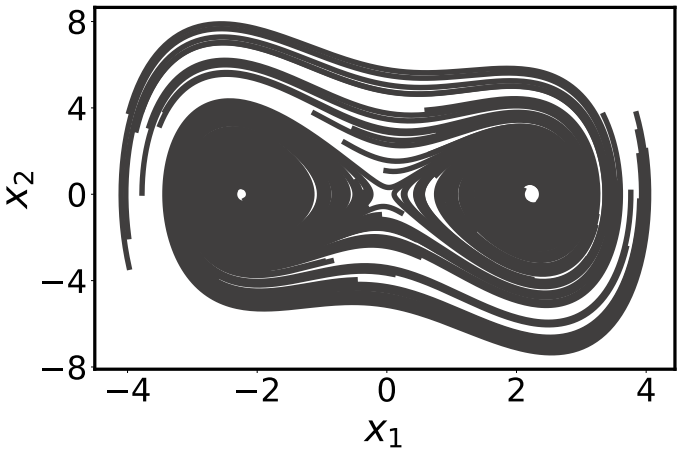


**Fig. 14**: Phase portrait of Duffing system

As the sampling period increases, the phase portraits of the identified models are shown in Supplementary Fig. 15. The system identified by our approach remains nearly invariant and closely resembles the true phase portrait, whereas the results from SINDy gradually deviate.

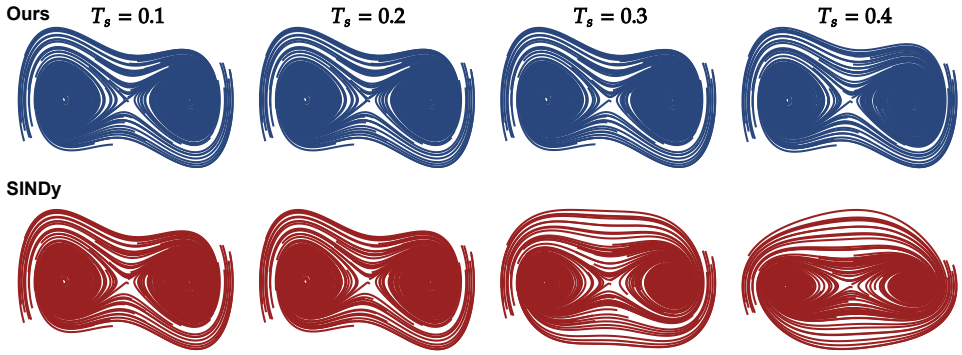


**Fig. 15**: Phase portrait of identified Duffing system through SINDy and our approach from data with different sampling periods

## Validation of prediction performance

To validate the predictive capability of the identified models, we test on symmetrical initial conditions $(4, -1)$. Using the models identified from data with $T_s = 0.3$ s, we plot the trajectories and the corresponding phase portraits (Supplementary Fig. 16).

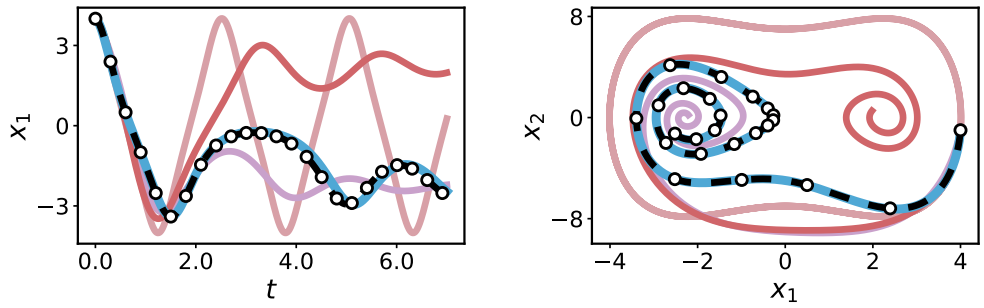


(a) Trajectories predicted from initial conditions $(4, -1)$

(b) Corresponding phase portraits of the trajectories

**Fig. 16**: Prediction of the identified models. Models are identified from data with $T_s = 0.3$ s. The ground-truth trajectory is shown as a black dashed curve, and the sampled states are indicated by hollow black circles. Predicted trajectories are generated by the identified models using HANDI (blue), SINDy (red), SR3 (purple), and PSE (pink), starting from the same initial condition $(4, -1)$.

### Spectral and eigenfunction analysis

We further analyze the Koopman generator identified by our approach. The spectrum is shown in Supplementary Fig. 17a, while representative eigenfunctions are presented in Supplementary Fig. 17b. The spectrum reveals intrinsic dynamical properties, and we highlight three dominant eigenvalues of $L$ that correspond to the principal modes of the system. The eigenfunction illustrated in Supplementary Fig. 17b corresponds to the eigenvalue

$$\lambda_1 = -0.01 + 0.00i,$$

the real part of eigenfunction partition the state space into regions associated with the two stable wells.

### The computation of NRMSE and MSE

To quantitatively evaluate the prediction performance of the identified models, we employ MSE and NRMSE as evaluation metrics. For MSE evaluation, we uniformly sample 100 initial conditions $\mathbf{x}_0 \in [-4, 4]^2$. For each initial condition, trajectories are simulated using the identified continuous-time models. The prediction horizon is chosen such that the total time equals that of the training trajectories, i.e., the number of simulated steps multiplied by the corresponding sampling interval. The NRMSE and MSE results of the four methods under different sampling intervals are summarized in Supplementary Table 16 and Supplementary Table 17.

### 6.3.6 Chemical autocatalysis

Autocatalysis represents an essential process of nonequilibrium self-organization in natural systems and is widely considered a key factor in the origin of life [21]. Accurate identification of the generation rate and the competing decay or inhibition rate

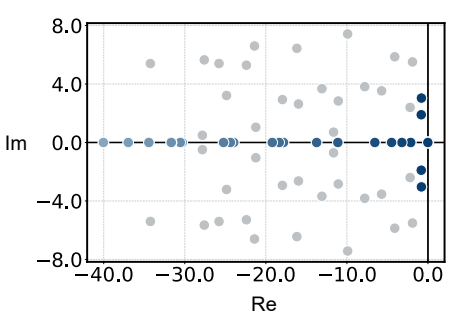


(a) Eigenvalues of Koopman Generator

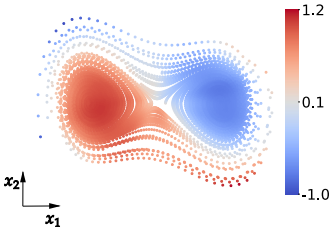


(b) Real part of the eigenfunction corresponding to the eigenvalue $\lambda_1 = -0.01 + 0.00i$

**Fig. 17**: Spectral analysis of the identified Koopman generator for Duffing dynamics.

**Table 16**: NRMSE of Duffing system

| *dt* | HANDI | SINDy | SR3 | PSE |
|---|---|---|---|---|
| 0.1 | 1.254e−4 | 2.587e−3 | 1.573e−2 | 6.285e−2 |
| 0.2 | 9.316e−5 | 1.190e−2 | 3.411e−2 | 6.285e−2 |
| 0.3 | 9.271e−4 | 6.670e−2 | 7.151e−2 | 6.285e−2 |
| 0.4 | 3.175e−3 | 1.659e−1 | 1.716e−1 | 6.285e−2 |

is essential for understanding reaction kinetics and designing reactors. However, it is challenging as autocatalytic systems often exhibit rapid initiation, and the characteristic timescale of their burst phase may be extremely short (from milliseconds to seconds), while conventional chemical analysis methods such as chromatography, nuclear magnetic resonance, or many sampling-and-analysis protocols typically require several seconds to minutes. This disparity results in data that is sparse relative to the reaction's rapid dynamics, limiting the ability to capture the full kinetics of the burst period [22, 23]. Here we consider an autocatalytic reaction in which one reactant remains approximately constant (with concentration $a_A$), while the concentration $x$ of another species promotes its own production but is ultimately limited by a competing back reaction [24].

We use the ODEBench system "Autocatalysis with one fixed abundant chemical" (system id = 6), whose scalar dynamics are

$$\dot{x} = k_e\, x - k_{-1}\, x^2, \qquad x(0) \in \{0.13,\ 2.24\}, \quad (k_e, k_{-1}) = (2.1,\ 0.5),$$

**Table 17**: MSE (mean ± std) of Duffing system

| *dt* | HANDI | SINDy | SR3 | PSE |
|---|---|---|---|---|
| 0.1 | 8.051e−6 ± 9.711e−6 | 1.209e−3 ± 1.686e−3 | 2.288e−2 ± 4.345e−2 | 4.141e−1 ± 5.311e−1 |
| 0.2 | 4.775e−5 ± 9.445e−5 | 1.127e−2 ± 8.313e−3 | 3.735e−1 ± 5.892e−1 | 2.503e+0 ± 2.790e+0 |
| 0.3 | 2.660e−3 ± 1.036e−2 | 1.575e+0 ± 2.083e+0 | 1.132e+0 ± 1.733e+0 | 5.094e+0 ± 4.703e+0 |
| 0.4 | 4.248e−1 ± 8.610e−1 | 3.030e+0 ± 3.087e+0 | 1.971e+0 ± 2.426e+0 | 6.970e+0 ± 6.314e+0 |

where $x(t)$ denotes the concentration of the chemical species $X$. The equation form and parameters are taken from Strogatz's textbook *Nonlinear Dynamics and Chaos*[25] (2nd ed., p. 39). This simple autocatalytic reaction represents a self-reinforcing process

$$A + X \to 2X,$$

in which the product $X$ catalyzes its own formation, while the substrate $A$ is assumed to remain in fixed abundance. Because the concentration of the substrate $A$ is maintained in large excess throughout the experiment, the bimolecular reaction effectively behaves as a pseudo–first-order process in $X$. Under this assumption, the concentration of $A$ remains approximately constant, $[A](t) \approx a_A$, allowing the true second-order rate $k_1[A]X$ to be written as

$$k_1[A]X = (a_A k_1)\, X = k_e\, X,$$

so that the growth term is governed by the *effective* rate constant $k_e = a_A k_1$. A schematic illustration of the reaction mechanism is shown in Supplementary Fig. 18.

### Data generation and noise modeling

Numerical integration is performed over $t \in [0, 20]$ s with 401 uniformly spaced samples, yielding a base sampling interval

$$\Delta t = \frac{20 - 0}{400} = 0.05 \text{ s}.$$

This corresponds to the configuration `t_eval = np.linspace(0, 20, 401)` in the generation script. The original implementation and configuration details are available in the official ODEBench repository: *https://github.com/GPBench/ODEBench*[26].

To assess identification robustness, zero-mean *multiplicative Gaussian noise* is applied to the numerical solution. For each sample $x(t_i)$, the observed value is

$$\tilde{x}(t_i) = x(t_i)\,\big(1 + \sigma\,\xi_i\big), \qquad \xi_i \sim \mathcal{N}(0, 1),$$

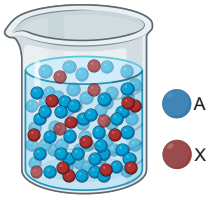


**Fig. 18**: Well-mixed schematic of the autocatalytic system with one fixed abundant reactant. Blue spheres denote the abundant substrate $A$; red spheres denote the autocatalyst/product $X$. The beaker highlights that $A$ is maintained in large excess while encounters $A + X \to 2X$ create additional $X$. Under this pseudo–first-order condition, the kinetics $\dot{x} = k_e x - k_{-1} x^2$ use the effective rate constant $k_e = a_A k_1$, reflecting self-amplified growth with quadratic saturation.

where $\sigma \in \{0, 0.01, 0.02, 0.03, 0.04, 0.05\}$ corresponds to relative noise levels of 0–5%. To emulate sparse sensing, trajectories are downsampled by a factor of 45 (keep every 45th point):

$$x^{\downarrow}(t_k) = x(t_0 + 45k\,\Delta t)\,, \qquad k = 0, 1, \ldots,$$

resulting in an effective sampling interval $T_s = 45\,\Delta t = 2.25$ s. The same downsampling procedure is applied independently to all noisy observation sets $\tilde{x}(t_i)$.

### Identified equations under noise (with error quantification)

Using HANDI on multiplicatively perturbed ($\sigma \in \{0, 1, 2, 3, 4, 5\}\%$) and downsampled trajectories, we identified the governing dynamics of the autocatalytic process as

$$\dot{x} = \hat{k}_e\, x - \hat{k}_{-1}\, x^2,$$

where $(\hat{k}_e, \hat{k}_{-1})$ are the recovered kinetic parameters under each noise condition. The true parameters are $(k_e, k_{-1}) = (2.1, 0.5)$. The identified equations for all six noise levels are

$$\begin{aligned}
&(0\%\text{ noise}) && \dot{x} = 2.10172\,x - 0.495336\,x^2,\\
&(1\%\text{ noise}) && \dot{x} = 2.00270\,x - 0.468931\,x^2,\\
&(2\%\text{ noise}) && \dot{x} = 2.00270\,x - 0.468931\,x^2,\\
&(3\%\text{ noise}) && \dot{x} = 2.18336\,x - 0.511338\,x^2,\\
&(4\%\text{ noise}) && \dot{x} = 2.10177\,x - 0.500079\,x^2,\\
&(5\%\text{ noise}) && \dot{x} = 2.10401\,x - 0.478132\,x^2.
\end{aligned}$$

Across all noise levels, the dominant first- and second-order terms remain correctly identified, and both coefficients show strong robustness even under higher noise.

## Trajectory comparison and validation

### *(a) Real trajectories (six noise configurations).*

Supplementary Fig. 19 shows the true trajectories for $\sigma = 0\%, 1\%, 2\%, 3\%, 4\%, 5\%$. Blue curves correspond to $x(0) = 0.13$; gray curves to $x(0) = 2.24$. Square markers indicate 45× downsampled samples.

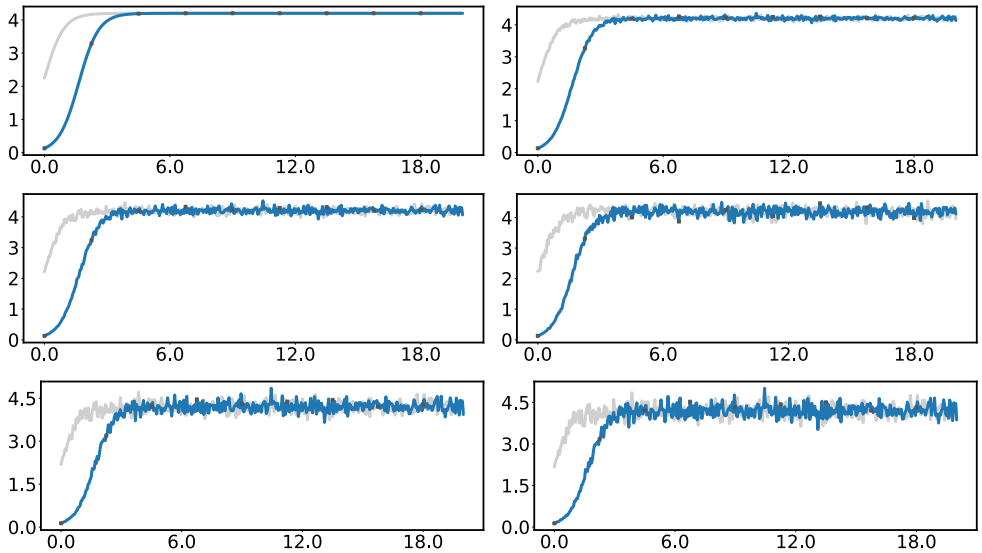


**Fig. 19**: True trajectories (real-only) for six noise levels (0%–5%). Blue: $x(0) = 0.13$; gray: $x(0) = 2.24$. Square markers: 45× downsampled points.

### *(b) Real vs. predicted trajectories (six noise configurations).*

For each noise level, the identified model is simulated and compared with the corresponding observations. The gray lines denote noisy trajectories, while the colored lines show model predictions. As illustrated in Supplementary Fig. 20, all predicted trajectories closely follow the observed trajectories and converge monotonically to the steady state $x^* = k_e/k_{-1} = 4.2$. This confirms that the identified models retain the correct autocatalytic behavior even under multiplicative perturbations and sparse sampling.

### *(c) Cross-method trajectory comparison.*

We further perform a cross-method comparison of the predicted trajectories under an identical noise-free setting. Supplementary Fig. 21 shows the true trajectories together with predictions by HANDI, EDMD, gEDMD, PSE, SINDy, SR3, and WSINDy, all simulated from the same initial conditions.

While HANDI, SINDy, SR3, and WSINDy accurately reproduce the logistic-type monotonic convergence to the steady state $x^* = 4.2$, EDMD and gEDMD exhibit

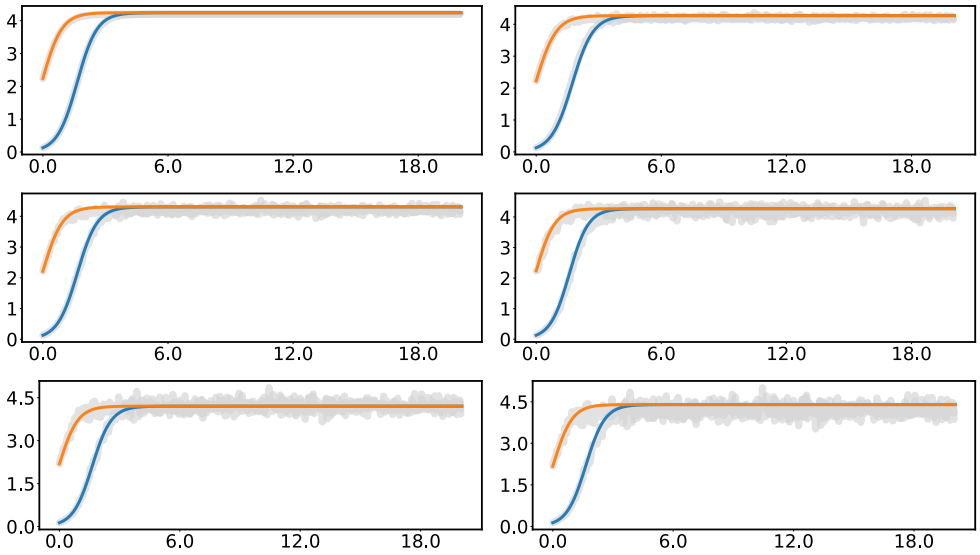


**Fig. 20**: Real (gray) vs. predicted (colored) trajectories under six noise levels (0%–5%). Despite multiplicative perturbations and sparse sampling (45× downsampling), the identified models reproduce the logistic-type monotonic convergence to $x^* = 4.2$.

severe divergence and fail to capture the correct asymptotic behavior due to unstable linear coefficients. PSE yields a qualitatively incorrect linear growth, reflecting the loss of nonlinear saturation.

### Physical parameter recovery

The regression coefficients are directly interpreted as the kinetic rate parameters

$$k_e \text{ (autocatalytic rate)}, \qquad k_{-1} \text{ (saturation or back reaction rate)}.$$

Estimation accuracy is quantified by the absolute relative errors

$$\varepsilon_{k_e} = \frac{|\,\hat{k}_e - k_e\,|}{k_e}, \qquad \varepsilon_{k_{-1}} = \frac{|\,\hat{k}_{-1} - k_{-1}\,|}{k_{-1}}.$$

In the noise-free setting (0% noise), the autocatalytic rate $k_e$ is recovered with high accuracy, as shown in Supplementary Table 18. HANDI achieves near-exact identification with relative errors below 1%, whereas SINDy and SR3 underestimate $k_e$ and WSINDy exhibits a moderate bias. In contrast, EDMD and gEDMD suffer from severe coefficient blow-up,indicating the instability of linear Koopman-based regression for this nonlinear kinetic system.

Robustness under measurement noise is further evaluated through the trajectory level and identified vector fields. Supplementary Table 19 and Supplementary Table 20 report the mean squared error (MSE) of two representative trajectories and error of

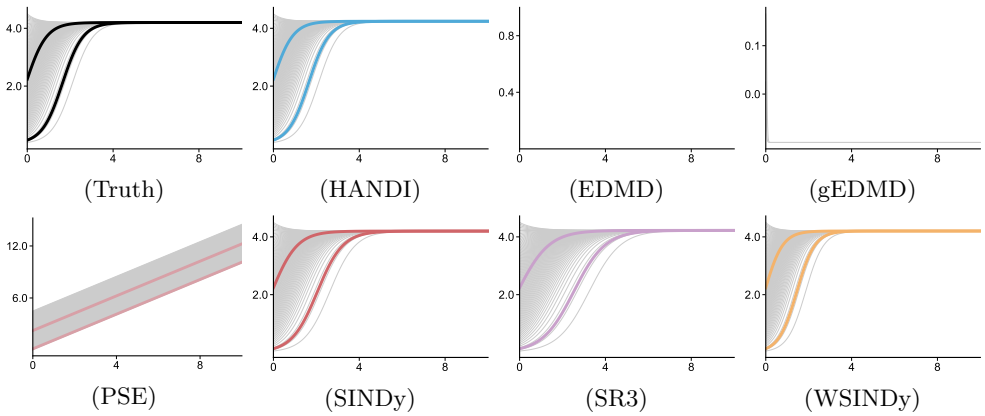


**Fig. 21**: Cross-method trajectory comparison for the autocatalytic system. The first panel shows the true trajectories, while the remaining seven panels show predictions by HANDI, EDMD, gEDMD, PSE, SINDy, SR3, and WSINDy from identical initial conditions. Gray curves correspond to background initial conditions, and colored thick curves highlight $x(0) = 0.13$ and $x(0) = 2.24$.

**Table 18**: Recovered kinetic parameters $k_e$ and $k_{-1}$ of different models (true values: $k_e = 2.100e+00$, $k_{-1} = 5.000e-01$).

| Methods | $\hat{k}_e$ | $\hat{k}_{-1}$ | $\varepsilon_{k_e}$ (%) | $\varepsilon_{k_{-1}}$ (%) |
|---|---|---|---|---|
| HANDI | 2.102e+00 | 4.953e-01 | 8.000e-02 | 9.300e-01 |
| SINDy | 1.683e+00 | 4.008e-01 | 1.984e+01 | 1.984e+01 |
| SR3 | 1.365e+00 | 3.231e-01 | 3.501e+01 | 3.537e+01 |
| WSINDy | 2.383e+00 | 5.675e-01 | 1.349e+01 | 1.349e+01 |
| PSE | 0.000e+00 | 0.000e+00 | 1.000e+02 | 1.000e+02 |
| EDMD | 5.974e+01 | -2.084e+02 | 2.745e+03 | 4.178e+04 |
| gEDMD | -5.114e+01 | -4.414e+02 | 2.535e+03 | 8.837e+04 |

identified vector fields for noise levels from 1% to 5%, respectively. HANDI consistently achieves the lowest MSE across all noise regimes, while SINDy and SR3 show progressively increasing errors as noise increases, whereas WSINDy exhibits noticeable instability. PSE and Koopman-based methods (EDMD, gEDMD) exhibit large errors dominated by structural model mismatch.

### 6.3.7 Language death

The language competition and extinction process can be modeled analogously to population dynamics, where the fraction of speakers of a given language evolves over time. Language use can shift rapidly, but measurements typically arrive only at decennial censuses or multi-year releases, resulting in intrinsically sparse temporal measurements [27].

**Table 19**: Trajectory-level MSE of two representative chemical autocatalysis trajectories under different noise levels.

| Methods | 1% | | 2% | | 3% | |
|---|---|---|---|---|---|---|
| | Traj 1 | Traj 2 | Traj 1 | Traj 2 | Traj 1 | Traj 2 |
| HANDI | 5.392e-03 | 4.529e-03 | 9.906e-03 | 1.080e-02 | 6.553e-03 | 4.905e-03 |
| SINDy | 7.988e-02 | 3.759e-03 | 1.253e-01 | 8.344e-03 | 5.057e-01 | 2.418e-02 |
| SR3 | 2.226e-01 | 9.287e-03 | 2.793e-01 | 1.223e-02 | 4.733e-01 | 2.217e-02 |
| WSINDy | 1.559e+01 | 1.230e+01 | 1.555e+01 | 1.139e+01 | 5.247e+00 | 2.820e-01 |
| PSE | 1.479e+01 | 3.662e+00 | 1.479e+01 | 3.662e+00 | 6.747e+01 | 9.790e+01 |
| EDMD | 1.000e+03 | 1.000e+03 | 1.000e+03 | 1.000e+03 | 1.577e+01 | 1.000e+03 |
| gEDMD | 1.000e+03 | 1.000e+03 | 1.000e+03 | 1.000e+03 | 1.000e+03 | 1.000e+03 |

| Methods | 4% | | 5% | |
|---|---|---|---|---|
| | Traj 1 | Traj 2 | Traj 1 | Traj 2 |
| HANDI | 9.000e-06 | 8.000e-06 | 3.523e-02 | 3.801e-02 |
| SINDy | 2.647e-01 | 2.729e-02 | 3.576e-01 | 4.208e-02 |
| SR3 | 5.019e-01 | 2.501e-02 | 6.690e-01 | 3.566e-02 |
| WSINDy | 1.553e+01 | 1.106e+01 | 1.553e+01 | 1.109e+01 |
| PSE | 1.479e+01 | 3.662e+00 | 1.479e+01 | 3.662e+00 |
| EDMD | 1.000e+03 | 1.000e+03 | 1.000e+03 | 1.000e+03 |
| gEDMD | 1.480e+01 | 1.000e+03 | 1.480e+01 | 1.000e+03 |

**Table 20**: Error of identified vector fields averaged over state space

| Method | $E_{L2}$ | $E_{\text{rel}}$ | $n_{\text{fail}}$ | $n_{\text{IC}}$ |
|---|---|---|---|---|
| HANDI | 2.361e-01 | 1.588e-01 | 0 | 100 |
| SINDy | 6.193e-01 | 4.163e-01 | 0 | 100 |
| SR3 | 7.793e-01 | 5.239e-01 | 0 | 100 |
| PSE | 1.488e+00 | 1.000e+00 | 0 | 100 |
| WSINDy | 1.607e+00 | 1.080e+00 | 0 | 100 |
| EDMD | 9.924e+04 | 6.672e+04 | 0 | 100 |
| gEDMD | 1.500e+04 | 1.008e+04 | 0 | 100 |

We use the ODEBench system "Language Death Model for Two Languages" (system id = 9), described by the scalar dynamics

$$\frac{dx}{dt} = (1 - x) \cdot c_0 - x \cdot c_1,$$

where $x(t)$ represents the proportion of the population speaking language 1. The constants $c_0$ and $c_1$ represent the switching rates between languages: $c_0$ is the rate of language 2 speakers switching to language 1, and $c_1$ is the rate of language 1 speakers switching to language 2. Accurately identifying these transition rates is crucial for revealing the mechanisms underlying language shift and for developing effective preservation policies. The equation parameters are given by

$$c_0 = 0.32, \qquad c_1 = 0.28,$$

and initial conditions are provided as $x(0) = 0.14$ and $x(0) = 0.55$, with constraints $0 < x < 1$ for the population proportion.


**Fig. 22**: Schematic illustration of the two-language competition model. Each head represents a speaker group. The left group says *"Hablemos en español!"* (Let's speak Spanish), while the right replies *"Qhichwata rimarisun!"* (Let's speak Quechua). The arrows symbolize the bidirectional switching between languages with rates $c_0$ (toward language 1) and $c_1$ (toward language 2).

### Data generation and noise modeling

Numerical integration is performed over $t \in [0, 10]$ s with 201 uniformly spaced samples using the LSODA solver, yielding a base sampling interval

$$\Delta t = \frac{10 - 0}{200} = 0.05 \text{ s}.$$

This corresponds to the configuration `t_eval = np.linspace(0, 10, 201)` in the generation script. The original implementation and configuration details are available in the official ODEBench repository: *https://github.com/GPBench/ODEBench*[26].

To assess identification robustness, zero-mean *multiplicative Gaussian noise* is applied to the numerical solution. For each sample $x(t_i)$, the observed value is

$$\tilde{x}(t_i) = x(t_i)\,\big(1 + \sigma\,\xi_i\big), \qquad \xi_i \sim \mathcal{N}(0, 1),$$

where $\sigma \in \{0, 0.01, 0.02, 0.03, 0.04, 0.05\}$ corresponds to relative noise levels of 0–5%.

To emulate sparse sensing, trajectories are downsampled by a factor of 40 (keeping every 40th point):

$$x^{\downarrow}(t_k) = x(t_0 + 40k\,\Delta t)\,, \qquad k = 0, 1, \ldots,$$

resulting in an effective sampling interval $T_s = 40\,\Delta t = 2.0$ s. The same downsampling procedure is applied independently to all noisy observation sets $\tilde{x}(t_i)$.

### Identified equations under noise (with error quantification)

Using HANDI on multiplicatively perturbed data downsampled by a factor of 40, we identify the parameters $c_0$ and $c_1$ for six noise levels ($\sigma = 0\%, 1\%, 2\%, 3\%, 4\%, 5\%$). The identified equations take the affine form

$$\dot{x} = -a\,x + b,$$

which corresponds to the analytical model $\dot{x} = (1 - x)c_0 - xc_1 = c_0 - (c_0 + c_1)x$. Matching coefficients gives $a = c_0 + c_1$ and $b = c_0$, from which both parameters can be recovered as

$$\hat{c}_0 = b, \qquad \hat{c}_1 = a - b.$$

The recovered coefficients from the identified equations are:

$$\begin{aligned}
&(0\%\text{ noise}) \quad \dot{x} = -0.600124\,x + 0.320036,\\
&(1\%\text{ noise}) \quad \dot{x} = -0.602037\,x + 0.318026,\\
&(2\%\text{ noise}) \quad \dot{x} = -0.595282\,x + 0.319871,\\
&(3\%\text{ noise}) \quad \dot{x} = -0.671719\,x + 0.348039,\\
&(4\%\text{ noise}) \quad \dot{x} = -0.724065\,x + 0.380552,\\
&(5\%\text{ noise}) \quad \dot{x} = -0.550505\,x + 0.310393.
\end{aligned}$$

Substituting into the recovery relations above yields the parameter estimates summarized in Supplementary Table 21.

**Table 21**: Identified coefficients and relative errors under six noise levels (downsampling $\times 40$). True values: $c_0 = 0.32$, $c_1 = 0.28$.

| Noise | $\hat{c}_0$ | $\hat{c}_1$ | $\varepsilon_{c_0}$ (%) | $\varepsilon_{c_1}$ (%) |
|---|---|---|---|---|
| 0% | 0.320036 | 0.280088 | 0.01 | 0.03 |
| 1% | 0.318026 | 0.284011 | 0.62 | 1.43 |
| 2% | 0.319871 | 0.275411 | 0.04 | 1.64 |
| 3% | 0.348039 | 0.323680 | 8.76 | 15.60 |
| 4% | 0.380552 | 0.343513 | 18.92 | 22.68 |
| 5% | 0.310393 | 0.240112 | 3.00 | 14.25 |

## Trajectory comparison and validation

***(a) Real trajectories (six noise configurations).***

Supplementary Fig. 23 shows the true trajectories of language 1 usage for noise levels $\sigma = 0\%, 1\%, 2\%, 3\%, 4\%, 5\%$. Blue curves correspond to the trajectory starting from $x_0(0) = 0.14$, while gray curves start from $x_0(0) = 0.55$. Square markers indicate $40\times$ downsampled samples. In all cases, the trajectories monotonically converge to the steady state $x^* = c_0/(c_0 + c_1) = 0.533$.

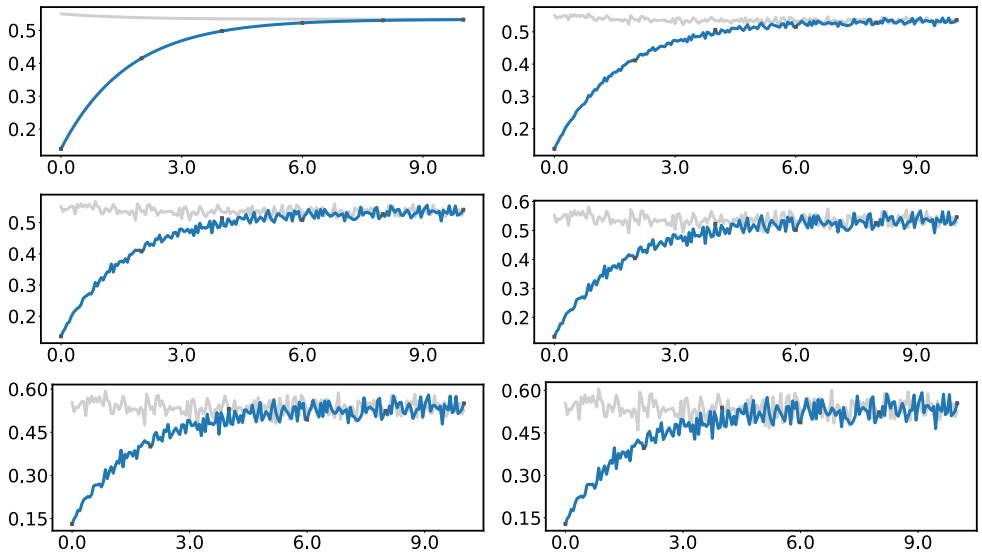


**Fig. 23**: True trajectories of language 1 speaker proportion for six noise levels (0%–5%). Blue: $x_0(0) = 0.14$; gray: $x_0(0) = 0.55$. Square markers: $40\times$ downsampled samples.

***(b) Real vs. predicted trajectories (six noise configurations).***

For each noise level, the identified model is simulated from the same initial conditions and compared against the corresponding noisy observations. Gray lines represent noisy data, while colored lines denote predictions from the recovered model. As shown in Supplementary Fig. 24, the predicted curves capture the correct qualitative convergence behavior even under extreme sparsity ($40\times$ downsampling). This confirms that the identified linear model

$$\dot{x}_0 = (1 - x_0)\hat{c}_0 - x_0\hat{c}_1$$

adequately reproduces the exponential relaxation dynamics of the two–language system.

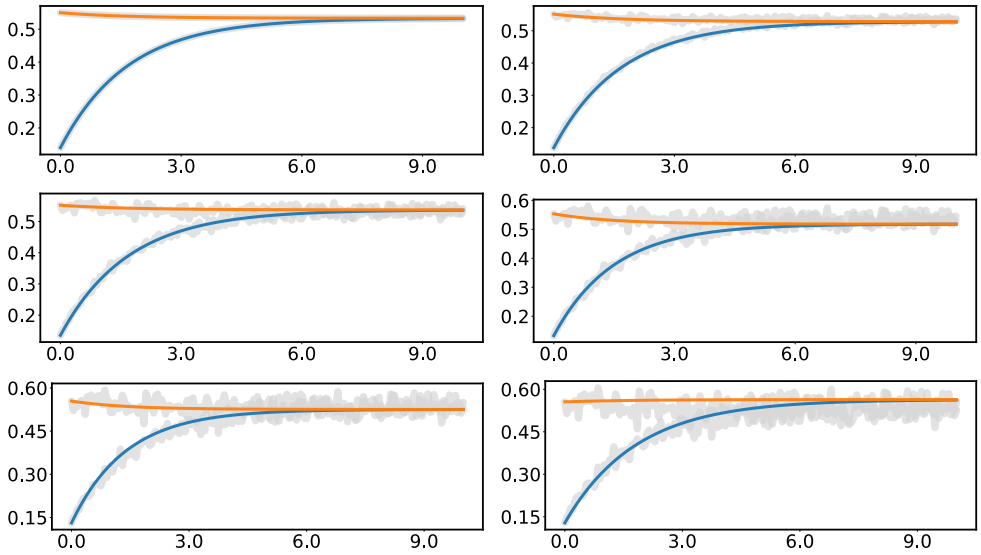


**Fig. 24**: Real (gray) vs. predicted (colored) trajectories under six noise levels (0%–5%). The identified models reproduce the qualitative exponential convergence of language 1 usage toward equilibrium $x^* \approx 0.53$, demonstrating robustness under multiplicative noise and 40× downsampling.

***(c) Cross-method trajectory comparison.***

We further compare the predicted trajectories of seven identification methods under an identical noise-free setting. Supplementary Fig. 25 shows the true trajectories together with predictions by HANDI, EDMD, gEDMD, PSE, SINDy, SR3, and WSINDy, all simulated from the same initial conditions.

For this linear and stable system, most methods successfully reproduce the monotonic convergence to the unique steady state, and their predicted trajectories closely overlap with the ground truth. In contrast, EDMD and gEDMD yield degenerate constant solutions and fail to capture the correct transient dynamics, reflecting severe instability of the learned linear operators.

## Physical parameter recovery

The regression coefficients are directly interpreted as the transition rate parameters

$c_0$ (inflow rate: language 2 → language 1), $c_1$ (outflow rate: language 1 → language 2).

These two parameters explicitly characterize the bidirectional switching dynamics in the language–competition model and are therefore of direct physical interest.

Estimation accuracy is quantified by the absolute relative errors

$$\varepsilon_{c_0} = \frac{|\,\hat{c}_0 - c_0\,|}{c_0}, \qquad \varepsilon_{c_1} = \frac{|\,\hat{c}_1 - c_1\,|}{c_1}.$$

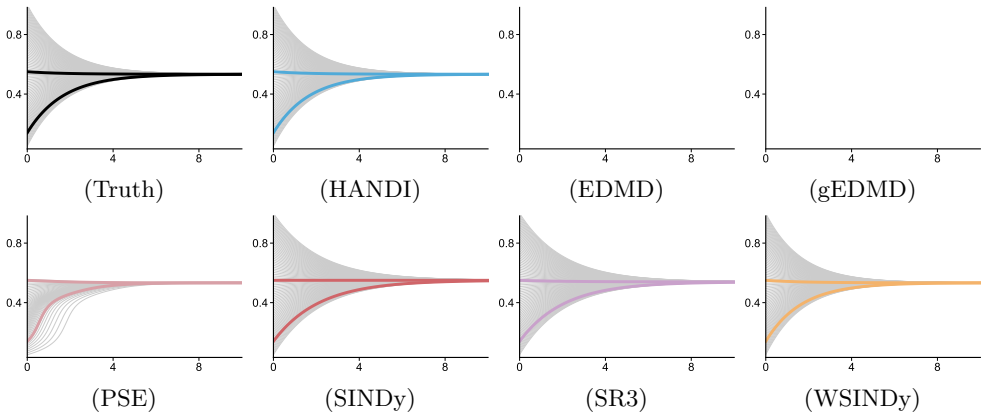


**Fig. 25**: Cross-method trajectory comparison for the id9-like linear system. The first panel shows the true trajectories, while the remaining seven panels show predictions by HANDI, EDMD, gEDMD, PSE, SINDy, SR3, and WSINDy from identical initial conditions. Gray curves correspond to background initial conditions, and colored thick curves highlight $x(0) = 0.14$ and $x(0) = 0.55$.

The ground-truth parameters are $(c_0, c_1) = (0.32, 0.28)$.

The recovered transition rates and their corresponding relative errors in the noise-free setting (0% noise) are summarized in Supplementary Table 22. Under clean measurements, HANDI achieves accurate identification of both parameters with low relative errors. In contrast, SINDy, SR3, and WSINDy exhibit moderate degradation, while PSE and Koopman-based methods (EDMD, gEDMD) suffer from severe coefficient distortion or numerical blow-up.

**Table 22**: Recovered transition rate parameters $c_0$ and $c_1$ in the language–competition model (true values: $c_0 = 0.32$, $c_1 = 0.28$).

| Methods | $\hat{c}_0$ | $\hat{c}_1$ | $\varepsilon_{c_0}$ (%) | $\varepsilon_{c_1}$ (%) |
|---|---|---|---|---|
| HANDI | 3.200e-01 | 2.801e-01 | 1.000e-02 | 3.000e-02 |
| SINDy | 2.592e-01 | 2.120e-01 | 1.901e+01 | 2.427e+01 |
| SR3 | 2.631e-01 | 2.245e-01 | 1.778e+01 | 1.981e+01 |
| WSINDy | 3.223e-01 | 2.820e-01 | 7.200e-01 | 7.300e-01 |
| PSE | -1.133e+00 | 1.133e+00 | 4.542e+02 | 3.048e+02 |
| EDMD | -1.200e-02 | 6.893e+03 | 1.038e+02 | 2.462e+06 |
| gEDMD | -2.094e+04 | 3.743e+05 | 6.543e+06 | 1.337e+08 |

As direct parameter regression becomes increasingly ill-conditioned in the presence of measurement noise, robustness under noisy observations is instead evaluated at the trajectory level. Supplementary Table 23 and Supplementary Table 24 report the

**Table 23**: Trajectory-level MSE of two representative trajectories under different noise levels.

| Methods | 1% | | 2% | | 3% | |
|---|---|---|---|---|---|---|
| | Traj 1 | Traj 2 | Traj 1 | Traj 2 | Traj 1 | Traj 2 |
| HANDI | 1.800e-05 | 1.900e-05 | 9.000e-06 | 1.200e-05 | 9.700e-05 | 1.860e-04 |
| SINDy | 2.640e-04 | 3.170e-04 | 3.420e-04 | 4.640e-04 | 4.400e-04 | 6.610e-04 |
| SR3 | 2.630e-04 | 3.200e-05 | 3.380e-04 | 3.400e-05 | 4.310e-04 | 3.700e-05 |
| WSINDy | 1.100e-04 | 1.500e-05 | 6.610e-04 | 6.200e-05 | 2.443e-03 | 1.550e-04 |
| PSE | 1.159e-01 | 8.000e-05 | 1.904e-03 | 6.000e-06 | 1.255e-02 | 2.570e-04 |
| EDMD | 1.000e+03 | 1.000e+03 | 1.000e+03 | 1.000e+03 | 1.000e+03 | 1.000e+03 |
| gEDMD | 1.000e+03 | 1.000e+03 | 1.000e+03 | 1.000e+03 | 1.000e+03 | 1.000e+03 |

| Methods | 4% | | 5% | |
|---|---|---|---|---|
| | Traj 1 | Traj 2 | Traj 1 | Traj 2 |
| HANDI | 1.220e-04 | 5.400e-05 | 4.700e-04 | 6.890e-04 |
| SINDy | 5.610e-04 | 9.200e-04 | 7.060e-04 | 1.252e-03 |
| SR3 | 5.460e-04 | 4.200e-05 | 6.850e-04 | 5.000e-05 |
| WSINDy | 8.966e-03 | 3.250e-04 | 5.053e-02 | 6.700e-04 |
| PSE | 1.204e-01 | 3.180e-04 | 1.233e-01 | 3.830e-04 |
| EDMD | 1.000e+03 | 1.000e+03 | 1.000e+03 | 1.000e+03 |
| gEDMD | 1.000e+03 | 1.000e+03 | 1.000e+03 | 1.000e+03 |

**Table 24**: Error of identified vector fields averaged over state space.

| Method | $E_{L2}$ | $E_{\text{rel}}$ | $n_{\text{fail}}$ | $n_{\text{IC}}$ |
|---|---|---|---|---|
| HANDI | 2.283e-02 | 1.184e-01 | 0 | 100 |
| SINDy | 7.117e-02 | 3.690e-01 | 0 | 100 |
| SR3 | 5.665e-02 | 2.938e-01 | 0 | 100 |
| PSE | 1.336e+12 | 6.930e+12 | 0 | 100 |
| WSINDy | 1.629e-01 | 8.447e-01 | 0 | 100 |
| EDMD | 4.523e+03 | 2.345e+04 | 0 | 100 |
| gEDMD | 7.247e+06 | 3.758e+07 | 0 | 100 |

mean squared error (MSE) of two representative trajectories and the error of identified vector fields for noise levels ranging from 1% to 5% respectively. Consistent with the noise-free parameter recovery results, HANDI maintains the lowest MSE across all noise regimes, with errors remaining several orders of magnitude smaller than those of competing methods.

### 6.3.8 SIR epidemic

Disease transmission can vary on day-level timescales, while surveillance data are typically reported in weekly aggregates with reporting delays [28], making the measurements temporally sparse. We use the ODEBench system "SIR Infection Model Only for Healthy and Sick" (system id = 31), whose simplified two–variable dynamics describe the interaction between the healthy ($x_1$) and infected ($x_2$) populations:

$$\begin{aligned}\dot{x}_1 &= -\,k\,x_1 x_2,\\ \dot{x}_2 &= k\,x_1 x_2 - \gamma\,x_2,\end{aligned}$$

where $x_1(t)$ and $x_2(t)$ denote the number (or normalized proportion) of healthy and infected individuals, respectively. The parameters are $k = \beta/N = 0.4$ (effective contact rate, $\text{Person}^{-1} \cdot \text{Time}^{-1}$) and $\gamma = 0.314$ (recovery rate, $\text{Time}^{-1}$), corresponding to the canonical two–compartment SIR model (Strogatz, p. 188). Initial conditions are $(x_1, x_2) = (7.2, 0.98)$ and $(20, 12.4)$, both satisfying $x_1 > 0, x_2 > 0$.

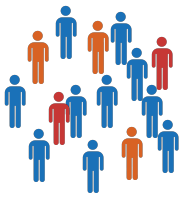

**Fig. 26**: Schematic representation of the simplified SIR infection model with only two compartments: healthy individuals ($x_1$, shown in blue) and infected individuals ($x_2$, shown in red). The infection process transfers individuals from the healthy to the infected group at rate $k\,x_1 x_2$, while recovery occurs from the infected group at rate $\gamma\,x_2$.

### Data generation and noise modeling

Numerical integration was carried out for $t \in [0, 10]$ s with 201 uniform samples using the LSODA solver, yielding the base sampling interval

$$\Delta t = \frac{10 - 0}{200} = 0.05 \text{ s}.$$

This corresponds to `t_eval = np.linspace(0,10,201)` in the ODEBench generator (https://github.com/GPBench/ODEBench)[26].

To assess robustness, multiplicative Gaussian noise is applied to the state variables:

$$\tilde{x}(t_i) = x(t_i)\big(1 + \sigma\xi_i\big), \qquad \xi_i \sim \mathcal{N}(0,1),$$

with $\sigma \in \{0, 0.01, 0.02, 0.03, 0.04, 0.05\}$ giving 0–5% noise levels. Each noisy trajectory is then downsampled by a factor of 6, resulting in the sampling interval $T_s = 6\Delta t = 0.3\,\mathrm{s}$.

### Identified equations under noise (with error quantification)

HANDI yields the following identified equations for noise levels $\sigma = 0\%, 1\%, 2\%, 3\%, 4\%, 5\%$:

$$(0\%)\ \begin{cases} \dot{x}_1 = -0.336855\,x_1x_2 - 0.233229\,x_1 - 0.0184153\,x_1^2 + 0.001689\,x_2 - 0.000226\,x_2^2, \\ \dot{x}_2 = 0.340060\,x_1x_2 - 0.313728\,x_2 + 0.196023\,x_1 + 0.021283\,x_1^2 + 8.1\times10^{-5}\,x_2^2; \end{cases}$$

$$(1\%)\ \begin{cases} \dot{x}_1 = -0.418462\,x_1x_2 - 0.119675\,x_1 + 0.063187\,x_1^2 - 0.004766\,x_2 + 0.000416\,x_2^2, \\ \dot{x}_2 = 0.362881\,x_1x_2 - 0.337947\,x_2 + 0.238106\,x_1 - 0.007378\,x_1^2 + 0.001509\,x_2^2; \end{cases}$$

$$(2\%)\ \begin{cases} \dot{x}_1 = -0.431484\,x_1x_2 + 0.102561\,x_1 + 0.0271924\,x_1^2 - 0.0102016\,x_2 + 0.000724615\,x_2^2, \\ \dot{x}_2 = 0.404992\,x_1x_2 - 0.337159\,x_2 + 0.100011\,x_1 - 0.0209051\,x_1^2 + 0.00141335\,x_2^2; \end{cases}$$

$$(3\%)\ \begin{cases} \dot{x}_1 = 0.430106\,x_1 - 0.422872\,x_1x_2 - 0.0454488\,x_2 - 0.0241717\,x_1^2 + 0.00286195\,x_2^2, \\ \dot{x}_2 = 0.374143\,x_1x_2 - 0.336812\,x_2 - 0.0825472\,x_1 + 0.0335469\,x_1^2 + 0.00192518\,x_2^2; \end{cases}$$

$$(4\%)\ \begin{cases} \dot{x}_1 = -0.813425\,x_1 - 0.359856\,x_1x_2 + 0.070071\,x_2 + 0.061029\,x_1^2 - 0.004373\,x_2^2, \\ \dot{x}_2 = -0.436824\,x_1 - 0.345413\,x_2 + 0.335976\,x_1^2 + 0.196385\,x_1x_2 + 0.002533\,x_2^2; \end{cases}$$

$$(5\%)\ \begin{cases} \dot{x}_1 = 0.847616\,x_1 - 0.436800\,x_1x_2 - 0.160162\,x_1^2 - 0.017330\,x_2 + 0.001004\,x_2^2, \\ \dot{x}_2 = 0.434672\,x_1x_2 - 0.369540\,x_2 - 0.272873\,x_1 + 0.097599\,x_1^2 + 0.003302\,x_2^2. \end{cases}$$

### Trajectory comparison and validation

***(a) Real trajectories.***

Supplementary Fig. 27 presents the true trajectories for both $x_1(t)$ (healthy, blue) and $x_2(t)$ (infected, orange) under six noise levels (0–5%). Square markers denote the 6× downsampled samples. Both populations evolve monotonically toward equilibrium: the infected group decays while the healthy group approaches its asymptotic value.

***(b) Real vs. predicted trajectories.***

Supplementary Fig. 28 compares the identified–model predictions (colored) with noisy observations (gray). Across all noise levels, the reconstructed trajectories closely follow the true evolution and converge to the correct equilibrium values, confirming that

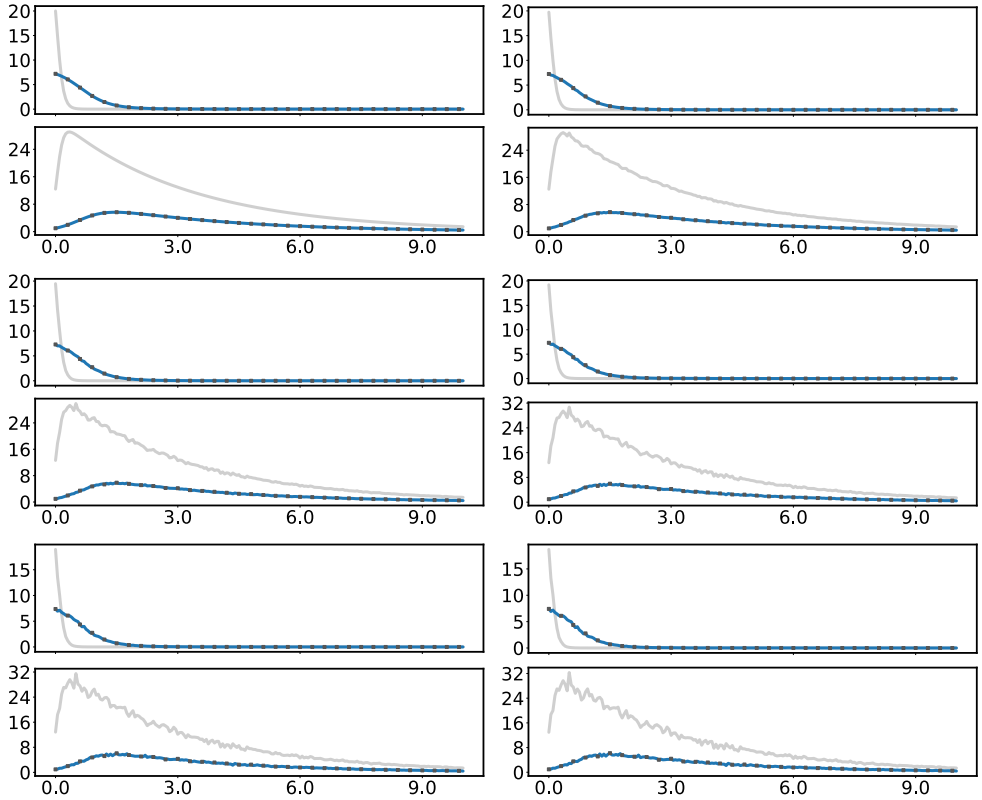


**Fig. 27**: True trajectories for the SIR model (0–5% noise). Blue: $x_1$ (healthy); orange: $x_2$ (infected). Square markers: 6× downsampled points.

the HANDI framework successfully identifies the effective transmission and recovery dynamics.

***(c) Cross-method vector-field comparison.***

We further compare the recovered vector fields of seven identification methods for the SIR-like epidemic system. Supplementary Fig. 29 shows the true vector field together with the recovered fields by HANDI, EDMD, gEDMD, PSE, SINDy, SR3, and WSINDy, all evaluated over the same phase-space region and from identical initial conditions.

HANDI, PSE, and WSINDy accurately reproduce the global flow structure, and their predicted trajectories closely follow the true epidemic decay paths. In contrast, EDMD and gEDMD produce severely distorted vector fields with incorrect flow directions and spurious trends, leading to qualitatively wrong bahaviors. SR3 and SINDy fit one training trajectory but fail to recover the correct curvature of the vector field, resulting in noticeable deviations in the phase-space geometry.

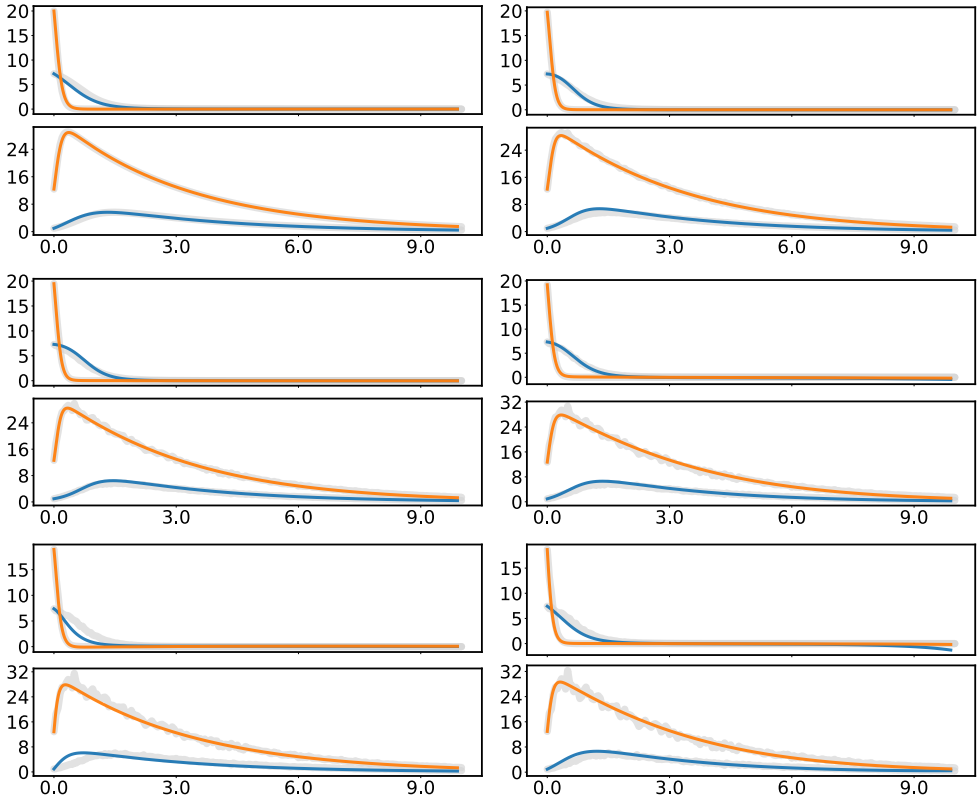


**Fig. 28**: Real (gray) vs. predicted (colored) trajectories for the SIR model under six noise levels. Identified models reproduce the infection–recovery dynamics and steady–state behavior.

### Physical parameter recovery

In the identified SIR system, the two physical parameters correspond to the effective contact rate $k = \beta/N$ (Person$^{-1}$·Time$^{-1}$) and the recovery rate $\gamma$ (Time$^{-1}$):

$$\dot{x}_1 = -k\, x_1 x_2, \qquad \dot{x}_2 = k\, x_1 x_2 - \gamma x_2.$$

The infection rate $k$ quantifies the transmission intensity between susceptible and infected individuals, while $\gamma$ characterizes the rate at which infected individuals recover or are removed from the infectious pool. Both parameters are therefore of direct epidemiological significance.

To enhance robustness in coefficient interpretation, we estimate the effective contact rate by symmetrizing the bilinear interaction terms appearing in the two governing equations,

$$\hat{k} \;=\; \tfrac{1}{2}\big(\big|\mathrm{coeff}_{x_1x_2}(\dot{x}_1)\big| + \mathrm{coeff}_{x_1x_2}(\dot{x}_2)\big)\,, \qquad \hat{\gamma} \;=\; \big|\mathrm{coeff}_{x_2}(\dot{x}_2)\big|.$$

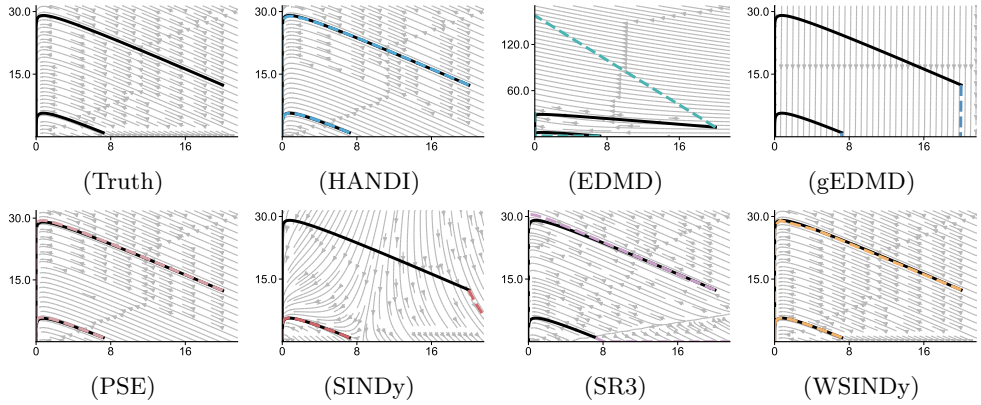


**Fig. 29**: Cross-method vector-field comparison for the SIR-like epidemic system. The first panel shows the true vector field, while the remaining seven panels show recovered vector fields by HANDI, EDMD, gEDMD, PSE, SINDy, SR3, and WSINDy. Black solid curves indicate true trajectories, and colored dashed curves denote predicted trajectories from identical initial conditions.

**Table 25**: Recovered SIR parameters under noise-free observations (true values: $k = 4.000e-01$, $\gamma = 3.140e-01$).

| Methods | $\hat{k}$ | $\hat{\gamma}$ | $\varepsilon_k$ (%) | $\varepsilon_\gamma$ (%) |
|---|---|---|---|---|
| HANDI | 3.401e-01 | 3.137e-01 | 1.499e+01 | 9.000e-02 |
| SINDy | -3.197e-01 | 3.008e-01 | 1.799e+02 | 4.190e+00 |
| SR3 | 6.962e-01 | 4.949e-01 | 7.405e+01 | 5.762e+01 |
| WSINDy | 1.200e+01 | 9.420e+00 | 2.900e+03 | 2.900e+03 |
| PSE | 0.000e+00 | 0.000e+00 | 1.000e+02 | 1.000e+02 |
| EDMD | -1.350e-01 | 7.476e+00 | 1.338e+02 | 2.281e+03 |
| gEDMD | 1.000e-05 | 4.316e-02 | 1.000e+02 | 8.625e+01 |

The ground-truth parameters are $k = 0.4 = \beta/N$ and $\gamma = 0.314$.

The recovered parameters under noise-free observations (0% noise) are summarized in Supplementary Table 25. HANDI accurately identifies the recovery rate $\gamma$ and effective contact rate $k$ with lower relative error than baseline methods. In contrast, SINDy, SR3, and Koopman-based methods (EDMD, gEDMD) yield substantially distorted or non-physical parameter values.epidemiological rates under unconstrained regression.

As direct parameter estimation becomes increasingly ill-conditioned in the presence of measurement noise, robustness under noisy observations is assessed at the trajectory level. Supplementary Table 26 and Supplementary Table 27 report the mean squared error (MSE) of two representative SIR trajectories and error of identified vector fields for noise levels ranging from 1% to 5%, respectively. Consistent with the noise-free parameter recovery results, HANDI maintains stable trajectory prediction

**Table 26**: Trajectory-level MSE of two representative SIR trajectories under different noise levels.

| Methods | 1% | | 2% | | 3% | |
|---|---|---|---|---|---|---|
| | Traj 1 | Traj 2 | Traj 1 | Traj 2 | Traj 1 | Traj 2 |
| HANDI | 1.072e-01 | 2.347e-02 | 4.816e-02 | 1.580e-02 | 5.461e-01 | 6.309e-02 |
| SINDy | 3.400e-04 | 1.000e+03 | 1.656e-03 | 1.000e+03 | 7.442e-03 | 1.000e+03 |
| SR3 | 1.000e+03 | 1.755e-01 | 1.000e+03 | 1.755e-01 | 1.000e+03 | 2.093e-01 |
| WSINDy | 1.000e+03 | 7.770e+01 | 1.000e+03 | 7.815e+01 | 1.000e+03 | 7.947e+01 |
| PSE | 3.019e+00 | 7.581e+01 | 3.019e+00 | 7.581e+01 | 3.019e+00 | 7.581e+01 |
| EDMD | 1.000e+03 | 1.000e+03 | 1.000e+03 | 1.000e+03 | 1.000e+03 | 1.000e+03 |
| gEDMD | 2.587e+01 | 2.367e+02 | 2.582e+01 | 2.346e+02 | 2.576e+01 | 2.310e+02 |

| Methods | 4% | | 5% | |
|---|---|---|---|---|
| | Traj 1 | Traj 2 | Traj 1 | Traj 2 |
| HANDI | 5.484e-01 | 2.595e-01 | 2.262e-01 | 1.748e-01 |
| SINDy | 9.384e-03 | 1.000e+03 | 1.108e-02 | 1.000e+03 |
| SR3 | 1.000e+03 | 2.093e-01 | 1.000e+03 | 2.456e-01 |
| WSINDy | 1.000e+03 | 7.947e+01 | 5.702e+00 | 7.703e+01 |
| PSE | 3.019e+00 | 7.581e+01 | 3.019e+00 | 7.581e+01 |
| EDMD | 1.000e+03 | 1.000e+03 | 1.000e+03 | 1.000e+03 |
| gEDMD | 2.576e+01 | 2.310e+02 | 2.580e+01 | 2.333e+02 |

**Table 27**: Error of identified vector fields averaged over state space.

| Method | $E_{L2}$ | $E_{\text{rel}}$ | $n_{\text{fail}}$ | $n_{\text{IC}}$ |
|---|---|---|---|---|
| HANDI | 3.924e+01 | 3.132e-01 | 0 | 6400 |
| SINDy | 3.378e+02 | 2.696e+00 | 0 | 6400 |
| SR3 | 4.440e+01 | 3.544e-01 | 0 | 6400 |
| PSE | 7.868e+01 | 6.279e-01 | 0 | 6400 |
| WSINDy | 3.633e+03 | 2.900e+01 | 0 | 6400 |
| EDMD | 3.477e+07 | 2.775e+05 | 0 | 6400 |
| gEDMD | 1.419e+02 | 1.132e+00 | 0 | 6400 |

accuracy for noise levels up to 3%, whereas competing methods exhibit either large errors or numerical instability. At higher noise levels (4–5%), increased deviations are observed, reflecting amplified imbalance in the bilinear interaction terms; nevertheless, the identified dynamics remain stable, without numerical blow-up or collapse to trivial solutions.

### 6.3.9 Glycolytic oscillator

Oscillatory glycolysis is a canonical biochemical process in yeast, responsible for maintaining energy balance through periodic variations of key metabolites such as ADP and F6P. This phenomenon serves as a paradigmatic example of biochemical feedback and collective synchronization in living cells. While yeast glycolytic oscillations evolve on a rapid tens-of-seconds timescale [29], routine experimental assays frequently suffer from low temporal resolution, often sampling only every 5 seconds or even every minute [30, 31]. Consequently, the collected data are temporally sparse relative to the intrinsic dynamics, posing a significant challenge for modeling.

We use the ODEBench system "Glycolytic oscillator, e.g., ADP and F6P in yeast (dimensionless)" (system id = 39), whose dynamics are expressed as

$$\dot{x}_1 = -x_1 + a\,x_2 + x_1^2 x_2,$$
$$\dot{x}_2 = b - a\,x_1 - x_1^2 x_2,$$

where $x_1(t)$ and $x_2(t)$ denote the dimensionless concentrations of ADP (substrate) and F6P (intermediate metabolite), respectively, representing the energy and glycolytic components of the system. The parameters $a$ and $b$ represent the kinetic coupling strength and the external substrate influx rate:

- $a$: enzyme coupling strength (*coupling strength*) — describes the catalytic rate between substrate and product;
- $b$: external substrate influx rate (*external substrate influx rate*) — controls the continuous supply of substrate into the system.

Precise estimation of these parameters is critical for characterizing oscillation stability and elucidating mechanisms of metabolic regulation. The true parameters are $a = 2.4$ and $b = 0.07$, and the initial conditions are $(x_1, x_2) = (0.4, 0.31)$ and $(0.2, -0.7)$, as specified in ODEBench.

#### Data generation and noise modeling

Numerical integration is performed over $t \in [0, 10]$ s with 201 uniformly spaced samples using the LSODA solver, yielding a base sampling interval

$$\Delta t = \frac{10 - 0}{200} = 0.05 \text{ s}.$$

This configuration follows the official ODEBench implementation (https://github.com/GPBench/ODEBench)[26]. To evaluate robustness, zero-mean multiplicative Gaussian noise is applied:

$$\tilde{x}(t_i) = x(t_i)\big(1 + \sigma\xi_i\big), \qquad \xi_i \sim \mathcal{N}(0, 1),$$

where $\sigma \in \{0, 0.01, 0.02, 0.03, 0.04, 0.05\}$ corresponds to noise levels of 0%, 1%, 2%, 3%, 4%, and 5%. Downsampling by a factor of 6 is then applied to all noisy trajectories, leading to an effective sampling interval $T_s = 6\Delta t = 0.3$ s.

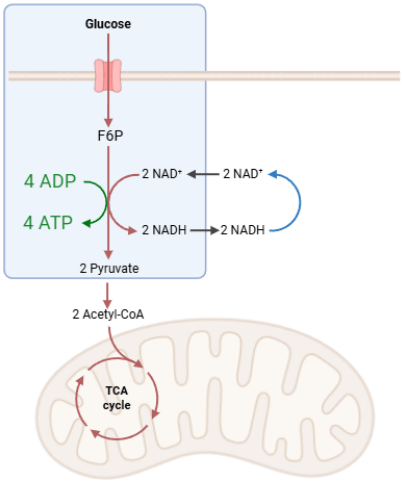


**Fig. 30**: Schematic of the glycolytic oscillator. Glucose enters the cell and is phosphorylated to fructose-6-phosphate (F6P). Through a series of enzyme-mediated reactions, adenosine diphosphate (ADP) is converted to adenosine triphosphate (ATP), shown in green. Two molecules of $NAD^+$ are reduced to NADH, which in turn participate in redox balance cycles (blue arrows). The resulting pyruvate is further oxidized to acetyl-CoA and enters the tricarboxylic acid (TCA) cycle in the mitochondria. This feedback between energy generation and consumption gives rise to oscillatory behavior in the coupled variables $x_1$ (ADP) and $x_2$ (F6P).

### Identified equations under noise (with error quantification)

Using HANDI, the following models were identified at noise levels $\sigma = 0\%, 1\%, 2\%, 3\%, 4\%, 5\%$:

$$(0\%) \quad \begin{cases} \dot{x}_1 = & 2.3999x_2 - 1.0010x_1 + 0.98595x_1^2x_2 + 0.02574x_1x_2^2 + 0.00334x_2^3 \\ & +0.00241x_1x_2 + 0.00238x_1^2 + 0.00120x_1^3 - 0.00011x_2^2 - 4.58 \times 10^{-5}, \\ \dot{x}_2 = & -2.3995x_1 - 0.98310x_1^2x_2 + 0.07003 - 0.01459x_1x_2^2 - 0.00597x_2^3 \\ & -0.00293x_1^3 - 0.00278x_1x_2 - 0.00178x_1^2 + 0.00030x_2^2 - 0.00022x_2, \end{cases}$$

$$(1\%) \quad \begin{cases} \dot{x}_1 = & 2.4227x_2 - 0.99516x_1 + 0.67733x_1^2x_2 - 0.13026x_2^3 - 0.10139x_1x_2 \\ & +0.04124x_1x_2^2 + 0.03000x_2^2 - 0.02953x_1^2 - 0.02131x_1^3 - 0.00083, \\ \dot{x}_2 = & -2.3788x_1 - 0.68332x_1^2x_2 - 0.46633x_1x_2^2 - 0.11652x_1^3 - 0.08238x_2^3 \\ & +0.06899 - 0.04308x_2^2 + 0.00760x_1^2 + 0.00668x_1x_2 - 0.00024x_2, \end{cases}$$

(2%)
$$\begin{cases} \dot{x}_1 = -2.99141\,x_1x_2^2 + 2.39037\,x_2 + 2.24786\,x_1^2x_2 - 0.951787\,x_1 \\ \quad +0.383908\,x_2^3 + 0.363984\,x_1^3 - 0.298853\,x_2^2 + 0.204974\,x_1x_2 \\ \quad +0.0386969\,x_1^2 + 0.00727977, \\ \dot{x}_2 = -2.33981\,x_1 - 1.87282\,x_1x_2^2 + 0.318012\,x_1^2x_2 + 0.218726\,x_1x_2 \\ \quad -0.184219\,x_1^3 - 0.1785\,x_2^2 + 0.16416\,x_2^3 + 0.0715465 \\ \quad -0.0303769\,x_2 + 0.0173604\,x_1^2, \end{cases}$$

(3%)
$$\begin{cases} \dot{x}_1 = 2.4955\,x_2 - 1.1746\,x_1x_2^2 - 0.916263\,x_1 - 0.601348\,x_1x_2 \\ \quad -0.440474\,x_1^2x_2 - 0.4362\,x_1^3 - 0.355517\,x_2^3 \\ \quad -0.249128\,x_1^2 - 0.0787953\,x_2^2 + 0.00492925, \\ \dot{x}_2 = -2.30135\,x_1 - 2.02517\,x_1x_2^2 - 0.548182\,x_1^3 - 0.365093\,x_1^2x_2 \\ \quad -0.215837\,x_2^2 - 0.189888\,x_2^3 - 0.127563\,x_1x_2 + 0.070751 \\ \quad -0.0645834\,x_1^2 + 0.0112772\,x_2, \end{cases}$$

(4%)
$$\begin{cases} \dot{x}_1 = 2.51022\,x_2 - 0.937292\,x_1 - 0.626442\,x_1x_2 - 0.61524\,x_1^2x_2 \\ \quad -0.593086\,x_1x_2^2 - 0.525371\,x_2^3 - 0.33799\,x_1^3 \\ \quad -0.216788\,x_1^2 + 0.0150633\,x_2^2 + 0.000760634, \\ \dot{x}_2 = -2.51195\,x_1x_2^2 - 2.27744\,x_1 - 0.690968\,x_1^3 - 0.268885\,x_2^3 \\ \quad -0.267745\,x_2^2 - 0.144792\,x_1x_2 - 0.0986881\,x_1^2x_2 + 0.0697583 \\ \quad -0.0656378\,x_1^2 + 0.0114746\,x_2, \end{cases}$$

(5%)
$$\begin{cases} \dot{x}_1 = \quad 2.5248x_2 - 0.93914x_1 - 0.72996x_1^2x_2 - 0.67587x_1x_2 - 0.62630x_2^3 \\ \quad\quad -0.51935x_1x_2^2 - 0.31535x_1^3 - 0.22124x_1^2 + 0.05098x_2^2 - 0.00101, \\ \dot{x}_2 = \quad -2.2710x_1 - 2.7233x_1x_2^2 - 0.73316x_1^3 + 0.36067x_1^2x_2 - 0.32470x_2^3 \\ \quad\quad -0.28181x_2^2 + 0.06718 - 0.06636x_1x_2 - 0.02693x_1^2 + 0.00095x_2. \end{cases}$$

The leading coefficients of $x_2$ in $\dot{x}_1$ and of $x_1$ in $\dot{x}_2$ correspond to $\pm a$, while the constant term in $\dot{x}_2$ gives $b$. To mitigate asymmetric estimation due to noise, the coupling parameter is averaged as

$$\hat{a} = \tfrac{1}{2}\big(|\mathrm{coeff}_{x_2}(\dot{x}_1)| + |\mathrm{coeff}_{x_1}(\dot{x}_2)|\big), \qquad \hat{b} = \mathrm{coeff}_1(\dot{x}_2).$$

Supplementary Table 28 summarizes the recovered parameters and their relative errors.

## Trajectory comparison and validation

***(a) Real trajectories (six noise configurations).***

Supplementary Fig. 31 shows the real trajectories of $x_1$ (ADP, blue) and $x_2$ (F6P, orange) for six noise levels (0–5%). Square markers denote 6× downsampled points.

**Table 28**: Recovered kinetic parameters under six noise levels ($a = 2.4$, $b = 0.07$).

| Noise | $a_{x_2}$ | $a_{x_1}$ | $\hat{a}$ | $\hat{b}$ | $\varepsilon_a$ (%) | $\varepsilon_b$ (%) |
|---|---|---|---|---|---|---|
| 0% | 2.3999 | 2.3995 | 2.3997 | 0.07003 | 0.01 | 0.04 |
| 1% | 2.4227 | 2.3788 | 2.4008 | 0.06899 | 0.03 | 1.44 |
| 2% | 2.3904 | 2.3398 | 2.3651 | 0.07155 | 1.45 | 2.21 |
| 3% | 2.4955 | 2.3014 | 2.3984 | 0.07075 | 0.07 | 1.07 |
| 4% | 2.5102 | 2.2774 | 2.3938 | 0.06976 | 0.26 | 0.35 |
| 5% | 2.5248 | 2.2710 | 2.3979 | 0.06718 | 0.09 | 4.03 |

***(b) Real vs. predicted trajectories (six noise configurations).***

Supplementary Fig. 32 compares the identified–model predictions (colored) with noisy observations (gray). Across all noise levels, the predicted oscillatory dynamics and amplitudes closely match the training trajectories.

***(c) Cross-method vector-field comparison.***

We further compare the recovered vector fields of seven identification methods for the id39-like glycolytic oscillator system. Supplementary Fig. 33 shows the true vector field together with the recovered fields by HANDI, EDMD, gEDMD, PSE, SINDy, SR3, and WSINDy, all evaluated over the same phase-space region and from identical initial conditions.

HANDI, SR3, and WSINDy accurately reproduce the global spiral structure and preserve the stable limit cycle, and their predicted trajectories closely overlap with the true periodic orbit. In contrast, gEDMD produces a severely distorted vector field that destroys the closed orbit and yields an incorrect spiral geometry. EDMD significantly deforms the direction of trajectories and vector fields. Although PSE and SINDy approximate the training trajectories with low error, they fail to recover the intrinsic structure of the underlying vector fields, leading to topological distortions in the reconstructed phase space.

## Physical parameter recovery

In this glycolytic oscillator, the parameters $a$ and $b$ play distinct physical roles: $a$ represents the enzyme coupling strength governing the nonlinear catalytic feedback between substrate (ADP) and product (F6P), while $b$ denotes the external substrate influx rate that sustains oscillatory dynamics. Both parameters are therefore of direct biochemical significance. The recovered parameters under noise-free observations are summarized in Supplementary Table 29.

To further assess robustness under noisy observations, trajectory-level accuracy is evaluated using the mean squared error (MSE). Supplementary Tables 30, 31 report the MSE of two representative glycolytic oscillator trajectories and error of identified vector fields for noise levels ranging from 1% to 5%. Consistent with the noise-free parameter recovery results, HANDI consistently achieves the lowest MSE across all noise regimes, with errors remaining several orders of magnitude smaller than those

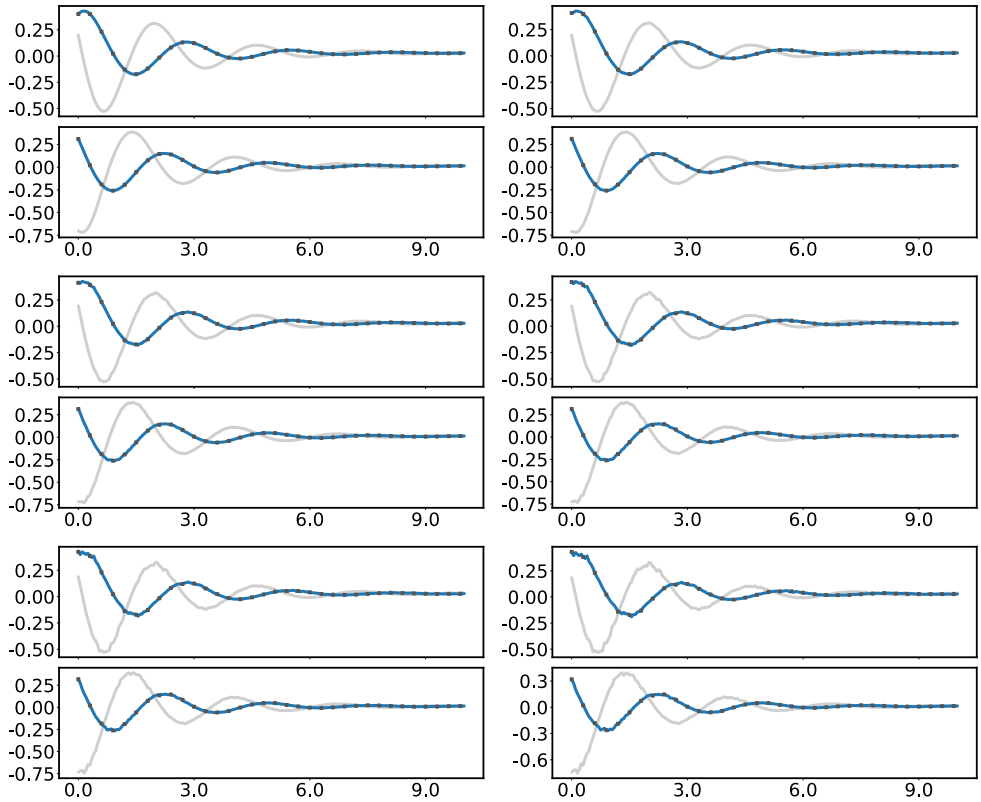

**Fig. 31**: True trajectories for the glycolytic oscillator under six noise levels (0–5%). Blue: $x_1$ (ADP); orange: $x_2$ (F6P). Square markers: 6× downsampled samples.

of competing methods. In contrast, PSE and Koopman-based approaches (EDMD, gEDMD) exhibit substantially larger errors or numerical instability.

### 6.3.10 Pendulum

The simple pendulum, one of the most fundamental nonlinear oscillators, captures the essence of dissipative periodic motion governed by gravitational restoring forces. A lightly damped pendulum obeys

$$\ddot{\theta} + \delta\dot{\theta} + \frac{g}{L}\sin\theta = 0, \tag{50}$$

where $\theta$, $\delta$, $g = 9.81\,\mathrm{m/s^2}$, and $L$ denote the angular displacement, viscous damping coefficient, gravitational constant, and wire length, respectively. Let $x_1 = \theta$ and $x_2 = \dot{\theta}$, the system becomes

$$\dot{x}_1 = x_2, \qquad \dot{x}_2 = -\delta x_2 - \frac{g}{L}\sin x_1. \tag{51}$$

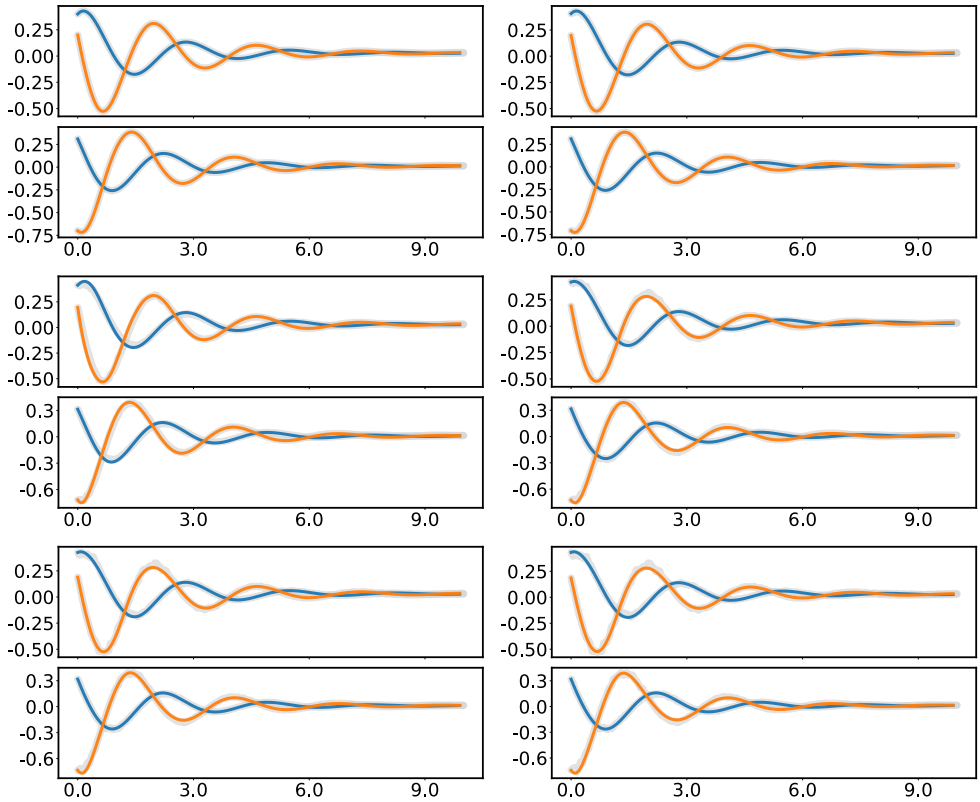


**Fig. 32**: Real (gray) vs. predicted (colored) trajectories under six noise levels (0–5%). The identified models reproduce the oscillatory coupling between $x_1$ (ADP) and $x_2$ (F6P) concentrations.

The hardware used here is a brass bob ($m = 44\,\mathrm{g}$) suspended from a steel wire of nominal length $L = 0.43\,\mathrm{m}$; the motion decays towards the stable equilibrium $(x_1, x_2) = (0, 0)$.

### Data and preprocessing

The raw data for the pendulum experiment is publicly available from the KU Leuven RDR data repository at https://doi.org/10.48804/SB7TNU. This data was generated from a video of a physical simple pendulum, consisting of a brass ball ($m = 44\,\mathrm{g}$) attached to a metal wire ($L = 0.43\,\mathrm{m}$). The dataset is provided as a `pickle` file containing bounding-box coordinates for each frame of the video, which was recorded at 120 fps and comprises approximately 18,000 frames[32]. The specific file is also accessible via the project's GitLab repository at https://gitlab.kuleven.be/gelenslab/publications/biological_oscillators_sindy/-/blob/main/data/all_boxes.dat.

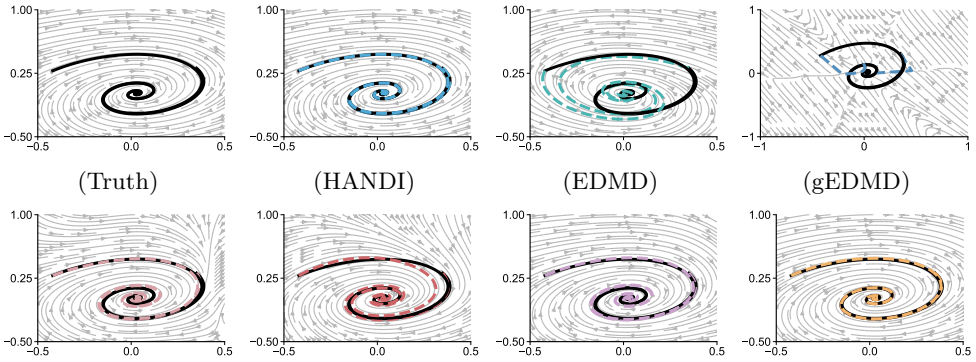


**Fig. 33**: Cross-method vector-field comparison for the id39-like glycolytic oscillator system. The first panel shows the true vector field, while the remaining seven panels show recovered vector fields by HANDI, EDMD, gEDMD, PSE, SINDy, SR3, and WSINDy. Black solid curves indicate true trajectories, and colored dashed curves denote predicted trajectories from identical initial conditions.

**Table 29**: Recovered glycolytic parameters $a$ (enzyme coupling strength) and $b$ (external substrate influx rate) under noise-free observations (true values: $a = 2.4$, $b = 0.07$).

| Methods | $\hat{a}$ | $\hat{b}$ | $\varepsilon_a$ (%) | $\varepsilon_b$ (%) |
|---|---|---|---|---|
| HANDI | 2.400e+00 | 7.003e-02 | 0.000e+00 | 5.000e-02 |
| SINDy | 2.272e+00 | 6.333e-02 | 5.350e+00 | 9.530e+00 |
| SR3 | 2.217e+00 | 6.421e-02 | 7.640e+00 | 8.270e+00 |
| WSINDy | 2.387e+00 | 7.003e-02 | 5.300e-01 | 4.000e-02 |
| PSE | 2.256e+00 | 6.498e-02 | 5.980e+00 | 7.170e+00 |
| EDMD | -2.402e+00 | 0.000e+00 | 2.001e+02 | 1.000e+02 |
| gEDMD | 2.402e+00 | 6.412e-02 | 8.000e-02 | 8.400e+00 |

The data pre-processing pipeline begins with a geometric transformation to establish a consistent coordinate system. We first define a static optical axis at $(x_{\text{mid}}, y_{\text{mid}}) = (227, 20)$ pixels. For each frame, the bob's center $(x, y)$ is calculated and converted into a Cartesian displacement $(\Delta x, \Delta y)$ from this axis. These displacements are then used to compute the swing angle via a polar coordinate conversion, $\theta(t) = \arctan\big(\Delta x / \Delta y\big)$. To focus on the primary oscillation dynamics, a temporal window is subsequently applied by retaining frames from $k = 140$ to $N - 130$, thereby discarding the initial manual release and final damping stages. Following this, the angular velocity $\dot{\theta}(t)$ is computed from the angle data using the centred finite-difference operator from PySINDy (`FiniteDifference(order=2)`), and the data is trimmed at the edges to ensure $\theta$ and $\dot{\theta}$ are time-aligned. Finally, the two processed

**Table 30**: Trajectory-level MSE of two representative glycolytic oscillator trajectories under different noise levels.

| Methods | 1% | | 2% | | 3% | |
|---|---|---|---|---|---|---|
| | Traj 1 | Traj 2 | Traj 1 | Traj 2 | Traj 1 | Traj 2 |
| HANDI | 7.460e-07 | 8.643e-06 | 4.400e-05 | 1.300e-04 | 3.300e-05 | 7.200e-05 |
| SINDy | 7.570e-04 | 1.883e-03 | 7.600e-04 | 1.467e-03 | 7.660e-04 | 1.590e-03 |
| SR3 | 1.079e-03 | 2.232e-03 | 9.450e-04 | 2.223e-03 | 8.220e-04 | 2.285e-03 |
| WSINDy | 1.800e-04 | 1.000e+03 | 5.850e-04 | 6.289e-02 | 3.710e-04 | 1.000e+03 |
| PSE | 1.217e-03 | 1.000e+03 | 1.123e-03 | 3.628e-03 | 1.042e-03 | 3.665e-03 |
| EDMD | 2.082e-02 | 3.493e-02 | 1.000e+03 | 1.000e+03 | 1.000e+03 | 1.000e+03 |
| gEDMD | 1.000e+03 | 1.000e+03 | 1.000e+03 | 1.000e+03 | 1.000e+03 | 1.000e+03 |

| Methods | 4% | | 5% | |
|---|---|---|---|---|
| | Traj 1 | Traj 2 | Traj 1 | Traj 2 |
| HANDI | 2.800e-05 | 1.060e-04 | 3.000e-05 | 1.470e-04 |
| SINDy | 7.780e-04 | 2.333e-03 | 7.810e-04 | 5.350e-03 |
| SR3 | 1.042e-03 | 2.551e-03 | 1.350e-03 | 2.573e-03 |
| WSINDy | 1.260e-03 | 1.000e+03 | 8.770e-04 | 5.135e-02 |
| PSE | 9.780e-04 | 2.333e-03 | 9.540e-04 | 6.278e-03 |
| EDMD | 1.146e+00 | 1.024e+00 | 2.451e-02 | 3.584e-02 |
| gEDMD | 1.000e+03 | 1.000e+03 | 1.000e+03 | 1.000e+03 |

**Table 31**: Error of identified vector fields averaged over state space.

| Method | $E_{L2}$ | $E_{\text{rel}}$ | $n_{\text{fail}}$ | $n_{\text{IC}}$ |
|---|---|---|---|---|
| HANDI | 4.371e-01 | 2.975e-01 | 0 | 6400 |
| SINDy | 1.314e+00 | 8.942e-01 | 0 | 6400 |
| SR3 | 3.585e-01 | 2.441e-01 | 0 | 6400 |
| PSE | 1.508e+02 | 1.027e+02 | 0 | 6400 |
| WSINDy | 6.904e+00 | 4.699e+00 | 0 | 6400 |
| EDMD | 9.619e+00 | 6.548e+00 | 0 | 6400 |
| gEDMD | 3.423e+03 | 2.330e+03 | 0 | 6400 |

state variables, the angle and its angular velocity $(\theta, \dot{\theta})$, are assembled into a two-column data matrix for subsequent identification.This results in a final data array with a shape of (1, 1304, 2), representing one trajectory of 1304 time steps with two state variables. The reconstructed trajectories after preprocessing are shown in Supplementary Fig. 35.

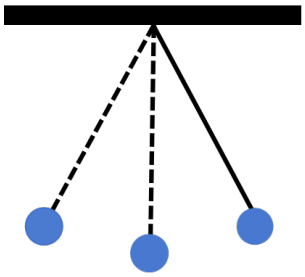

**Fig. 34**: Schematic of the simple pendulum system.

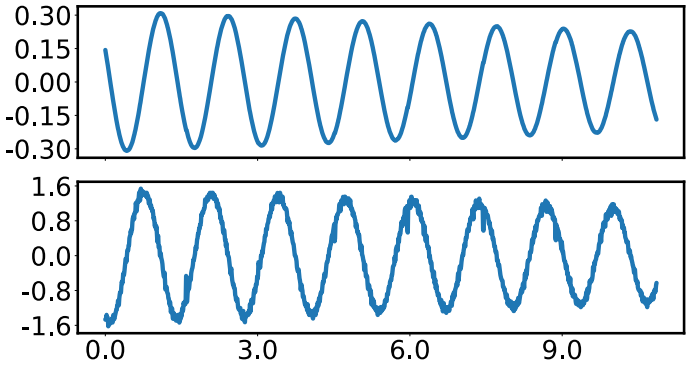


**Fig. 35**: Trajectories after preprocessing, including the measured angle and the numerically derived angular velocity.

### Identification of physical quantities

The identification is performed using the ground-truth trajectory generated over the interval $t \in [0, 12]\,\mathrm{s}$. To mimic realistic acquisition constraints, the high-resolution signal is downsampled, resulting in sampling periods of $T_s = 0.1, 0.2, 0.3\,\mathrm{s}$.

For example, using the sparsest sampling period $T_s = 0.3\,\mathrm{s}$, the model identified by HANDI is:

$$\dot{x}_1 = 0.9693\,x_2 + 0.1056\,x_1 - 0.00371\,x_1^2 - 0.0676\,x_1x_2 + 0.0151\,x_2^2, \tag{52}$$

$$\dot{x}_2 = -22.992\,x_1 - 0.147\,x_2 + 1.531\,x_1^2 + 0.2507\,x_1x_2 + 0.0136\,x_2^2. \tag{53}$$

The dominant stiffness term $-22.992\,x_1$ corresponds to $-g/L$. Taking the gravitational constant $g = 9.81\,\mathrm{m/s^2}$, the length is recovered as $L \approx \frac{9.81}{22.992} \simeq 0.427\,\mathrm{m}$, which is only 0.77% from the measured value of 0.430 m. The damping term yields the coefficient $\delta \approx 0.147\,\mathrm{s^{-1}}$; with the bob mass $m = 44\,\mathrm{g}$, the implied viscous parameter is $b = m\delta \simeq 6.5 \times 10^{-3}$.

The identified quantities under different sampling periods are provided in Supplementary Table 32. While most methods perform well at the finest resolution

($T_s = 0.1\,\mathrm{s}$), their accuracy degrades significantly as the sampling becomes sparser. In contrast, HANDI maintains a calibrated error below 1.5% even at $T_s = 0.3\,\mathrm{s}$.

**Table 32**: Recovered length $L$ by different models (true values: $L = 0.43$ m).

| Method | 0.1 s | | 0.2 s | | 0.3 s | |
|---|---|---|---|---|---|---|
| | $\hat{L}$ | $\varepsilon_L$ (%) | $\hat{L}$ | $\varepsilon_L$ (%) | $\hat{L}$ | $\varepsilon_L$ (%) |
| HANDI | 0.433 | 0.70 | 0.435 | 1.16 | 0.427 | 0.70 |
| SINDy | 0.451 | 4.88 | 0.515 | 19.77 | 0.620 | 44.19 |
| SR3 | 0.451 | 4.88 | 0.515 | 19.77 | 0.620 | 44.19 |
| WSINDy | 0.435 | 1.16 | 0.408 | 5.12 | 0.350 | 18.60 |
| PSE | 0.446 | 3.72 | 0.491 | 14.19 | 0.577 | 34.19 |
| EDMD | 0.575 | 33.72 | 0.535 | 24.42 | 0.450 | 4.65 |
| gEDMD | 0.459 | 6.74 | 0.508 | 18.14 | 0.634 | 47.44 |

### 6.3.11 Inverted flag

Fluid–structure interaction systems exhibit strong nonlinear coupling between flow-induced forces and elastic response, often producing self-sustained oscillations. The inverted flag is a canonical example of such dynamics and poses a severe identification challenge that the flow–structure feedback induces an unstable equilibrium and a nonlinear route to periodic flapping.

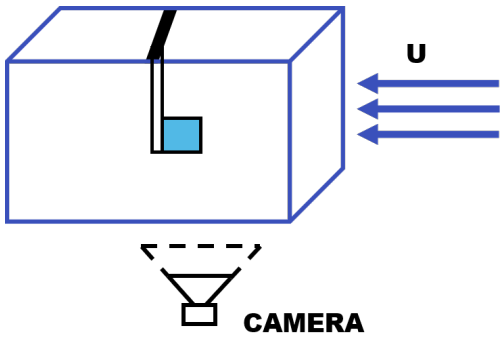


**Fig. 36**: Schematic illustration of the inverted flag experiment.

### Data and preprocessing

The raw time series for the inverted-flag experiment are publicly available at https://drive.google.com/drive/folders/16IGMR4v87ZZsTmEtgscQVjuxoeOny1Rd. Each file

records the two–dimensional position of the flag's tip at 30 Hz; the state variable $x(t)$ is the in-plane stream-wise displacement from the clamped leading edge (positive downstream), while $y(t)$ is the transverse deflection normal to the mean flow (positive to the flag's right)[33]. To create a dimensionless representation, these coordinates are normalized by the video's frame width and are thus expressed as a percentage.

**Pre-processing.** To reduce the influence of start-up noise, the initial portion of each record is discarded and the remaining data are then truncated to a common length for analysis (see the accompanying code for the trajectory-specific cropping). Let $t_n = n\Delta t$ with $\Delta t = 1/30$ s denote the sampling times. The in-plane velocities are approximated by first-order differencing,

$$\dot{x}(t_n) \approx \frac{x(t_{n+1}) - x(t_n)}{\Delta t}, \qquad \dot{y}(t_n) \approx \frac{y(t_{n+1}) - y(t_n)}{\Delta t}. \tag{54}$$

We then define the four-component state at time $t_n$ as

$$\mathbf{x}(t_n) = [x(t_n),\, \dot{x}(t_n),\, y(t_n),\, \dot{y}(t_n)]^\top = [x_1(t_n),\, x_2(t_n),\, x_3(t_n),\, x_4(t_n)]^\top, \tag{55}$$

where $x_1$ is the stream-wise position, $x_2$ the stream-wise velocity, $x_3$ the transverse position, and $x_4$ the transverse velocity.

All traces are then truncated to the common minimum length $T_{\min} = 454$ samples (about 15.1 s), yielding a dataset containing six independent trajectories. The processed dataset is provided in `HANDI_codes/Real-world examples/Inverted_Flag/data/trajectories.npy`. The first four trajectories in this file are used for training, and the last two trajectories are used for testing since their initial conditions are distinct from the training set. The training set trajectories are shown in Supplementary Fig. 37.

## Identified model

We now focus on the model identified from data with $T_s = 0.2\,\mathrm{s}$ for further physical validation. HANDI identifies a four-dimensional polynomial model governing the flag's tip dynamics. Terms in each equation list the *linear* part first (underbraced), followed by higher-order polynomial terms.

$$\begin{aligned}
\dot{x}_1 = \underbrace{-0.00752744\,x_1 + 0.992015\,x_2 - 0.903634\,x_3 - 0.0322842\,x_4}_{\text{Linear terms}} \\
&+ 6.86519\,x_2\,x_3^2 - 5.64562\,x_3^3 + 4.61439\,x_3^2 + 4.46766\,x_2\,x_3\,x_4 - 2.47902\,x_1\,x_3\,x_4 \\
&- 1.99663\,x_1\,x_4^2 + 1.77748\,x_3^2 x_4 - 1.65949\,x_3\,x_4^2 + 0.883076\,x_4^2 - 0.878867\,x_3\,x_4 \\
&- 0.710215\,x_1^2 x_3 - 0.673796\,x_1\,x_2\,x_4 - 0.596174\,x_1\,x_3^2 + 0.463547\,x_2^2 x_3 + 0.327969\,x_1\,x_3 \\
&- 0.21006\,x_1\,x_4 + 0.208929\,x_1^2 + 0.201085\,x_1\,x_2\,x_3 + 0.196959\,x_4^3 - 0.193543\,x_2\,x_3 \\
&+ 0.190015\,x_1^2 x_2 - 0.114432\,x_2\,x_4 + 0.106199\,x_1^2 x_4 + 0.0921677\,x_1\,x_2^2 \\
&- 0.0414337\,x_2\,x_4^2 + 0.0122929\,x_2^2 x_4 - 0.00914444\,x_1^3 + 0.00737129\,x_2^3
\end{aligned}$$

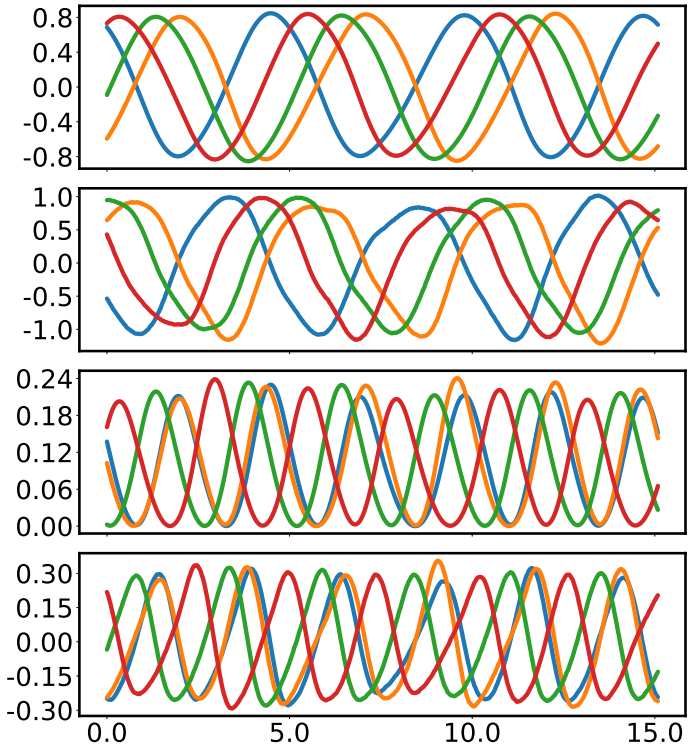


**Fig. 37**: Time series of the pre-processed state of the flag tip $(x_1(t), x_2(t), x_3(t), x_4(t))$ for the inverted flag (training set).

$$+ 0.00353617\, x_1\, x_2 + 0.00300473\, x_2^2, \tag{56}$$

$$\begin{aligned}\dot{x}_2 = &\underbrace{0.907705\, x_1 + 0.239115\, x_2 + 17.7833\, x_3 + 2.29389\, x_4}_{\text{Linear terms}} \\ &- 173.594\, x_2\, x_3\, x_4 + 167.676\, x_3^3 - 152.127\, x_2\, x_3^2 - 104.009\, x_3^2 + 75.4016\, x_1\, x_4^2 \\ &+ 62.7127\, x_1\, x_3\, x_4 + 36.0971\, x_1\, x_3^2 + 32.295\, x_3\, x_4^2 - 25.473\, x_3^2 x_4 - 19.1053\, x_1\, x_3 \\ &+ 17.7833\, x_3 + 11.3694\, x_1\, x_2\, x_3 + 8.63541\, x_1^2 x_3 - 8.10651\, x_4^2 + 7.48842\, x_2\, x_4 \\ &- 6.15303\, x_1\, x_2^2 + 3.80906\, x_2\, x_4^2 - 3.54091\, x_4^3 - 3.17973\, x_1^2 x_4 - 3.12432\, x_3\, x_4 \\ &- 2.83036\, x_1^2 + 2.29389\, x_4 - 2.01934\, x_1^2 x_2 + 1.49499\, x_1\, x_2\, x_4 - 0.971225\, x_1\, x_2 \\ &+ 0.907705\, x_1 + 0.693216\, x_1\, x_4 + 0.603866\, x_2^2 x_3 + 0.351687\, x_2\, x_3 - 0.273776\, x_2^2 x_4 \\ &- 0.27162\, x_1^3 + 0.239115\, x_2 - 0.208526\, x_2^3 - 0.105469\, x_2^2,\end{aligned} \tag{57}$$

$$\begin{aligned}\dot{x}_3 = &\underbrace{-0.000141693\, x_1 + 0.00168058\, x_2 + 1.02736\, x_3 + 1.0413\, x_4}_{\text{Linear terms}} \\ &- 4.64753\, x_3^2 + 2.54582\, x_3^3 - 1.83829\, x_2\, x_3^2 + 1.42121\, x_3^2 x_4 + 1.20053\, x_1^2 x_3\end{aligned}$$

$$
\begin{aligned}
&- 1.13898\,x_4^2 + 1.05132\,x_1\,x_2\,x_4 + 1.0413\,x_4 + 1.02736\,x_3 + 0.937005\,x_1\,x_3\,x_4 \\
&+ 0.922724\,x_3\,x_4^2 + 0.916909\,x_1\,x_2\,x_3 - 0.842514\,x_2^2 x_3 - 0.773424\,x_3\,x_4 - 0.418096\,x_2\,x_3\,x_4 \\
&- 0.283055\,x_1^2 - 0.243364\,x_1^2 x_4 + 0.158739\,x_1\,x_4^2 + 0.150652\,x_4^3 - 0.0841357\,x_1\,x_4 \\
&- 0.0646655\,x_1\,x_3 + 0.0635833\,x_2\,x_4^2 + 0.0602009\,x_2\,x_3 - 0.0221983\,x_1\,x_2 \\
&+ 0.0200565\,x_1^3 + 0.0200399\,x_2\,x_4 + 0.0128184\,x_1^2 x_2 - 0.00991188\,x_1\,x_2^2 \\
&- 0.00914333\,x_2^2 x_4 - 0.00884189\,x_2^2 - 0.00701034\,x_1\,x_3^2 - 0.00199487\,x_2^3 \\
&+ 0.00168058\,x_2 - 0.000141693\,x_1, \qquad (58)
\end{aligned}
$$

$$
\begin{aligned}
\dot{x}_4 = &\underbrace{0.0300019\,x_1 - 0.0315982\,x_2 - 14.7475\,x_3 + 0.294645\,x_4}_{\text{Linear terms}} \\
&- 40.2828\,x_3\,x_4^2 + 39.9678\,x_3^2 + 35.5272\,x_3^2 x_4 + 32.1278\,x_4^2 + 23.0252\,x_3^3 \\
&- 19.1883\,x_3\,x_4 - 18.8511\,x_1^2 x_3 - 17.1739\,x_1\,x_2\,x_4 - 14.7475\,x_3 + 10.8883\,x_2\,x_3^2 \\
&- 9.67553\,x_1\,x_3\,x_4 + 7.59197\,x_2\,x_3\,x_4 + 4.43912\,x_1^2 + 2.62\,x_1\,x_2\,x_3 + 2.50968\,x_1\,x_3 \\
&- 2.42615\,x_1\,x_4^2 + 2.076\,x_1\,x_4 - 1.43327\,x_2\,x_4^2 + 1.41171\,x_1^2 x_4 - 1.34478\,x_1\,x_3^2 \\
&- 1.11005\,x_2^2 x_3 - 0.744693\,x_1^3 + 0.536386\,x_2^2 - 0.467116\,x_1^2 x_2 - 0.39948\,x_2\,x_3 \\
&- 0.378946\,x_2^2 x_4 + 0.294645\,x_4 - 0.292221\,x_2\,x_4 + 0.237409\,x_4^3 + 0.0893352\,x_1\,x_2 \\
&+ 0.0725666\,x_1\,x_2^2 - 0.0315982\,x_2 + 0.0300019\,x_1 + 0.0283755\,x_2^3. \qquad (59)
\end{aligned}
$$

### Amplitude recovery analysis

We further examine the ability of identified models to recover the flapping amplitude of the inverted flag. The amplitude is computed from $x_1(t)$: for each oscillation period $j$ of $x_1(t)$, we detect a local maximum $x_{1,\max}^{(j)}$ and the subsequent local minimum $x_{1,\min}^{(j)}$, and compute the cycle amplitude as

$$
A^{(j)} = x_{1,\max}^{(j)} - x_{1,\min}^{(j)}. \qquad (60)
$$

The reported amplitude is then obtained by averaging over all detected cycles,

$$
A = \frac{1}{N_c} \sum_{j=1}^{N_c} A^{(j)}, \qquad (61)
$$

where $N_c$ is the number of oscillation cycles within the analyzed time window. For each method, $\hat{A}$ denotes the recovered amplitude obtained using the above procedure. The relative error is computed as

$$
\varepsilon_A = \frac{|\hat{A} - A_{\text{true}}|}{A_{\text{true}}} \times 100\%. \qquad (62)
$$

The reference amplitude $A_{\text{true}} \approx 1.642$ is obtained by averaging the cycle-averaged amplitudes computed from the four training trajectories (Trajectories 1–4). To assess

robustness under sparse sampling, we evaluate amplitude recovery across three different sampling intervals: $T_s = 0.1$, 0.1666, and 0.2 s (Supplementary Table 33). Each method is tested on four trajectories, and the reported values $\hat{A}$ and $\varepsilon_A$ are computed from the across-trajectory averages. The "–" entry indicates that the method failed to converge on all four trajectories at the corresponding sampling interval.

**Table 33**: Recovered amplitude $A$ by different models for the inverted flag system (true amplitude $A_{\text{true}} \approx 1.642$).

| Method | 0.1 s | | 0.1666 s | | 0.2 s | |
|---|---|---|---|---|---|---|
| | $\hat{A}$ | $\varepsilon_A$ (%) | $\hat{A}$ | $\varepsilon_A$ (%) | $\hat{A}$ | $\varepsilon_A$ (%) |
| HANDI | 1.640 | 0.12 | 1.647 | 0.30 | 1.639 | 0.18 |
| SINDy | 1.622 | 1.22 | 1.572 | 4.26 | 1.663 | 1.28 |
| SR3 | 1.621 | 1.28 | – | – | 1.342 | 18.27 |
| WSINDy | 1.606 | 2.19 | 1.645 | 0.18 | – | – |
| PSE | 1.635 | 0.43 | 1.443 | 12.12 | – | – |
| EDMD | – | – | – | – | – | – |
| gEDMD | – | – | – | – | – | – |

The results demonstrate that HANDI consistently achieves the lowest amplitude error across all sampling intervals, with errors below 0.3%. In contrast, other methods exhibit increasing errors or divergence as the sampling becomes sparser. Notably, EDMD and gEDMD fail to produce stable predictions for this high-dimensional nonlinear system, while SINDy-based methods show degraded performance at larger sampling intervals.

### Detailed analysis of energy-exchange asymmetry

Fluid–structure coupling in the inverted-flag system produces a strongly asymmetric exchange of kinetic energy between the two half-cycles of flapping motion. For a detailed physical validation, we focus on the HANDI model identified from sampling period $T_s = 0.2$ s. We quantify the energy-exchange asymmetry using the (mass-normalized) kinetic energy (KE)

$$\mathrm{KE}(t) = \frac{1}{2} v(t)^2, \qquad v(t) = \sqrt{x_2(t)^2 + x_4(t)^2}, \tag{63}$$

where $v(t)$ is the tip speed. As discussed in the main text, the identified model faithfully reconstructs this asymmetry, which manifests as two distinct KE maxima during opposite-direction strokes.

Following the notation in the main text, we define two representative KE maxima:

- $P_a$ (Upstream stroke): the KE maximum during upstream motion ($x_2(t) < 0$), with corresponding speed $v_a$;

- $P_b$ (Downstream stroke): the KE maximum during downstream motion ($x_2(t) > 0$), with corresponding speed $v_b$.

Our analysis of $P_a$ and $P_b$ was applied to four training trajectories. A representative case (Trajectory 2) is visualized in Supplementary Fig. 38 and Fig. 39, showing that the model-predicted peaks ($P_a$, $P_b$) align closely with those from the ground truth in both phase-space and time-domain representations. Supplementary Table 34 summarizes the quantitative comparison across all trajectories. For each trajectory, we report the $x_1$-position and tip speed at the two KE peaks, together with the average Euclidean distance between the true and predicted peak coordinates. The identified model accurately reproduces $v_a > v_b$ for all cases, while maintaining a small average spatial error of 0.052. This observation that $v_a > v_b$ indicates that the upstream stroke is more energetically enhanced due to asymmetric vortex shedding and delayed flow separation.

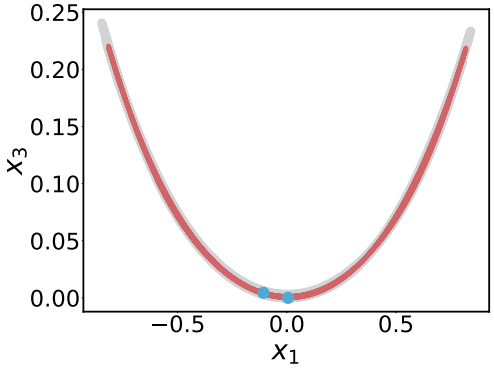


**Fig. 38**: Detailed analysis of Trajectory 2 (Phase Space). Tip trajectory ($x_3$ vs. $x_1$) showing the representative KE peaks $P_b$ (downstream) and $P_a$ (upstream) identified from the model's simulation (blue 'o').

### 6.3.12 Wheel shimmy

Wheel shimmy refers to a self-excited vibration of the front wheels under high-speed or specific operating conditions, characterized by nonlinear oscillations of the steering wheel about the vertical axis. This phenomenon is commonly observed in aircraft nose gears, motorcycles, and automobiles, exhibiting typical nonlinear, strongly coupled, and even chaotic vibrational characteristics. In this section, we employ experimentally collected real-world wheel shimmy data for system identification and prediction performance validation, as illustrated schematically in Supplementary Fig. 40[33].

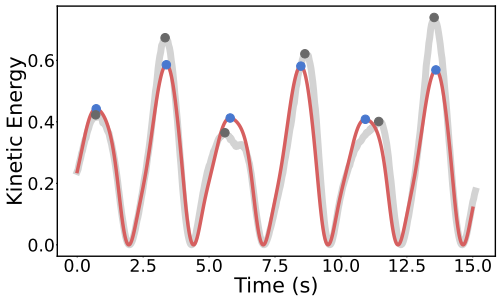


**Fig. 39**: Detailed analysis of Trajectory 2 (Time Domain). Kinetic energy vs. time. The model's predicted peaks (blue 'o') align closely with the true peaks (grey 'o'), capturing the two distinct KE maxima that characterize the asymmetric energy exchange.

**Table 34**: Quantitative comparison of representative kinetic-energy peaks ($P_a$: upstream, $P_b$: downstream) across all test trajectories. For each trajectory, the ground truth (True) and the model prediction (Model) are reported. The identified model accurately reproduces the asymmetric energy exchange, consistently yielding $v_a > v_b$.

| Traj. | Data | Upstream Peak ($P_a$) | | Downstream Peak ($P_b$) | | Avg. Peak Distance Error |
|---|---|---|---|---|---|---|
| | | $x$-pos | Speed ($v_a$) | $x$-pos | Speed ($v_b$) | |
| 1 | True | -0.125 | 1.073 | 0.083 | 0.840 | 0.046 |
| | Model | -0.105 | 1.077 | 0.013 | 0.912 | |
| 2 | True | -0.095 | 1.161 | -0.028 | 0.919 | 0.023 |
| | Model | -0.107 | 1.078 | 0.006 | 0.908 | |
| 3 | True | -0.019 | 1.059 | 0.079 | 0.987 | 0.098 |
| | Model | -0.116 | 1.060 | -0.020 | 0.905 | |
| 4 | True | -0.091 | 1.121 | -0.091 | 0.983 | 0.042 |
| | Model | -0.106 | 1.133 | -0.022 | 0.966 | |

## Data and preprocessing

The dataset contains signals of the front-wheel angle $\theta(t)$. The angular velocity $\dot{\theta}(t)$ is not directly measured but computed numerically from the angle signal using Savitzky–Golay differentiation. Both states (measured angle and derived angular velocity) are used for system identification. The raw sampling interval is $\Delta t = 0.005$ s. Two experimental trajectories are available, each covering $t \in [0, 3.075]$ s. The raw experimental data are publicly available at *Google Drive (Wheel Shimmy Dataset)*.

For identification, each state is standardized using a single affine transform computed across all samples of the training set (i.e., over all time steps of all trajectories). Specifically, the standardized state $\mathbf{z} \in \mathbb{R}^2$ is defined component-wise as

$$z_i = \frac{x_i - \mu_i}{\sigma_i}, \qquad i = 1, 2,$$

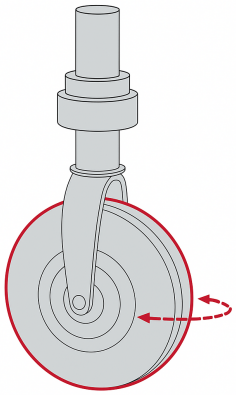

**Fig. 40**: Schematic illustration of the wheel shimmy phenomenon. The red dashed arrows indicate the self-excited oscillatory motion about the vertical axis.

where

$$\boldsymbol{\mu} = \begin{bmatrix} 0.0009544 \\ -0.0475395 \end{bmatrix}, \quad \boldsymbol{\sigma} = \begin{bmatrix} 0.0664808 \\ 0.9665666 \end{bmatrix}.$$

The first component corresponds to the angle and the second to the angular velocity. The same $(\boldsymbol{\mu}, \boldsymbol{\sigma})$ are applied to all samples for consistency, i.e., no per-trajectory normalization is used. All physical results reported in this section are obtained by the inverse transform,

$$x_i = z_i\,\sigma_i + \mu_i, \qquad i = 1, 2.$$

The reconstructed trajectories after preprocessing are shown in Supplementary Fig. 41.

### Identification of physical quantities

The identification is performed using two training trajectories. To evaluate robustness under sparse sampling, the raw data (at $\Delta t = 0.005\,\mathrm{s}$) is downsampled to effective sampling periods of $T_s = 0.08, 0.095, 0.11\,\mathrm{s}$.

For the wheel shimmy system, oscillatory characteristics are extracted directly from the time–domain numerical responses of the identified nonlinear ODE, without invoking linearization or eigenvalue analysis. Using sampling period $T_s = 0.11\,\mathrm{s}$, we define $\theta \equiv x_1$ (angle, rad) and $\omega \equiv x_2$ (angular velocity, rad/s). The identified continuous–time model is given by

$$\begin{aligned}\dot{x}_1 = {} & 14.4129\,x_2 + 0.0970819\,x_1 - 1.10396\,x_1x_2 - 0.706969\,x_2^2 - 0.274129\,x_1^2 \\ & + 0.511632\,x_1x_2^2 - 0.204207\,x_1^3 + 0.110337\,x_2^3 + 0.0234364\,x_1^4\end{aligned}$$

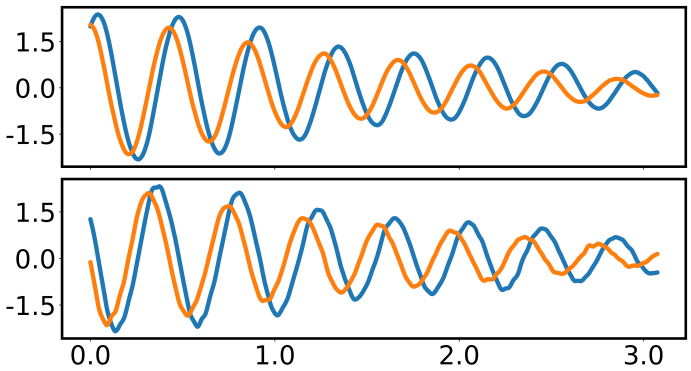


**Fig. 41**: Trajectories after preprocessing, including the measured angle and the numerically derived angular velocity.

$$+ 0.186406\, x_1^3 x_2 + 0.0996347\, x_1 x_2^3 + 0.111268\, x_2^4, \tag{64}$$

$$\begin{aligned}\dot{x}_2 = &-17.5155\, x_1 - 1.4151\, x_2 + 1.13042\, x_1 x_2 + 1.03413\, x_1^2 - 1.42427\, x_2^2 \\ &+ 0.662696\, x_1^3 + 0.98089\, x_1 x_2^2 - 0.417805\, x_1^2 x_2 + 0.412774\, x_2^3 \\ &- 0.409313\, x_1^4 - 0.461067\, x_1^3 x_2 + 0.33917\, x_2^4.\end{aligned} \tag{65}$$

The model is trained using standardized variables $z_i = (x_i - \mu_i)/\sigma_i$ with

$$\boldsymbol{\mu} = \begin{bmatrix} 0.0009544 \\ -0.0475395 \end{bmatrix}, \qquad \boldsymbol{\sigma} = \begin{bmatrix} 0.0664808 \\ 0.9665666 \end{bmatrix},$$

and all quantities reported below are de–standardized to physical units ($\theta$ [rad], $\omega$ [rad/s]).

Three trajectories are considered: two trajectories corresponding to the training data, and one additional trajectory initialized at a significantly larger amplitude. For each trajectory $\theta(t)$, a dominant oscillation frequency $f_d$ is first estimated using the fast Fourier transform (FFT). This frequency is used both to define an equivalent damped angular frequency

$$\omega_d = 2\pi f_d, \tag{66}$$

and to provide a reference scale for robust peak detection in the time domain.

From the extracted positive peak sequence $\{A_k\}$ of $\theta(t)$, the logarithmic decrement between successive peaks is computed as

$$\delta_k = \ln\left(\frac{A_k}{A_{k+1}}\right). \tag{67}$$

To reduce sensitivity to noise and occasional irregular peaks, the median value

$$\delta = \mathrm{median}_k(\delta_k) \tag{68}$$

is adopted as an equivalent logarithmic decrement for each trajectory.

Under the standard underdamped oscillator assumption, an equivalent damping ratio is defined by

$$\zeta = \frac{\delta}{\sqrt{4\pi^2 + \delta^2}}, \tag{69}$$

and the corresponding quality factor is approximated as

$$Q = \frac{\pi}{\delta}, \tag{70}$$

which is valid in the small–damping regime relevant to the present system.

Finally, an equivalent undamped natural frequency is inferred as

$$\omega_n = \frac{\omega_d}{\sqrt{1 - \zeta^2}}, \tag{71}$$

which characterizes the dominant oscillation time scale of the trajectory. For the two training trajectories, the extracted equivalent parameters are consistent, yielding

$$\omega_d \approx 15.5 \text{ rad/s}, \qquad \zeta \approx 4 \times 10^{-2}, \qquad Q \approx 10\text{–}15,$$

indicating a weakly damped oscillatory response that is well captured by the identified nonlinear model in the training regime.

For the large–amplitude trajectory, the equivalent parameters change markedly: the dominant oscillation frequency decreases to

$$\omega_d \approx 13.5 \text{ rad/s},$$

while the equivalent damping ratio becomes extremely small,

$$\zeta \approx 7 \times 10^{-4},$$

corresponding to very slow decay of the oscillation envelope. Despite this strong amplitude dependence, the trajectory remains asymptotically convergent to the origin, highlighting the stabilizing nonlinear structure learned by the model.

Supplementary Table 35 summarizes the recovered natural frequency for each method across different sampling intervals. The "–" entry indicates that the method diverged or failed to identify a stable model.

### 6.3.13 Neuronal integration

Electrical activity underlies all neuronal computation. Discovering interpretable models from membrane potential recordings is essential for understanding neural coding, disease mechanisms, and pharmacological modulation. Here we consider the neuronal integration system. Using the whole-cell patch-clamp technique, multiple stimulus–response experiments (sweeps) are conducted on mouse cortical neurons, as illustrated in the Supplementary Fig. 44. These experiments simultaneously capture the injected

**Table 35**: Recovered natural frequency $\omega_n$ (rad/s) by different models for the wheel shimmy system.

| Method | 0.08 s | | 0.095 s | | 0.11 s | |
|---|---|---|---|---|---|---|
| | $\hat{\omega}_n$ | $\varepsilon_{\omega_n}$ (%) | $\hat{\omega}_n$ | $\varepsilon_{\omega_n}$ (%) | $\hat{\omega}_n$ | $\varepsilon_{\omega_n}$ (%) |
| HANDI | 14.458 | 0.03 | 14.455 | 0.00 | 14.792 | 0.01 |
| PSE | 12.381 | 14.35 | 10.317 | 28.62 | – | – |
| SINDy | – | – | 10.318 | 28.62 | – | – |
| SR3 | 12.383 | 14.33 | 10.318 | 28.62 | 8.448 | 42.90 |
| WSINDy | – | – | – | – | – | – |
| EDMD | – | – | – | – | – | – |
| gEDMD | – | – | – | – | – | – |

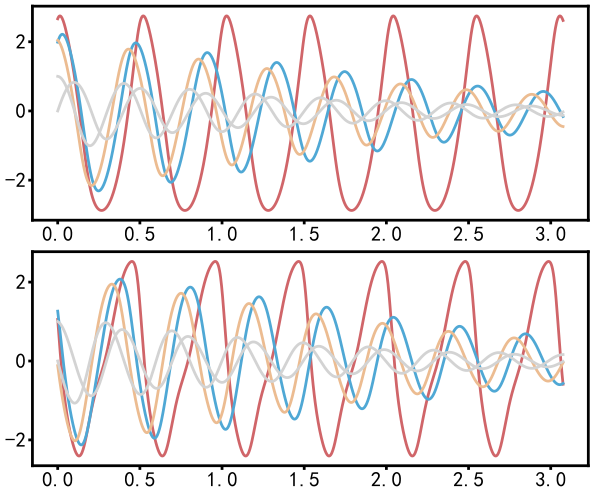


**Fig. 42**: Time series of the identified ODE. Top: $\theta(t)$; bottom: $\omega(t)$ for five initial conditions. The red curve corresponds to the largest-amplitude initial condition and shows slower decay and slightly lower frequency. The blue and orange curves use initial conditions matched to the two training trajectories. Remaining runs are plotted in light gray.

currents and the corresponding membrane potential variations, thereby yielding high-precision time-series data. Such electrophysiological data exhibit pronounced nonlinear and strongly coupled characteristics, providing a solid foundation for the construction and validation of neuronal dynamical models.

### Data and preprocessing

The raw electrophysiological data of biological neurons were obtained from the Allen Cell Types Database (https://allensdk.readthedocs.io/en/latest/index.html ) via the

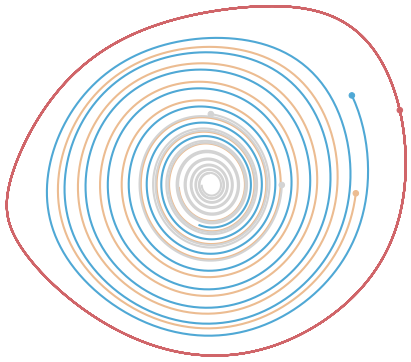

**Fig. 43**: Phase portrait. Trajectories in the $(x_1, x_2)$ plane spiral into the origin (stable focus). The outer red loop corresponds to the largest initial amplitude, illustrating the strongly nonlinear, weakly damped transient before convergence. The blue and orange trajectories start from initial states identical to the two training trials.

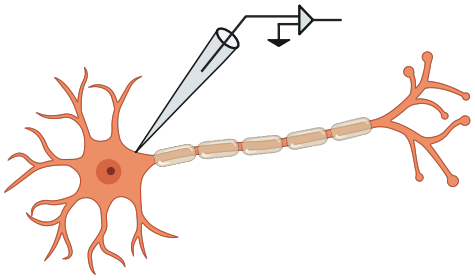

**Fig. 44**: Schematic of the neuronal integration system.

`CellTypesCache` API [34]. We select the sample with ID 324257146. Each record contains multiple scanning sequences, all labeled with corresponding stimulus types. This study screened out the experimental sequences involving constant current stimulation, with a data acquisition frequency of 200 kHz.

**Pre-processing.** The FitzHugh–Nagumo (FN) model provides a simplified two-dimensional representation of neuronal dynamics:

$$\dot{V}(t) = V(t) - \frac{V^3(t)}{3} - W(t) + I, \qquad \dot{W}(t) = a\,(V(t) + b - cW(t))\,,$$

where $V(t)$ denotes the membrane potential, $W(t)$ is the recovery variable, and $I$ represents the external constant input current. The membrane potential $V(t)$ was first smoothed using a Savitzky–Golay filter to reduce noise, and its derivative $\dot{V}(t)$ was

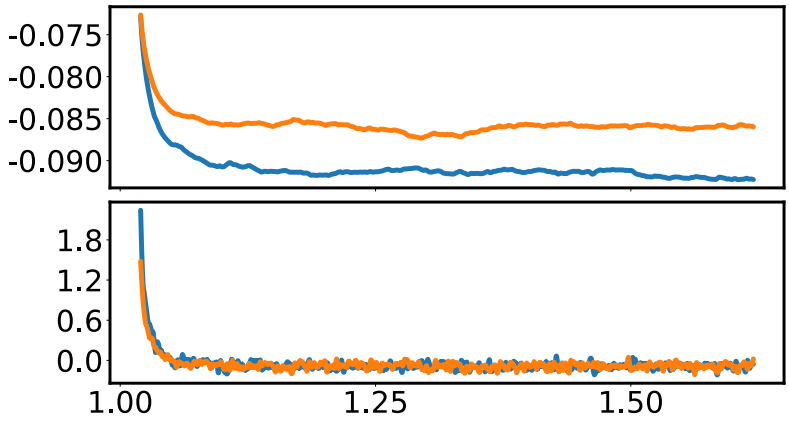


**Fig. 45**: Trajectories after preprocessing, including the membrane potential $V$ and the recovery variable $W$.

computed. The recovery variable $W(t)$ was then reconstructed as

$$W(t) = V(t) - \frac{V^3(t)}{3} - \dot{V}(t) + I.$$

Both $V(t)$ and $W(t)$ were smoothed again to eliminate residual artifacts, as illustrated in Supplementary Fig. 45. The signals $V(t)$, $W(t)$, and $I$ were standardized to have zero mean and unit variance across all trials. The standardized data were then uniformly downsampled using three different sampling intervals, $T_s = 0.01, 0.02, 0.03s$. Within the interval $[1.02, 1.62]$ s (duration $= 0.60$ s), each trajectory yielded a sequence of sampled points determined by the corresponding sampling interval.

### Physical parameter recovery

The identification is performed using two trajectories driven by distinct input currents $I$. To evaluate robustness under sparse sampling, the downsampled data is further processed at effective sampling periods of $T_s = 0.01, 0.02, 0.03$ s.

For the neuronal integration system, the key physical quantity is the steady-state membrane potential $V_{ss}$, which characterizes the equilibrium response under constant current stimulation. From the identified model, $V_{ss}$ corresponds to the fixed point where $\dot{V} = 0$, and its value depends systematically on the applied current $I$.

For example, using sampling period $T_s = 0.03$ s, the model identified by HANDI is:

$$\begin{aligned}\dot{V}(t) = &-68.4668\,V(t) + 47.3012\,I + 19.597\,W(t) \\ &- 34.0075\,V(t)^2W(t) + 21.9788\,V(t)^3 + 20.8142\,V(t)W(t)^2 \\ &- 16.6151\,W(t)^2 - 3.45085\,V(t)^2 - 3.2005\,W(t)^3 + 0.11171\,V(t)W(t), \quad (72)\end{aligned}$$

$$\begin{aligned}\dot{W}(t) = &\ 605.494\,V(t) - 385.731\,I - 207.084\,W(t) \\ &- 201.909\,V(t)^3 + 109.543\,V(t)^2W(t) + 95.2014\,V(t)W(t)\end{aligned}$$

$$+ 38.643\,V(t)W(t)^2 - 32.1348\,W(t)^2 - 28.9836\,V(t)^2 - 24.7708\,W(t)^3. \quad (73)$$

Starting from the initial points of the original data, the system states rapidly converge to their steady values. The resulting steady-state potential for the two trajectories (with true values $-92.12\,\mathrm{mV}$ and $-85.95\,\mathrm{mV}$) is predicted with errors of only 0.25% and 0.08%, respectively. To summarize the steady-state performance, we report the average values of these trajectory errors in the main text.

Supplementary Table 36 summarizes the steady-state potential error for each method across different sampling intervals. For each sampling period, we report the errors for both trajectories ($\varepsilon_1$ and $\varepsilon_2$). The "–" entry indicates that the method diverged or produced physically unreasonable predictions.

**Table 36**: Steady-state potential error $\varepsilon_{V_{ss}}$ (%) by different models for the neuronal integration system.

| Method | 0.01 s | | 0.02 s | | 0.03 s | |
|---|---|---|---|---|---|---|
| | $\varepsilon_1$ | $\varepsilon_2$ | $\varepsilon_1$ | $\varepsilon_2$ | $\varepsilon_1$ | $\varepsilon_2$ |
| HANDI | 0.37 | 0.10 | 0.05 | 0.07 | 0.25 | 0.08 |
| SINDy | 6.09 | – | – | – | – | 0.22 |
| SR3 | – | – | – | 0.38 | 0.86 | – |
| PSE | 0.70 | 0.48 | 2.89 | 6.56 | – | 0.11 |
| WSINDy | 3.34 | 1.34 | 1.26 | 1.05 | 5.01 | 1.75 |
| gEDMD | 20.75 | 8.39 | – | – | – | – |
| EDMD | – | – | 3.10 | 27.29 | 10.97 | – |

# 7 Aliasing and the fundamental sampling limit of system identification

For a continuous-time nonlinear dynamical system $\dot{\mathbf{x}} = \mathbf{f}(\mathbf{x})$, the identification of the system is based on the data $\mathbf{x}(kT_s)$. When the sampling period $T_s$ is too large, different vector fields may generate the same discrete-time flow, leading to *system aliasing* [35, 36]. In this section, we introduce the *critical sampling period* $T_\gamma$ to avoid this aliasing.

## Definition of $T_\gamma$

The critical sampling period $T_\gamma$ is the largest sampling interval that guarantees the uniqueness of system identification. Equivalently, the sampling frequency must satisfy the condition [36]:

$$\omega > \omega_\gamma, \quad \omega_\gamma = 2\max|\mathrm{Im}(\sigma(L|_{\mathcal{F}_e^\gamma}))|, \quad (74)$$

which implies a maximum sampling period of:

$$T_\gamma = \frac{\pi}{\max |\mathrm{Im}(\sigma(L|_{\mathcal{F}_e^\gamma}))|}. \tag{75}$$

Here, $\sigma(\cdot)$ denotes the spectrum of the operator. The subspace $\mathcal{F}_e^\gamma$ is defined as the invariant function space that minimizes the largest oscillation frequency captured by the Koopman spectrum:

$$\mathcal{F}_e^\gamma \triangleq \arg\min_{\mathcal{F}_e} \max |\mathrm{Im}(\sigma(L|_{\mathcal{F}_e}))|. \tag{76}$$

In this context, $\mathcal{F}_e$ represents any invariant subspace where the Koopman operator and its infinitesimal generator $L$ are well-defined and bounded. By selecting $\mathcal{F}_e^\gamma$, we obtain the tightest possible sampling bound for the system.

## Physical explanation

The imaginary part of the Koopman spectrum corresponds to oscillatory components of observables $g(\mathbf{x}(t))$. Intuitively, $\max |\mathrm{Im}(\sigma(L|_{\mathcal{F}_e^\gamma}))|$ represents the highest oscillation frequency embedded in the system. Therefore, $T_\gamma$ ensures that the sampling is sufficiently fast to capture all intrinsic oscillations without ambiguity. If $T_s \geq T_\gamma$, multiple candidate systems may reproduce the same sampled trajectory, and reliable identification becomes impossible.

## Connection to Nyquist–Shannon Theorem

The role of $T_\gamma$ is analogous to the Nyquist frequency in classical signal processing: the sampling rate must exceed twice the maximum oscillation frequency characterized by Fourier spectrum. However, the classical Nyquist theorem is limited to band-limited linear systems. The Koopman framework extends this concept to nonlinear dynamics, where oscillatory modes are instead characterized by the Koopman operator spectrum. This spectral analysis offers a richer characterization: the real part of the Koopman eigenvalues describes the amplitude growth or decay, while the imaginary part defines the oscillation frequencies. This extension provides a principled definition of necessary sampling bounds for nonlinear systems, moving beyond the strict limitations of band-limited or linear requirements [37].

## Implications

Practically, $T_\gamma$ provides a criterion for experiment design and data collection: only when $T_s < T_\gamma$ can the underlying vector field $\mathbf{f}$ be uniquely recovered. Although computing $T_\gamma$ requires knowledge of the Koopman spectrum, data-driven approximations (e.g., DMD-based methods [38, 39]) allow it to be estimated from finely sampled trajectories, making the theory applicable to real-world nonlinear systems.

## Visualization of system aliasing

A continuous-time dynamical system possesses a fundamental sampling limit beyond which the underlying dynamics becomes non-identifiable. When the sampling period grows too large, aliasing inevitably occurs: different continuous-time trajectories collapse into indistinguishable discrete-time sampled sequences, making it theoretically impossible to uniquely recover the underlying continuous-time dynamics. Identifications under such extreme sampling regimes is therefore instructive for not only revealing the fundamental theoretical limit of continuous-time system identification but also conclusively demonstrating that our method maintains effectiveness right up to this theoretical boundary.

To explicitly illustrate this aliasing phenomenon, we revisit the fixed point and limit cycle systems. Both admit explicit Koopman spectral decompositions [40], allowing us to analyze their critical sampling periods.

***Fixed point system***

The fixed point system is given by

$$\begin{aligned} \dot{x}_1 &= -3x_2 - x_1(x_1^2 + x_2^2), \\ \dot{x}_2 &= 3x_1 - x_2(x_1^2 + x_2^2). \end{aligned} \tag{77}$$

This system admits a fixed point at the origin, i.e., $\mathbf{f}(0,0) = 0$.For nonlinear systems with fixed point $\mathbf{x}^*$, the principal Koopman eigenvalues $\lambda_i$ are the eigenvalues of the Jacobian matrix of the vector field $f$ at the fixed point $x^*$ [4]. Therefore, eigenvalues of the generator of the system (77) are eigenvalues of the Jacobian matrix at $(0,0)$:

$$J = \begin{pmatrix} 0 & -3 \\ 3 & 0 \end{pmatrix}. \tag{78}$$

It leads to the principal Koopman eigenvalues $\pm 3i$. According to the formulation of critical sampling theorem, the lower bound of sampling frequency is 6 rad/s and the critical sampling period is $\pi/3$ s.

***Limit cycle system***

The limit cycle system described by

$$\begin{aligned} \dot{x}_1 &= 3x_2 - x_1(x_1^2 + x_2^2 - 1), \\ \dot{x}_2 &= -3x_1 - x_2(x_1^2 + x_2^2 - 1), \end{aligned} \tag{79}$$

admits a stable limit cycle characterized by $x_1^2 + x_2^2 = 1$. For dynamical systems exhibiting a limit cycle, the Floquet exponents correspond to the principal Koopman eigenvalues [4]. The Koopman principal eigenvalues of system (79) are calculated as follows. In polar coordinates, i.e., through the transformation $x_1 = r\cos\theta$ and

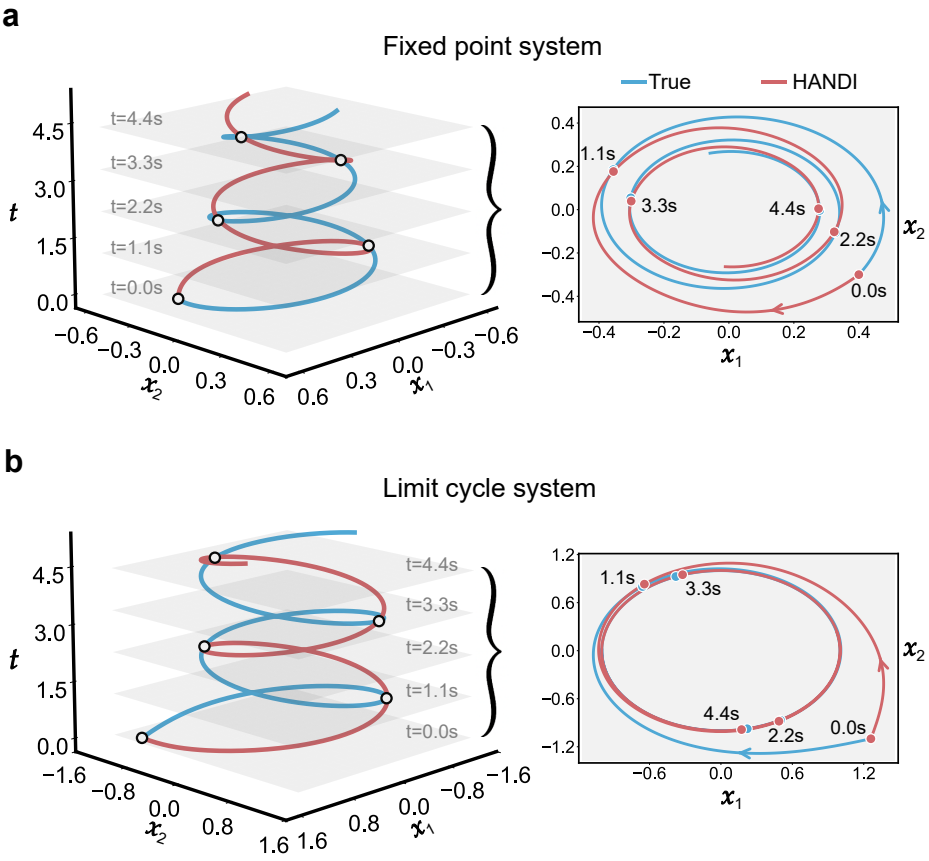


**Fig. 46**: **Aliasing and the theoretical sampling limit revealed by HANDI.** When the sampling period exceeds the theoretical limit $T_\gamma$, distinct dynamical behaviors become indistinguishable in measurements, leading to aliased identification. **a**, Fixed point and **b**, limit cycle systems identified at $T_s = 1.1$ s ($> T_\gamma = \pi/3$ s). While the identified models match the sampled data (blue triangles) almost perfectly, their predicted trajectories evolve in the opposite direction to the true dynamics, confirming that aliasing, i.e., not algorithmic error, causes the mismatch and marking the fundamental limit of continuous-time identification.

$x_2 = r \sin\theta$, we obtain the following dynamical system

$$\begin{aligned} \dot{r} &= -r^3 + r, \\ \dot{\theta} &= -3. \end{aligned} \tag{80}$$

Since the limit cycle is at $r = 1$, the eigenvalue (Floquet exponent) is $-2$. Other principal eigenvalues are $\pm 3i$ with associated eigenfunctions $e^{\mp i\theta}$. According to the formulation of the critical sampling period, the critical sampling period is $\pi/3$ s.

When we increase the sampling period slightly beyond the threshold to $T_s = 1.1\,\mathrm{s}$ (Supplementary Fig. 46), aliasing becomes evident: the identified model matches the sampled measurements almost perfectly, yet the reconstructed trajectories evolve in a qualitatively incorrect direction, producing a dynamically inconsistent picture while incurring negligible error at the sampling points. This decisive mismatch confirms that the failure stems from aliasing rather than the method itself.

# References


[1] Koopman, B.O.: Hamiltonian systems and transformation in Hilbert space. Proceedings of the National Academy of Sciences of the United States of America **17**(5), 315 (1931)

[2] Mezić, I.: Spectral properties of dynamical systems, model reduction and decompositions. Nonlinear Dynamics **41**(1), 309–325 (2005)

[3] Lasota, A., Mackey, M.C.: Chaos, Fractals, and Noise: Stochastic Aspects of Dynamics vol. 97. Springer, New York, NY (2013)

[4] Mauroy, A., Mezić, I.: Global stability analysis using the eigenfunctions of the koopman operator. IEEE Transactions on Automatic Control **61**(11), 3356–3369 (2016)

[5] Petersen, K.B., Pedersen, M.S., *et al.*: The matrix cookbook. Technical University of Denmark **7**(15), 510 (2008)

[6] Moler, C., Van Loan, C.: Nineteen dubious ways to compute the exponential of a matrix, twenty-five years later. SIAM Review **45**(1), 3–49 (2003)

[7] Trefethen, L.N., Bau, D.: Numerical Linear Algebra. SIAM, Philadelphia, PA (2022)

[8] Higham, N.J.: Functions of Matrices: Theory and Computation. SIAM, Philadelphia, PA (2008)

[9] Al-Mohy, A.H., Higham, N.J.: Improved inverse scaling and squaring algorithms for the matrix logarithm. SIAM Journal on Scientific Computing **34**(4), 153–169 (2012)

[10] Higham, N.J., Lin, L.: A schur–padé algorithm for fractional powers of a matrix. SIAM Journal on Matrix Analysis and Applications **32**(3), 1056–1078 (2011)

[11] Williams, M.O., Kevrekidis, I.G., Rowley, C.W.: A data–driven approximation of the Koopman operator: Extending dynamic mode decomposition. Journal of

Nonlinear Science **25**, 1307–1346 (2015)

[12] Kato, T.: Perturbation Theory for Linear Operators vol. 132. Springer, Berlin, Heidelberg (2013)

[13] Challita, E.J., Sehgal, P., Krugner, R., Bhamla, M.S.: Droplet superpropulsion in an energetically constrained insect. Nature Communications **14**(1), 860 (2023)

[14] Graeber, G., Regulagadda, K., Hodel, P., Küttel, C., Landolf, D., Schutzius, T.M., Poulikakos, D.: Leidenfrost droplet trampolining. Nature Communications **12**(1), 1727 (2021)

[15] Kang, D.-H., Cho, S., Kim, H.Y., Shim, S., Kim, D.H., Jeong, B., Lee, Y.S., Park, E.-A., Lee, W., Kim, H., *et al.*: Silicon nanocolumn-based disposable and flexible ultrasound patches. Nature Communications **16**(1), 6609 (2025)

[16] Vikrant, K., Jayanth, G.: Diamagnetically levitated nanopositioners with large-range and multiple degrees of freedom. Nature Communications **13**(1), 3334 (2022)

[17] Lyu, M., Torii, R., Liang, C., Zhang, X., Wang, X., Li, Q., Ventikos, Y., Chen, D.: Predictive computational framework to provide a digital twin for personalized cardiovascular medicine. Communications Medicine **5**(1), 370 (2025)

[18] Li, Z., Roscow, J., Khanbareh, H., Taylor, J., Haswell, G., Bowen, C.: A comprehensive energy flow model for piezoelectric energy harvesters: understanding the relationships between material properties and power output. Materials Today Energy **37**, 101396 (2023)

[19] Chen, L.-k., Jiang, L.-z., Li, R., Li, Q., Zhang, M., Zhang, N., Luo, J.-z., Ling, L., Zhu, S.-y.: A feasible vibration measurement and active control method of reinforced concrete lightweight pier railway bridges for heavy-haul monorail trains. European Journal of Environmental and Civil Engineering **26**(1), 360–378 (2022)

[20] Bazzani, S., Puliatti, S., Ferretti, S., Bianchi, G., Secchi, C., Ferraguti, F.: Ultrasonographic-guided robotic-assisted percutaneous nephrolithotomy. Communications Engineering **4**(1), 120 (2025)

[21] Galanics, C., Sintár, V., Szalai, I.: Autocatalytic flow chemistry. Scientific Reports **13**(1), 9211 (2023)

[22] Howlett, M.G., Fletcher, S.P.: From autocatalysis to survival of the fittest in self-reproducing lipid systems. Nature Reviews Chemistry **7**(10), 673–691 (2023)

[23] Pu, C., Luan, Y., Wang, Y., Xiao, Z.: Thermal kinetics and flash dsc experimental validation of conventional nitrocellulose and ladder-structured nitrocellulose under non-isothermal condition. Combustion and Flame **260**, 113216 (2024)

[24] Strogatz, S.H.: Nonlinear Dynamics and Chaos: with Applications to Physics, Biology, Chemistry, and Engineering. Chapman and Hall/CRC, Boca Raton, FL (2024)

[25] Strogatz, S.H.: Nonlinear Dynamics and Chaos: with Applications to Physics, Biology, Chemistry, and Engineering (studies in Nonlinearity) vol. 1. Westview press, Boulder, CO (2001)

[26] Bideh, A.Z., Georgievska, A., Gryak, J.: MDBench: Benchmarking Data-Driven Methods for Model Discovery (2025). https://arxiv.org/abs/2509.20529

[27] Abrams, D.M., Strogatz, S.H.: Modelling the dynamics of language death. Nature **424**(6951), 900–900 (2003)

[28] Held, L., Hofmann, M., Höhle, M., Schmid, V.: A two-component model for counts of infectious diseases. Biostatistics **7**(3), 422–437 (2006)

[29] Weber, A., Zuschratter, W., Hauser, M.J.: Partial synchronisation of glycolytic oscillations in yeast cell populations. Scientific Reports **10**(1), 19714 (2020)

[30] Madsen, M.F., Danø, S., Sørensen, P.G.: On the mechanisms of glycolytic oscillations in yeast. The FEBS journal **272**(11), 2648–2660 (2005)

[31] Teusink, B., Larsson, C., Diderich, J., Richard, P., Van Dam, K., Gustafsson, L., Westerhoff, H.V.: Synchronized heat flux oscillations in yeast cell populations. Journal of Biological Chemistry **271**(40), 24442–24448 (1996)

[32] Prokop, B., Gelens, L.: From biological data to oscillator models using sindy. iScience **27**(4), 109316 (2024) https://doi.org/10.1016/j.isci.2024.109316

[33] Yang, A., Axås, J., Kádár, F., Stépán, G., Haller, G.: Modeling nonlinear dynamics from videos. Nonlinear Dynamics **113**(10), 10881–10909 (2025)

[34] Brain Science, A.I.: AllenSDK Documentation. https://allensdk.readthedocs.io/en/latest/index.html. Accessed: 26 Oct 2025

[35] Yue, Z., Thunberg, J., Ljung, L., Yuan, Y., Gonçalves, J.: System aliasing in dynamic network reconstruction: issues on low sampling frequencies. IEEE Transactions on Automatic Control **66**(12), 5788–5801 (2020)

[36] Zeng, Z., Yue, Z., Mauroy, A., Gonçalves, J., Yuan, Y.: A sampling theorem for exact identification of continuous-time nonlinear dynamical systems. IEEE Transactions on Automatic Control **69**(12), 8402–8417 (2024)

[37] Zeng, Z., Liu, J., Yuan, Y.: A generalized nyquist-shannon sampling theorem using the koopman operator. IEEE Transactions on Signal Processing **72**, 3595–3610 (2024) https://doi.org/10.1109/TSP.2024.3436610

[38] Schmid, P.J.: Dynamic mode decomposition of numerical and experimental data. Journal of Fluid Mechanics **656**, 5–28 (2010)

[39] Tu, J.H.: Dynamic mode decomposition: Theory and applications. PhD thesis, Princeton University (2013)

[40] Lan, Y., Mezić, I.: Linearization in the large of nonlinear systems and Koopman operator spectrum. Physica D: Nonlinear Phenomena **242**(1), 42–53 (2013) https://doi.org/10.1016/j.physd.2012.08.017